

©2018

Paul Kim

ALL RIGHTS RESERVED

THE RARE EARTH CARBONATES: PROPERTY TRENDS, SYNTHESIS, AND RELEVANCE

by

PAUL KIM

A dissertation submitted to the

School of Graduate Studies

Rutgers, The State University of New Jersey

In partial fulfillment of the requirements

For the degree of

Doctor of Philosophy

Graduate Program in Materials Science and Engineering

Written under the direction of

Richard E. Riman

And approved by

---

---

---

---

New Brunswick, New Jersey

MAY 2018

## ABSTRACT OF THE DISSERTATION

### THE RARE EARTH CARBONATES: PROPERTY TRENDS, SYNTHESIS, AND RELEVANCE

by PAUL KIM

Dissertation Director:

Richard E. Riman

The rare earth carbonates in the broadest definition are an important class of insoluble rare earth solids that account for a large amount of the globe's rare earth mineral resources and are precipitated as precursor materials in the preparation of other rare earth solids in industrial settings. Understanding how to best extract and utilize the rare earths from carbonate sources starts with a fundamental understanding of the properties of the pure rare earth carbonates, namely the normal carbonates ( $\text{RE}_2(\text{CO}_3)_3 \cdot x\text{H}_2\text{O}$ ) and the hydroxycarbonates ( $\text{RE}(\text{OH})\text{CO}_3$ ). This would allow us to improve the efficiency and sustainability of industrial rare earth refinement, find new ways to precipitate the carbonates, and enable important technologies that rely upon a stable supply of rare earths. Thus, a comprehensive review of the normal carbonates and hydroxycarbonates was conducted to find the values for their fundamental properties;

crystallographic parameters, thermochemical values, thermal decomposition behavior, and aqueous solubility. Trends with respect to increasing atomic number were established based upon the available literature; lattice parameters shrink, are less thermodynamically stable, decompose at successively lower temperatures, and increase in solubility.

These property values, namely the thermochemical and aqueous solubility values, may then be utilized in thermodynamic simulations to discover new processes by which rare earth carbonates can be precipitated from aqueous solutions of pure rare earth salts or mixed rare-earth/metal cation salts. We have predicted and verified the precipitation of the normal rare earth carbonates from concentrated aqueous solutions of rare earth chlorides using monoethanolamine (MEA) loaded with carbon dioxide (CO<sub>2</sub>). This precipitation methodology allows for the facile recovery and separation of the reaction products, the normal carbonate(s) and the water soluble MEA salt, the latter of which has applications in other industries.

Finally, a technology/synthesis strategy that offers a low cost, relatively physically robust alternative to optically active components has been explored to demonstrate the necessity of a stable rare earth supply. Optically active, transparent composite materials were created by tuning the refractive index of the polymer matrix (CN551) using ZrO<sub>2</sub> nanoparticles to match that of the optically active, micron sized rare earth LYE phosphor (La<sub>0.92</sub>Yb<sub>0.075</sub>Er<sub>0.005</sub>F<sub>3</sub>) agglomerates. The nature of the polymer-ceramic composite means that the components are fairly mechanically robust, can load fairly large quantities of optically active components by volume, and are easier to synthesize than their single crystal/polycrystalline counterparts.

## ACKNOWLEDGEMENTS

First and foremost, I am very thankful to my advisor Professor Richard E. Riman for the time and patience he afforded me during my time at Rutgers in pursuit of this doctorate. Thank you for giving me the freedom I needed in order to really figure out how to properly “Ph.D.” and find my own direction. I am also very grateful to my committee members, Doctor Lisa Klein, Doctor Dunbar Birnie, and Doctor Zhichao Hu, for all of your input and help during my time.

To the Riman Group Members, both current and prior, that made my time as a graduate student memorable and worthwhile: Daniel Kopp, Terrence Whalen, Ryan Anderson, Berra Beyoglu Siglam, Haohan Wu, Kevin Blinn, Jun Wang, Dechao Yu, Diane Amato, and Janet Pescinski. Thank you all for helping me grow not only as a graduate student, but also as a person and giving me the support and environment in which I could truly become better. I would also like to thank all of the Rutgers MSE staff and fellow graduate students for also making my time at Rutgers memorable.

To my friends, life here at Rutgers would not have been as fun and meaningful without y’all. I do not have words to express what you guys mean to me, but thank you for everything and the love y’all have shown me. I hope that our friendships will continue to grow and we’ll all see each other through more of all our individual life goals.

To my parents and my little brother, I want to say thank you for all the love and support you all have given unconditionally. Without y’all, nothing I am or have become would have been possible. To my father, you are an example I have always strived to emulate. To my mother, thank you for being such an important part to all of our lives. To my little brother, thank you for also being a good friend as we both try to figure out, “How to life and how to adult.”

To my late mom, all I can say is, “Thank you and I love you.”

This work was supported by the National Science Foundation (NSF) and the Critical Materials Institute (CMI), a United States Department of Energy research hub dedicated to anticipating which materials may go critical and increase the speed of materials discovery and deployment.

## TABLE OF CONTENTS

ABSTRACT OF THE DISSERTATION .....	ii
ACKNOWLEDGEMENTS.....	iv
LIST OF TABLES.....	viii
LIST OF FIGURES.....	ix
<b>Chapter 1. INTRODUCTION .....</b>	<b>1</b>
<b>Chapter 2. TRENDS IN STRUCTURE AND THERMODYNAMIC PROPERTIES OF NORMAL RARE EARTH CARBONATES AND RARE EARTH HYDROXYCARBONATES .....</b>	<b>3</b>
2.1. Introduction .....	3
2.2. Synthesis .....	6
2.2.1. Conversion .....	7
2.2.2. Decomposition .....	9
2.2.3. Precipitation.....	11
2.3. Trends in the Properties of the Rare Earth Carbonates.....	13
2.3.1. Crystallography of the Rare Earth Carbonates .....	15
2.3.2. Thermochemical Properties of the Rare Earth Carbonates.....	19
2.3.3. Thermal Behavior of the Rare Earth Carbonates.....	22
2.3.4. Behavior of Rare Earth Carbonates in Aqueous Environments .....	25
2.4. Final Remarks.....	27
2.5. Figures.....	30
2.6. References .....	39
<b>Chapter 3. PRECIPITATION OF RARE EARTH CARBONATES USING MONOETHANOLAMINE .....</b>	<b>48</b>
3.1 Introduction .....	48
3.2 Materials and Methods.....	51
3.2.1. Thermodynamic Process Simulation.....	51
3.2.2. Rare Earth Carbonate Precipitation .....	51
3.2.3. Characterization.....	53
3.3. Results and Discussion .....	54
3.4. Conclusion.....	59
3.5. Figures.....	60
3.6. Tables .....	64
3.7. References .....	67

<b>Chapter 4. REFRACTIVE INDEX TUNING OF HYBRID MATERIALS FOR HIGHLY TRANSMISSIVE LUMINESCENT LANTHANIDE PARTICLE – POLYMER COMPOSITES.....</b>	<b>71</b>
4.1. Introduction .....	71
4.2. Experimental Sections.....	74
4.2.1. Hydrothermal Synthesis of $\text{La}_{0.92}\text{Yb}_{0.075}\text{Er}_{0.005}\text{F}_3$ Nanoparticles .....	74
4.2.2. Composite Synthesis .....	76
4.2.3. Characterization.....	77
4.3. Results and Discussion .....	79
4.4. Conclusions .....	83
4.5. Figures.....	85
4.6. Tables .....	95
4.7. References .....	96
<b>Chapter 5. FINAL REMARKS .....</b>	<b>100</b>
<b>Appendix 1. ANNEALING SODIUM YTTRIUM FLUORIDE NANOPOWDERS TO IMPROVE OPTICAL PROPERTIES AND SURFACE CHEMISTRY.....</b>	<b>102</b>



## LIST OF TABLES

<b>TABLE 3.1.</b>	<b>INFLOW SOLUTION CONDITIONS FOR SELECT PRECIPITATION EXPERIMENTS .....</b>	<b>64</b>
<b>TABLE 3.2.</b>	<b>INFRARED SPECTRA AS REPORTED BY CARO ET AL<sup>45</sup> (FUJITA NOTATION, CM<sup>-1</sup>) FOR THE NORMAL CARBONATES. V<sub>1</sub> – V<sub>6</sub> CORRESPOND WITH THOSE IN FIGURE 3.3. ....</b>	<b>65</b>
<b>TABLE 3.3.</b>	<b>CONCENTRATIONS OF RARE EARTH CHLORIDE SOLUTIONS BEFORE AND AFTER PRECIPITATION WITH MEA AS DETERMINED BY ICP-OES. N/A REFERS TO CONCENTRATIONS BELOW DETECTABLE LIMITS. ....</b>	<b>66</b>
<b>TABLE 4.1.</b>	<b>NANOCOMPOSITE COMPOSITIONS FOR 5 VOL% LYEF – CN551 – ZrO<sub>2</sub> .....</b>	<b>95</b>
<b>TABLE 4.2.</b>	<b>NANOCOMPOSITE COMPOSITIONS FOR 15 VOL% LYEF – CN551 – ZrO<sub>2</sub> .....</b>	<b>95</b>
<b>TABLE 4.3.</b>	<b>NANOCOMPOSITE COMPOSITIONS FOR 30 VOL% LYEF – CN551 – ZrO<sub>2</sub> .....</b>	<b>95</b>

## LIST OF FIGURES

<b>FIGURE 2.1.</b>	<b>APPLICATIONS OF THE RARE EARTH ELEMENTS BROKEN DOWN BY ELEMENT. MOST APPLICATIONS ARE GEARED TOWARDS HIGH-TECHNOLOGY, SUCH AS LASERS, MAGNETS, PHOSPHORS, ENERGY CONVERSION, AND CATALYSIS. ADAPTED FROM GSCHNEIDNER, JR<sup>2</sup>.....</b>	<b>30</b>
<b>FIGURE 2.2.</b>	<b>(A) CRUSTAL ABUNDANCES OF THE RARE EARTH ELEMENTS (REES) RELATIVE TO SILICON (ADAPTED FROM USGS<sup>5</sup>) AND EACH OTHER (ADAPTED FROM GUPTA<sup>15</sup>). (B) REES ARE RELATIVELY ABUNDANT COMPARED TO PALLADIUM GROUP METALS (E.G., PALLADIUM, PLATINUM, AND RHODIUM). .....</b>	<b>31</b>
<b>FIGURE 2.3.</b>	<b>IONIC RADIUS OF THE TRIVALENT RARE EARTH (RE) CATIONS (ADAPTED FROM GUPTA<sup>15</sup>). LANTHANIDE CONTRACTION IS OBSERVED DUE TO THE WEAK SHIELDING OF THE VALENCE ELECTRONS BY THE 4f ELECTRONS. CERTAIN PROPERTIES OF RARE EARTH CARBONATE PHASES CAN BE CORRELATED WITH ATOMIC NUMBER. ....</b>	<b>32</b>
<b>FIGURE 2.4.</b>	<b>ELECTRON CONFIGURATION OF THE REE CATIONS (ADAPTED FROM GUPTA<sup>15</sup>). .....</b>	<b>33</b>
<b>FIGURE 2.5.</b>	<b>LATTICE PARAMETER DATA FOR THE LANTHANITES AND TENGERTITES, THE NORMAL RARE EARTH CARBONATE HYDRATES. VALUES FOR THE LANTHANITES ARE FROM CARO AND COWORKERS<sup>120</sup>. VALUES FOR THE TENGERTITES ARE FROM WAKITA AND COWORKERS<sup>123</sup>. .....</b>	<b>34</b>
<b>FIGURE 2.6.</b>	<b>LATTICE PARAMETERS FOR THE ORTHORHOMBIC AND HEXAGONAL RARE EARTH HYDROXYCARBONATES. VALUES FOR THE ORTHORHOMBIC HYDROXYCARBONATES ARE FROM TAHARA<sup>124</sup>. VALUES FOR THE HEXAGONAL HYDROXYCARBONATES ARE FROM MICHIBA<sup>79</sup>. .....</b>	<b>35</b>
<b>FIGURE 2.7.</b>	<b>GIBBS FREE ENERGIES OF FORMATIONS AND ENTHALPIES OF FORMATION FROM KARAPET'YANTS<sup>129, 132</sup>. HYDRATION OF THE RARE EARTH CARBONATES MASKS DECREASING THERMOCHEMICAL VALUES WITH RESPECT TO ATOMIC NUMBER AS OBSERVED IN THE ANHYDROUS PHASES. ....</b>	<b>36</b>
<b>FIGURE 2.8.</b>	<b>ENTHALPIES OF FORMATION FOR HEXAGONAL AND ORTHORHOMBIC HYDROXYCARBONATES FROM RORIF<sup>127</sup> AND SHIVARAMAIAH<sup>99</sup>. VALUE FOR ORTHORHOMBIC YTTRIUM HYDROXYCARBONATE IS FROM SHIVARAMAIAH<sup>99</sup> .....</b>	<b>37</b>

FIGURE 2.9.	SOLUBILITY PRODUCTS AND RAW DATA FOR THE NORMAL CARBONATES ARE PRESENTED FROM CARO AND COWORKERS <sup>48</sup> , JORDANOV <sup>141</sup> , AND SPAHIU <sup>142</sup> . IN GENERAL, THE SOLUBILITY OF THE NORMAL CARBONATES INCREASES WITH INCREASING ATOMIC NUMBER. THE DOTTED LINES ARE THE VALUES FOR SCANDIUM CARBONATE AND YTTRIUM CARBONATE AS REPORTED BY THE RESPECTIVE AUTHORS AND ARE PRESENTED FOR REFERENCE. SOLUBILITY PRODUCTS FOR THE HEXAGONAL AND ORTHORHOMBIC HYDROXYCARBONATES ARE FROM RORIF <sup>127</sup> . NO TREND WITH RESPECT TO ATOMIC NUMBER MAY BE ESTABLISHED, BUT THE ORTHORHOMBIC CARBONATES ARE IN GENERAL MORE SOLUBLE THAN THEIR HEXAGONAL COUNTERPARTS...	38
FIGURE 3.1.	THERMODYNAMIC SIMULATION FROM OLI SOFTWARE. EQUILIBRIUM PHASE DIAGRAM AS A FUNCTION OF MEA CONCENTRATION (MOLALITY) WITH RESPECT TO NdCl <sub>3</sub> CONCENTRATION (MOLALITY) AT A FIXED pCO <sub>2</sub> = 1 ATM AND T = 25 °C. PHASE STABILITY DIAGRAMS FOR Nd(OH)CO <sub>3</sub> AND Nd <sub>2</sub> (CO <sub>3</sub> ) <sub>3</sub> ARE PRESENTED. GREEN AREAS REPRESENT CONDITIONS AT WHICH THE SOLIDS MAY BE RECOVERED AT 99% YIELD. ....	60
FIGURE 3.2.	X-RAY DIFFRACTION SPECTRA FOR SELECTED UNAGED AND AGED RARE EARTH CARBONATE SAMPLES.....	61
FIGURE 3.3.	FTIR SPECTRA OF UNAGED, AGED, AND COMMERCIAL VARIANTS OF THE RESPECTIVE RARE EARTH CARBONATES. REFERENCE POSITIONS FOR KNOWN VIBRATION PEAKS FOR THE RESPECTIVE RARE EARTH CARBONATES ARE LABELED AS V <sub>1</sub> - V <sub>6</sub> WITH CORRESPONDING DOTTED LINES. EXACT POSITIONS OF REFERENCE VIBRATION PEAKS CAN BE FOUND IN TABLE 3.2.....	62
FIGURE 3.4.	THERMAL DECOMPOSITION PROFILES FOR THE UNAGED AND AGED RARE EARTH CARBONATES. ....	63
FIGURE 4.1.	ILLUSTRATION OF ACHIEVING HIGH TRANSMITTANCE THROUGH RI MATCHING. A) INCIDENT LIGHT IS TRANSMITTED THROUGH THE OPTICALLY HOMOGENEOUS MEDIUM WITH NO SCATTERING (N <sub>MATRIX</sub> = N <sub>PARTICLE</sub> ). B) INCIDENT LIGHT IS SCATTERED BY THE PARTICLE AS THE MEDIUM IS NOT OPTICALLY HOMOGENEOUS (N <sub>MATRIX</sub> ≠ N <sub>PARTICLE</sub> ). ....	85
FIGURE 4.2.	SCHEMATIC FOR THE ASTM 1003-92 STANDARD FOR THE MEASUREMENT OF POLYMER MATERIAL HAZE. COMPOSITE SAMPLES ARE PLACED IN THE LOCATIONS DICTATED BY T2 AND T4. ....	86

FIGURE 4.3.	X-RAY DIFFRACTION SPECTRUM OF $\text{La}_{0.92}\text{Yb}_{0.075}\text{Er}_{0.005}\text{F}_3$ POWDERS EXHIBITING CHARACTERISTIC PEAKS FOR FLUOCERITE (PDF# 97-001-6964). ....	87
FIGURE 4.4.	SCANNING ELECTRON MICROGRAPHS OF A) $\text{La}_{0.92}\text{Yb}_{0.075}\text{Er}_{0.005}\text{F}_3$ PARTICLES (LYEF), AND CROSS SECTIONS OF [LYEF]-[CN551] COMPOSITES AT B) 5 VOL% LYEF, C) 15 VOL% LYEF, AND D) 30 VOL% LYEF. ....	88
FIGURE 4.5.	CHANGES IN REFRACTIVE INDEX OF THE CN551 POLYMER MATRIX WITH RESPECT TO $\text{ZrO}_2$ SOLIDS LOADING. A) REFRACTIVE INDEX OF THE INDIVIDUAL COMPONENTS. B) REFRACTIVE INDEX OF CN551 POLYMERS AT DIFFERENT $\text{ZrO}_2$ SOLIDS LOADINGS (VOL%). C) EXTRACTED REFRACTIVE INDEX VALUES AT $\lambda = 980$ NM USING MAXWELL-GARNETT AND LORENTZ-LORENZ APPROXIMATIONS.....	89
FIGURE 4.6.	A) TRANSMITTANCE OF 5 VOL% [LYEF]-[CN551- $\text{ZrO}_2$ ] COMPOSITES WITH RESPECT TO $\text{ZrO}_2$ SOLIDS LOADING. B) EXTRACTED TRANSMITTANCE VALUES AND HAZE VALUES AT $\lambda = 980$ NM. LOSSES DUE TO SCATTERING ARE MINIMIZED WHEN THE REFRACTIVE INDEX OF THE MATRIX MATCHES THAT OF [LYEF]. ....	90
FIGURE 4.7.	TRANSMITTANCE OF A) 15 VOL% LYEF AND B) 30 VOL% LYEF NANOCOMPOSITES. MAXIMUM TRANSMITTANCE OF THE NANOCOMPOSITES CORRESPONDS TO THE THEORETICALLY DETERMINED REFRACTIVE INDEX MATCH POINT (27.4 VOL% AND 37.9 VOL% $\text{ZrO}_2$ , RESPECTIVELY). ....	91
FIGURE 4.8.	RELATIVE INTENSITY VALUES OF 15 VOL% LYEF COMPOSITES AT $\lambda = 1530$ NM AS DETERMINED BY PHOTOSPECTROMETRY. CURVES INDICATE CHANGES IN RELATIVE INTENSITIES OVER TIME OF 1530 NM EMISSION. A) MEASURED 2 MONTHS AFTER INITIAL SYNTHESIS. B) MEASURED 18 MONTHS AFTER SYNTHESIS.	92
FIGURE 4.9.	MICROSTRUCTURE SCHEMATIC FOR INITIAL CONDITIONS THAT RESULT IN PROPOSED CHANGES IN MICROSTRUCTURE THAT ACCOUNTS FOR CHANGE IN RELATIVE OPTICAL EMISSION INTENSITY WITH RESPECT TO $\text{ZrO}_2$ ( $r = 4$ NM) AND $\text{LaF}_3$ ( $r = 40$ NM) SOLIDS LOADING OVER TIME. INITIAL SOLIDS LOADING CONDITIONS DETERMINE INITIAL INTERPARTICLE SPACING (IPS) CONDITIONS.....	93
FIGURE 4.10.	$\text{ZrO}_2$ NANOPARTICLE IPS WITH RESPECT TO $\text{LaF}_3$ SOLIDS LOADING. IPS < 20 NM ARE DISTANCES AT WHICH ATTRACTIVE FORCES OVERCOME REPULSIVE FORCES. A) FIXED $\text{ZrO}_2$ PARTICLE SIZE ( $r = 4$ NM) WITH VARIABLE	

**ZrO<sub>2</sub> VOLUME FRACTION. B) FIXED ZrO<sub>2</sub> VOLUME FRACTION (17 VOL%) WITH VARIABLE ZrO<sub>2</sub> PARTICLE SIZE.**

**C) LaF<sub>3</sub> AND ZrO<sub>2</sub> IPS WITH FIXED ZrO<sub>2</sub> VOLUME FRACTION (5 VOL%) AND PARTICLE SIZE (R = 10 NM). .. 94**

## **Chapter 1. INTRODUCTION**

The rare earth elements are a ubiquitous part of modern life. From the gasoline in our cars, the lights in your ceiling, to the cellphones that have become an indispensable fixture to our lives, the rare earth elements and their consumption by a country are the stick by which some measure the degree of technological and economic prosperity of a country. Fortunately, the rare earth elements are not rare. Global reserves, more of which are being discovered, more than meet global demands for at least the next 500 years and beyond. However, the caveat to this is, "Can these rare earth resources be economically and sustainability tapped?" To vastly oversimplify a complex answer, many rare earth resources are physically accessible, but the chemistries and processes required to refine the rare earths can limit how much can be sustainably extracted. Understanding and creating a process by which rare earths may be extracted starts with the rare earth's fundamental properties and those of the deposits in which they are found.

A significant quantity of rare earth enriched minerals are carbonate minerals such as bastnaesite and lanthanite. The rare earth carbonates are also an important precipitation product that is generated during the rare earth refinement process. Thus synthesizing, analyzing, and perhaps measuring the fundamental properties of the rare earth carbonates will improve our ability to take advantage of these carbonate based resources. Understanding the rare earth carbonates begins with the pure rare earth carbonates, the normal carbonates ( $\text{RE}_2(\text{CO}_3)_3 \cdot x\text{H}_2\text{O}$ ) and the hydroxycarbonates ( $\text{RE}(\text{OH})\text{CO}_3 \cdot x\text{H}_2\text{O}$ ). These carbonates are important as the rare earths in geological settings where water ( $\text{H}_2\text{O}$ ) and carbon dioxide ( $\text{CO}_2$ ) are abundant are generally found as the carbonate. Herein, we present an overview of the normal carbonates and hydroxycarbonates, a new method to precipitate the rare earth carbonates, and an application of rare earth materials in a technology that requires a sustainable supply of rare earths.

Chapter 2, Trends in the Properties of the Rare Earth Carbonates, synthesizes our current understanding of the rare earth normal carbonates and the rare earth hydroxycarbonates by means of a literature review and survey. It discusses the trends in the various properties of the rare earth carbonates (e.g., thermochemical and crystallographic) to demonstrate what we understand, what we poorly understand, and what does not exist in literature. We also explore the history of the various synthesis methods that have been used to create the rare earth carbonates, including the most popular contemporary methods, along with their shortcomings.

Chapter 3, The Precipitation of Rare Earth Carbonates using Monoethanolamine, builds upon our discussion of rare earth carbonate synthesis and presents the first instance of rare earth carbonate precipitation using monoethanolamine (MEA, 2-aminoethanol, ethanolamine) loaded with CO<sub>2</sub>.

Chapter 4, contextualizes the importance of the rare earth carbonates as a precursor material in the rare earth supply chain by introducing, "Refractive Index Tuning of Hybrid Materials for Highly Transmissive Luminescent Lanthanide Particle – Polymer Composites." This work presents a method by which optically active, transparent composite materials are created using refractive index tuning. This technology can be used to create lower cost, mechanically robust alternatives to optically active, high technology materials, such as optical amplifiers. Development, deployment, and improvements in high technologies such as optical amplifiers, displays, or lasers would not be possible without a sustainable rare earth supply chain, which cannot be achieved without a fundamental basis of understanding and sustainable production.

## **Chapter 2. TRENDS IN STRUCTURE AND THERMODYNAMIC PROPERTIES OF NORMAL RARE EARTH CARBONATES AND RARE EARTH HYDROXYCARBONATES**

### **2.1. Introduction**

The rare earth elements have made their way into many aspects of modern life. From the gasoline in automobiles, the ubiquitous mobile phones, speakers, lights, to energy production, the rare earth elements are indispensable to current standards of living and technology. Common applications of the rare earth elements are summarized in Figure 2.1. The interesting properties that have allowed their application are largely due to the unique 4f electrons that have highly localized electronic states and very predictable electronic transitions that are weakly influenced by the coordination environment or crystal field. In general, this means that the unique physical properties of the rare earth ions are largely unaffected by their surroundings. However, it should be noted that slight variations and nuanced interactions of the rare earth ions with their surroundings are of great research interest<sup>1</sup>.

The International Union of Pure and Applied Chemistry (IUPAC) defines the rare earth elements as the series of 17 chemically similar elements in the periodic table<sup>3</sup> including scandium, yttrium, and the lanthanides. Scandium and yttrium are chemically similar to the lanthanides and often collocated with the lanthanides in mineral deposits. Scandium is not as widely utilized as the other rare earths as the process for obtaining metallic scandium is quite difficult. It is only relatively recently that scandium has found limited application in aluminum alloys. All but one of the lanthanides (lanthanum to lutetium) fill the 4f electron shell. Depending upon classification and researchers' preferences, either lanthanum, despite the namesake, or lutetium can be excluded from the lanthanide classification. Promethium was the last of rare earth elements to be formally



discovered and is mainly utilized for its radioactivity in research and a small amount of applications<sup>4</sup>.

The rare earth elements are not actually rare in geologic abundance, despite their name<sup>5</sup> (Figure 2.2). In absolute terms, the rare earth elements are more abundant than many of the platinum group metals (e.g., platinum and palladium) and have similar abundances to tin, zinc, and tungsten. Lutetium and thulium are the least abundant and lanthanum, cerium, and yttrium are the most abundant. The rare earth element of even atomic number is more abundant than either of the corresponding rare earth elements of odd atomic number on either side (Figure 2.2) in the periodic table (e.g., cerium (58) is more abundant than both lanthanum (57) and praseodymium (59)). The rare earth elements are co-located with one another and usually found as part of a host mineral. Many of these rare earth enriched minerals are carbonate minerals<sup>6</sup>, such as bastnaesite and lanthanite, and are found in large carbonatite deposits, such as those at Mountain Pass (California, USA)<sup>7</sup> and Bayan Obo (Inner Mongolia, China)<sup>8,9</sup>. Economically viable rare earth mineral deposits, large quantities of minerals with high rare earth concentrations and chemistries that allow for the relatively easy separation of the rare earth elements from the host, are mined and refined in only a few locations around the world. Large capital costs, high environmental impact, and specific mineral chemistries have resulted in China producing the majority of the world's rare earths<sup>5,10–14</sup>.

The ability to refine and produce rare earth products from the aforementioned carbonate mineral deposits begins with a fundamental understanding of the rare earth carbonates. The rare earth carbonates include both the rare earth bearing carbonate minerals and the synthetic rare earth carbonates that match the chemical composition of either the naturally occurring minerals or the pure single element carbonates. Understanding the behavior of the rare earth carbonates in geochemical systems begins with the behavior of the rare earths in the  $\text{RE}_2\text{O}_3 - \text{CO}_2 - \text{H}_2\text{O}$  ternary

system. At standard temperature and pressure (25 °C, 1 atm), the rare earth carbonates are the hydrated normal rare earth carbonates ( $\text{RE}_2(\text{CO}_3)_3 \cdot x\text{H}_2\text{O}$ ) and the rare earth hydroxycarbonates ( $\text{RE}(\text{OH})\text{CO}_3 \cdot x\text{H}_2\text{O}$ , also known as basic carbonates, carbonate hydroxide, hydroxylcarbonates, and hydroxocarbonates). Anhydrous variants of the normal carbonates and hydroxycarbonates exist, but they readily absorb water to create their respective hydrated variants. The rare earth oxycarbonates are also an important class of rare earth carbonates. However, these oxycarbonates form at higher temperatures as a result of the thermal decomposition of either the normal carbonates or hydroxycarbonates. Within the framework of this study, the oxycarbonates and the anhydrous carbonates are treated as the thermal decomposition products of their respective rare earth carbonate and will not be thoroughly addressed.

The preponderance of  $\text{CO}_2$  and  $\text{H}_2\text{O}$  in geological systems at ambient conditions has necessitated the analysis of the rare earth carbonates, especially with respect to phase stability, crystallography, thermodynamic stability, and behavior in water. Understanding which rare earth carbonate phase (normal vs hexagonal hydroxycarbonate vs orthorhombic hydroxycarbonate) will form in certain  $\text{CO}_2$ ,  $\text{H}_2\text{O}$ , pressure, and temperature conditions is crucial to understanding the geochemistry and distribution of rare earths in natural systems. This is particularly important to nuclear fuel applications, as certain lanthanides are the fission products of nuclear fuels and other lanthanides, such as neodymium, serve as chemical homologues in studying the distribution of radioactive actinides in natural  $\text{CO}_2$ - $\text{H}_2\text{O}$  hydrothermal systems<sup>16–19</sup>. In industrial rare earth production, understanding what phase the rare earth carbonates will assume in these mineral deposits (normal vs hexagonal hydroxycarbonate vs orthorhombic hydroxycarbonate) informs how the deposit can be processed. The refined rare earths are then precipitated as the rare earth carbonates to be used in the downstream production of other rare earth solids such as the rare earth chlorides, sulfates, and oxides. These industrially produced rare earth carbonate products

utilize alkali or ammonium carbonates/bicarbonates to simultaneously adjust pH and precipitate<sup>20–33</sup> from process streams.

The purpose of this study is to present the most common synthesis methods of the rare earth carbonates, their crystallographic structure, thermochemical data, aqueous behavior, and thermal stability. Through this treatment, we will find trends that can be attributed to the unique chemistry of the rare earth elements and identify inconsistencies and research needs in the current body of literature.

## **2.2. Synthesis**

The history of the rare earth carbonates begins in the latter half of the 19<sup>th</sup> century. Treatises on chemistry in the first half of the 19<sup>th</sup> century, such as those by Sylvester<sup>34</sup> and Reid<sup>35</sup>, contain scant mention, if any, of the rare earth elements. Considering that Johan Gadolin's discovery of yttrium dates to 1792, spread in knowledge concerning the chemistry of these new rare earths would have been limited. However, treatises on chemistry from the late 19<sup>th</sup> century onwards address the rare earth carbonates, along with other rare earth salts. Treatises such as those by Roscoe and Schorlermmmer<sup>36</sup>, Treadwell<sup>37</sup>, Blitz and Blitz<sup>38</sup>, and Fresenius<sup>39</sup> briefly detail the synthesis of the rare earth carbonates, though no specific mention of the stoichiometry is made. The most popular methods were precipitation from an aqueous rare earth salt solution using alkali/ammonia carbonates/bicarbonates or the conversion of the rare earth hydroxide to the carbonate using gaseous carbon dioxide. Efforts to synthesize the rare earth carbonates by alternative means yielded results in the 20<sup>th</sup> century. Starting in the 1950's, rare earth carbonates were synthesized by homogeneous precipitation from an aqueous solution of the rare earth salt plus a water soluble organic compound. Also known as decomposition synthesis, this method has been extensively used in laboratory settings to synthesize the carbonates. In laboratory settings

with high purity requirements, homogeneous precipitation has been the synthesis method of choice as the conversion of hydroxide is a relatively slow process and precipitation using the alkali/ammonia carbonates/bicarbonate salts result in alkali or double carbonate contamination<sup>36–42</sup>.

We have classified the various synthesis methods of the rare earth carbonates as conversion, precipitation, and decomposition. Based upon the findings by Kutty<sup>43–47</sup> and Caro<sup>48–50</sup>, each of these synthesis types can be used to create the desired rare earth carbonate phase (normal vs hydroxy). It should be noted that the most convenient means of creating the hydroxycarbonates are the decomposition methods. Both types of carbonates can be used in laboratory settings as host materials or as template materials in the formation of other nanocrystalline rare earth phases<sup>51–75</sup>. In industrial settings, both normal and hydroxycarbonates have been equally useful as precursor materials.

### *2.2.1. Conversion*

Conversion synthesis methods create rare earth carbonates by directly converting a colloidal solution of the insoluble precursor material into the rare earth carbonate of interest. Direct mention of this synthesis method can be found in chemistry treatises<sup>36–39</sup> dating to the late 19<sup>th</sup> century. In these cases, rare earth carbonates are created by flowing gaseous CO<sub>2</sub> through a wet solution of the rare earth hydroxide. Later reports in the early 20<sup>th</sup> century will use this technique to begin the work of definitively characterizing the rare earth carbonates. Raikow et al.<sup>76</sup> demonstrated the formation of lanthanum, yttrium, and cerium carbonates in addition to the formation of other metal carbonates, by flowing relatively low pressure, gaseous CO<sub>2</sub> over aqueous solutions of their respective metal hydroxides. By this method, normal lanthanum carbonate, yttrium hydroxycarbonate, and cerous/ceric carbonates were synthesized. Converting

a RE hydroxide into its respective RE carbonate by this method is quite simple but is slow and has low conversion yields<sup>77</sup>.

More recent advances in synthesizing rare earth carbonates from insoluble precursor materials (considering that solubility products of rare earth hydroxides range from  $10^{-18}$  to  $10^{-21}$ ) have come to include the conversion of the rare earth oxide<sup>49,50,78</sup>. Caro and coworkers<sup>50</sup> synthesized the entire array of normal rare earth carbonates at room temperature by equilibrating a colloidal solution of the oxides with a CO<sub>2</sub> overpressure of 1 atm over a matter of days to weeks. Caro and coworkers later demonstrated<sup>49</sup> that the lighter normal rare earth carbonates can be hydrolyzed to create the hydroxycarbonates by allowing the lighter normal rare earth carbonates to sit in water without CO<sub>2</sub> overpressure. Work by Fernando and coworkers<sup>78</sup> utilized supercritical CO<sub>2</sub> at 2800 psi and at temperatures less than 100 °C to synthesize the normal carbonates of lanthanum, neodymium, samarium, europium, gadolinium, dysprosium, and holmium. It was demonstrated that working with very low solids loading of the oxides, at lower temperatures, increasing pCO<sub>2</sub> increased conversion yields while keeping conversion times relatively short (> 95 % conversion in 1 hour) with increasing reaction times not giving measurable increases in yield.

RE<sub>2</sub>O<sub>3</sub> – CO<sub>2</sub> – H<sub>2</sub>O systems have been studied using varied system pressure and temperature to determine hydrothermal phase equilibria of the system<sup>43–47</sup>. With sufficient pCO<sub>2</sub> and mole fraction of CO<sub>2</sub>, the hydrated normal carbonates are preferred over the hydroxycarbonates at lower temperatures. Exact temperatures and mole fraction of CO<sub>2</sub> at which each carbonate (e.g., normal carbonate vs. hydroxycarbonate vs. monoxycarbonate) becomes preferred changes with system pressure. In general, the normal carbonates form preferentially at temperatures less than 200 °C given sufficient pCO<sub>2</sub>/mole fraction of CO<sub>2</sub>. With insufficient amounts of CO<sub>2</sub>, the hydroxycarbonates are generally preferred regardless of temperature. As previously mentioned,

the normal carbonates of the lighter rare earths can form their hydroxycarbonates at ambient conditions when exposed to water.

Gaseous  $\text{CO}_2$  is an integral part in the synthesis of the rare earth carbonates. Upon initial inspection, the conversion methods are relatively straightforward, facile means of creating the desired carbonates, especially the normal carbonates. Simple as they are, they are not necessarily the most popular or cost-effective solutions for creating the rare earth carbonates. Converting the hydroxides to the carbonates is a slow process. Converting the oxides to the carbonates using supercritical  $\text{CO}_2$  is a quick process with high yields, but requires high pressure vessels to contain the supercritical  $\text{CO}_2$ <sup>78</sup>. In both cases, high throughput synthesis of the carbonates is not possible. Synthesis of the carbonates from an aqueous solution of a rare earth salt is also not possible by these means. Yet, the importance of  $\text{CO}_2$  to the synthesis process, regardless of the type of synthesis, cannot be understated.

#### *2.2.2. Decomposition*

Decomposition synthesis, also known as homogeneous precipitation, create the rare earth carbonates by increasing the effective concentration of aqueous  $\text{CO}_2$ /carbonate ions in solutions via the decomposition of rare earth organic salts or soluble organic compounds at elevated temperatures. Unlike the conversion of insoluble template materials in a colloidal solution, these precipitations occur from completely aqueous solutions of the rare earth salts plus an organic compound. An initial reason for finding decomposition-based methods for synthesizing the rare earth carbonates was to eliminate the contamination from carbonate/bicarbonate salt precipitations and the slow conversion process of the rare earth oxides/hydroxides. Hence, in principle, any organic compound that liberates  $\text{CO}_2$  upon decomposition/hydrolysis in water can serve as a  $\text{CO}_2$  source. Despite that, the most popular organic compounds/salts that have been

used are trichloroacetic acid and urea. Other organic sources such as gelatin, formic acid<sup>79,80</sup>, acetic acid<sup>81</sup>, and propionic acid<sup>81</sup> have been used but have not been as popular.

Rare earth trichloroacetate salts were one of the first rare earth organic salts used to synthesize the rare earth carbonates. Salutsky and Quill<sup>82</sup> first synthesized the normal carbonates of lanthanum, neodymium, and samarium using this method in 1950. The oxide is first dissolved in an excess of the trichloroacetic acid and then heated under CO<sub>2</sub> bubbling until the excess trichloroacetic acid has been decomposed, after which precipitation can occur. Follow up studies on the normal rare earth carbonates by others such as Charles<sup>83</sup>, Head<sup>84,85</sup>, Sastry<sup>86</sup>, Wakita<sup>87</sup>, Shinn<sup>88</sup>, and Eyring and coworkers<sup>89,90</sup> have utilized rare earth trichloroacetate decomposition to synthesize phase pure normal rare earth carbonates. For the purposes of characterizing the normal carbonates, such as diffraction analysis and thermal decomposition analysis, trichloroacetate decomposition has been the choice synthesis method. From these normal carbonates, the respective hexagonal hydroxycarbonates may be synthesized via hydrolysis; elevated temperatures and low pCO<sub>2</sub> overpressure accelerate this hydrolysis. This hydrolysis occurs quickly and many steps during the normal carbonate synthesis are usually taken to ensure this does not occur, such as pCO<sub>2</sub> overpressure during reaction and washing with CO<sub>2</sub>-laden water. To synthesize the orthorhombic hydroxycarbonates, alternative organic compounds other than trichloroacetic acid are used.

Urea decomposition was reported by Akinc and coworkers<sup>91,92</sup> and Matijevic and coworkers<sup>61,71,72</sup> in the late 1980's and early 1990's. Since then, it has become one of the most favored CO<sub>2</sub>-source organic compounds in the laboratory synthesis of rare earth carbonates<sup>59,68,74,75,93–98</sup>, particularly the orthorhombic hydroxycarbonates. Urea hydrolysis is rather slow at even 90 °C, but is accelerated by the presence of lanthanide salts. Increasing the temperature beyond 100 °C results in uncontrolled, accelerated decomposition of urea. For nanoparticle synthesis, this has been

shown to be an undesirable outcome as this affects particle size distribution, but this may not necessarily be a concern for purely synthesizing the hydroxycarbonate<sup>99</sup>.

Other organic compounds such as gelatin, formic acid<sup>79,80</sup>, acetic acid<sup>81</sup>, and propionic acid<sup>81</sup> have been used to create the rare earth carbonates, but have only been utilized on a very limited scale, if at all. The most popular trichloroacetate and/or urea decompositions have been successfully used to synthesize the entire gamut of rare earth carbonates<sup>59,61,68,71,72,74,75,82–90,94–98</sup>. In laboratory settings where chemical purity is of utmost importance, they have been considered as choice precursor materials as the alkali precipitants will create double carbonate contaminants given sufficient contact time. Other modifications to reaction conditions such as stabilizing ligands, temperature, pressure, carbonate source content, and solvent have been used with great aplomb to achieve variations in particle morphology.

Decomposition syntheses are much faster than conversion syntheses and can be comparable in time to precipitations using carbonate/bicarbonate salts. Some laboratory-based carbonate syntheses utilize these salts. Yet, compared to salt precipitations, decomposition syntheses are not as straightforward and difficult to scale to large quantities. This particular quality of the carbonate/bicarbonate salt precipitations has made these salts the choice methods for industrial scale precipitations from highly acidic rare earth salt solutions.

### *2.2.3. Precipitation*

One of the most cost-effective ways of producing rare earth carbonates en masse from rare earth salt solutions (e.g., rare earth chlorides and nitrates) is by the precipitation of a rare earth carbonate using carbonate or bicarbonate salts. In an industrial setting, alkali or ammonia carbonate/bicarbonate salts are the most employed precipitation agents within the rare earth stripping/extraction/calination process(es)<sup>20–33</sup>. Given that many of these industrial rare earth



salt solutions are highly acidic, the “dual” nature of these precipitation agents are very useful; they adjust pH to the carbonate/hydroxide precipitation pH regime ( $\text{pH} \geq 6.0$ ) and increase the aqueous carbonate/bicarbonate concentrations beyond saturation. Synthetic rare earth salt solutions, i.e., those derived directly from the rare earth salts, are also acidic and benefit from the ‘dual’ nature of the carbonate/bicarbonate salts. Achieving  $\text{pH} \geq 6.0$  is a necessary component to the precipitation process as the rare earth carbonates are soluble at even moderately acidic pH. In laboratory settings, the rare earth carbonates are also synthesized using these salts. Nagashima<sup>97</sup> reported that the use of bicarbonate salts improved the crystallinity of the final rare earth carbonate products. However, since research laboratories require high purity products and have other product requirements such as particle size, shape, and crystallinity, these parameters are more easily controlled using decomposition synthesis, and carbonate/bicarbonate salt precipitations are not as favored. Based upon our understanding of the  $\text{RE}_2\text{O}_3\text{-CO}_2\text{-H}_2\text{O}$  hydrothermal equilibria, the normal carbonates are the preferred carbonate phases in these precipitation processes. Most carbonate salt precipitation processes are conducted at ambient conditions in relatively short amounts of time. However, if the rare earth carbonate is allowed to remain in contact with aqueous alkali carbonate/bicarbonate salt solution, the carbonate will either hydrolyze to create hydroxycarbonate<sup>100</sup> or, more likely, create a double carbonate<sup>36–42,101–104</sup>.

The double carbonates, single crystal phases characterized as a mixture of an alkali carbonate and rare earth carbonate, are a phase unique to the carbonate/bicarbonate salt precipitation methodologies. It has been understood since the beginnings of rare earth carbonate synthesis that the double carbonates form if a rare earth carbonate is allowed to sit in a solution of the alkali carbonate/bicarbonate salt<sup>36–39</sup>. Ammonium carbonate/bicarbonate solutions do not result in a double carbonate, but rather result in the formation of the peroxycarbonate<sup>105</sup>. It should be

noted that the dissolution process occurs more rapidly if the excess salt solution is that of the bicarbonate salt. Yet, regardless of either carbonate or bicarbonate, the final carbonate product will be the double carbonate. This process occurs in two steps. The rare earth carbonates will dissolve in the salt solution and then precipitate as the double carbonate. It should be noted that this process is not quick and requires the rare earth carbonate to be in contact with carbonate salt solution for hours to days for appreciable amounts of precipitation. The best characterized rare earth/alkali double carbonates are those of the rare earth/sodium double carbonates<sup>40,102–104</sup>. Rare earth/potassium double carbonates also occur<sup>41,42,102</sup>.

End product purity requirements, amongst other requirements, ultimately dictate what synthesis method is used to create the rare earth carbonate. Conversion methods are no longer as popular as the very large amounts of time require to achieve full conversions to the carbonates have seen them fall out of favor. The decomposition methods can be used to tailor product-specific properties such as particle size, morphology, and crystalline phase in laboratory settings. Decomposition methods are faster than conversion methods but still much slower than carbonate salt precipitations. Carbonate salt precipitations are generally not used to tailor product-specific properties such as particle size and shape, but are much more straightforward than decomposition methods, yet susceptible to double carbonate contamination.

### **2.3. Trends in the Properties of the Rare Earth Carbonates**

The rare earth elements, because of their chemically similar natures, exhibit a number of trends with respect to their atomic numbers. Many of these trends can be correlated with the lanthanide contraction, the decrease in ionic radii with increasing atomic number<sup>15</sup>. From lanthanum to lutetium, there is a demonstrable decrease in the ionic radius of the trivalent lanthanide cations due to the weak shielding of the valence electrons by the inner 4f electrons (Figure 2.3). This

contraction manifests itself in the slight chemical differences between the rare earths, including yttrium and scandium, that allow for their chemical separation during industrial refining process. Based upon ionic radius, the properties of scandium are very different from those of all other rare earths and the properties of yttrium are somewhere between those of erbium and thulium. Though it may be difficult to separate immediately adjacent lanthanides (due to a small difference in ionic radius and chemistry), increasingly greater differences in ionic radius, and thus chemistry, allows for easier separation. It is relatively straightforward to separate lanthanum from erbium but extraordinarily difficult to separate neodymium from praseodymium.

A number of lanthanide properties follows a general trend that is similar in principle to the lanthanide contraction. The metallic lanthanides have increasing Vickers hardness, density, and melting points with increasing atomic number. Europium and ytterbium are notable exceptions as they are divalent in the metallic state instead of the more common trivalent state (Figure 2.4). Cerium is also an exception as cerium can also be tetravalent, but the effect on Vickers hardness, density, and melting point is not as pronounced.

The rare earth carbonates exhibit a number of trends that are similar in principle to that of the lanthanide contraction. Their crystallography, thermal stability, thermochemistry, and behavior in aqueous systems demonstrate some trends with increasing atomic number. Identifying these trends furthers our understanding of the influence of rare earth chemistry on materials and enables predictive capabilities in the general  $\text{RE}_2\text{O}_3 - \text{CO}_2 - \text{H}_2\text{O}$  system(s). The slight and major differences that arise in the rare earth carbonates, such as the unit cell parameters in the rare earth carbonates within the same isostructural group, the hydrolysis tendency of the normal rare earth carbonate to create the hydroxycarbonate, or solubility differences in aqueous solutions, enables our ability to separate the rare earths. In natural water systems that contain an abundance of water, carbon dioxide, and the rare earth oxides, a systematic understanding of

rare earth carbonates can help us predict the distribution of the rare earths in these systems. As mentioned previously, rare earths are important in the study of nuclear fuel applications as rare earths are fission products of nuclear fuels and certain lanthanides are good chemical homologues for some actinides. As the carbonates are believed to be the solubility limiting factor in natural water systems, study of the synthetic carbonates is all the more relevant. Hydrolysis tendencies will affect which carbonate phase (normal carbonate vs hydroxycarbonate) are found in natural water systems, solubility trends will demonstrate the distribution of the rare earths between solid and aqueous phases, and in mixed  $\text{RE}_2\text{O}_3 - \text{H}_2\text{O} - \text{CO}_2$  systems, quantified thermochemical differences enable predictions of which rare earth carbonate is more likely to form over the other(s), enabling separation techniques of mixed rare earths.

These property-specific trends are most evident within a systematic study and when quantification and analytical methods are self-consistent. Systematic studies generally encompass the whole rare earth spectrum or representative rare earths (yttrium + light rare earth(s) + heavy rare earth(s)) to demonstrate trends with respect to atomic number. Crystallographic trends are apparent when the same indexing methods and space groups are used. Thermal stability trends manifest with consistent atmospheres and heating conditions. Solubility and thermochemical trends require the use of the exact, desired rare earth carbonate phase to properly attribute these values.

### *2.3.1. Crystallography of the Rare Earth Carbonates*

The normal rare earth carbonates, with the general chemical formula of  $\text{RE}_2(\text{CO}_3)_3 \cdot x\text{H}_2\text{O}$ , are hydrated carbonates in which the reported degree of hydration can vary from the theoretically determined values depending upon synthesis conditions. The rare earth hydroxycarbonates have the general chemical formula of  $\text{RE}(\text{OH})\text{CO}_3 \cdot x\text{H}_2\text{O}$  that can assume the orthorhombic, hexagonal,

or tetragonal structural variants depending upon reaction conditions. It should be noted that in the study of naturally occurring RE carbonates, particularly single RE carbonates, the hydroxycarbonates are of greater importance as they are the hydrolysis products of the normal carbonates at ambient conditions ( $p\text{CO}_2 = 3 \cdot 10^{-4}$  atm, 25 °C, total pressure = 1 atm) and are also the preferred carbonate phase at elevated temperatures<sup>43–47,49</sup>.

Much prior literature regarding the crystallography of the rare earth carbonates has reported unit cell parameters, space groups, and crystal systems in isolation from one another, i.e., there is an abundance of literature that reports crystallographic parameters of one or two rare earth carbonates<sup>88,106–119</sup>. This fragmentation leads to confusion and inconsistencies in the available crystallographic data for the rare earth carbonates. Yet, literature that utilizes the same crystal systems and space groups often reports similar crystallographic parameters, such as those by Caro<sup>120</sup> and Shinn<sup>88</sup>. Authors that have systematically studied the rare earth carbonates (e.g., Caro, Wakita, Michiba, and Tahara) have utilized self-consistent indexing and synthesis methods, allowing trends in the crystallographic parameters to become apparent. For both hydroxycarbonates and normal carbonates, unit cell parameters shrink with increasing atomic number. Though such trends were not the main focus of these reports, the crystallographic data clearly indicate the trend is present.

Of the normal rare earth carbonates, the carbonates of lanthanum through neodymium are isostructural to lanthanite, an octahydrate carbonate, and the carbonates of samarium through thulium plus yttrium are isostructural to tengerite, a di-/trihydrate carbonate. Ytterbium carbonates and lutetium carbonates form hexahydrate carbonate phases that are unique from each other and the rest of the rare earths<sup>50</sup>. Scandium can form a carbonate, but is most likely to form a unique hydroxide phase. Attempts to reproducibly synthesize and characterize scandium carbonates have met with limited, if any, success<sup>121,122</sup>.

The most comprehensive studies on the normal carbonates are by Caro<sup>120</sup> and Wakita<sup>123</sup>. Caro<sup>120</sup> reported the unit cell parameters for lanthanum, praseodymium and neodymium carbonate by assigning them to the orthorhombic crystal system within the *Pccn* space group (Figure 2.5). Praseodymium and neodymium carbonate were found to be isostructural to lanthanite. Wakita<sup>123</sup> determined the unit cell parameters for the normal rare earth carbonates to be isostructural to tengerite. These were the normal carbonates of samarium, gadolinium, dysprosium, holmium, erbium, and yttrium. Wakita indexed all of the carbonates isostructural to tengerite using the *“Battelle Indexing Charts for Diffraction Patterns of Tetragonal, Hexagonal and Orthorhombic Crystals”* and assigned to the orthorhombic crystal system<sup>123</sup>. Both studies have shown that the crystallographic parameters shrink with increasing atomic number. Caro also reported increasing density with increasing atomic number, attributable to increasing atomic number and shrinking unit cell volumes. Wakita did not specifically mention or calculate unit cell density, but it can be assumed that density also increases for the tengerites with increasing atomic number as shrinking unit cell volume with increasing atomic number was explicitly reported.

The hydroxycarbonates assume two polymorphs in nature. The hexagonal hydroxycarbonates are isostructural to the hydroxyl analogs of bastnäsite and the orthorhombic hydroxycarbonates are isostructural to the ancylite group of minerals plus kozoite. The most comprehensive examinations of the hydroxycarbonate crystal structures are by Tahara<sup>124</sup> and Michiba<sup>79</sup>. Tahara<sup>124</sup> synthesized the series of orthorhombic hydroxycarbonates by the decomposition of formic acid under hydrothermal conditions. Neodymium and samarium hydroxycarbonates were assigned the *Pnma* space group, europium through thulium hydroxycarbonates were assigned the *P2<sub>1</sub>2<sub>1</sub>2<sub>1</sub>* space group, and thulium and ytterbium hydroxycarbonates were assigned the *P4<sub>2</sub>/nmc*. Like those of the normal carbonates, the reported values for the orthorhombic unit cell parameters (Figure 2.6) shrink with increasing atomic number. Michiba<sup>79</sup> reported the unit cell parameters for

the hexagonal hydroxycarbonates (Figure 2.6). The hexagonal hydroxycarbonates were synthesized via the hydrothermal decomposition of formic acid at temperatures greater than those for the orthorhombic hydroxycarbonates. All of the hydroxycarbonates were assigned the  $P6$  space group. Like the normal carbonates, both polymorphs of the hydroxycarbonates have shrinking unit cell parameters with increasing atomic number. These shrinking parameters are also accompanied by hydroxycarbonate densities that increase with increasing atomic number, which is also attributable to shrinking unit cell volumes and increasing atomic mass.

Shrinking unit cell parameters and increasing carbonate density with increasing atomic number are found in all polymorphs of the rare earth carbonates. This is true for the normal carbonates, hexagonal hydroxycarbonates, and orthorhombic hydroxycarbonates. As previously discussed, these trends only exist when consistent methods of analysis and synthesis are applied to the systematic study of rare earth carbonate crystallography. For the hydroxycarbonates, lattice parameters reported by many different groups do not greatly vary from those of Tahara or Michiba. This can be attributed to the well understood crystallography and easily controllable chemical composition of the hydroxycarbonates. The values for the respective rare earth hydroxycarbonates from Beall<sup>110</sup>, Dal Negro<sup>125</sup>, Christensen<sup>107</sup>, Dexpert<sup>126</sup>, Doert<sup>109</sup>, and Kutlu<sup>108</sup> (Figure 2.6) are very similar to those presented by Tahara<sup>124</sup> and Michiba<sup>79</sup>.

Unlike the hydroxycarbonates, the reported values for the normal carbonates are rather inconsistent when considering a wider body of literature. These differing values can be attributed to different synthesis methods, degrees of hydration, particle size, and choice of crystal system. In many attempts to characterize the crystallography of the normal carbonates, the exact degree of hydration varies widely and the stoichiometry of the carbonate will vary, though it may not be reported as such. Based upon the general chemical formula of  $RE_2(CO_3)_3 \cdot xH_2O$ , the  $RE_2O_3:CO_2$  ratio should be as close to 1:3 as possible, with the amount of water being released upon

decomposition dependent upon the exact rare earth. The  $\text{RE}_2\text{O}_3:\text{CO}_2$  ratio is affected by the hydrolysis of the carbonates, of which those of cerium through europium tend to hydrolyze into the hydroxycarbonate, and degrees of hydration are sensitive to drying conditions<sup>86</sup>. Further deviations can be attributed to contamination by precipitation agents, such as sodium/potassium carbonates, where prolonged exposure of the rare earth carbonates to aqueous solutions of alkali carbonates will create the double carbonate<sup>36–42</sup>.

The crystallographic parameters we have selected as representative of the carbonates are based upon the following. For the hydroxycarbonates, these are the values that have been accepted into the Inorganic Crystal Structure Database (ICSD)<sup>79,124</sup>. For the normal carbonates, the values for the lanthanites have been indexed using the same method for the diffraction pattern and crystallographic parameters accepted into the ICSD for lanthanum carbonate octahydrate by Shinn<sup>88</sup>. The values for the tengerites by Wakita should be approached with a little more caution than those of the lanthanites as the ICSD does not include these values. The diffraction pattern and crystallographic pattern for tengerite in the ICSD is that by Miyawaki<sup>112</sup>, who assigned a different space group to the synthetic yttrium carbonate than that of Wakita but Miyawaki's work has been heavily influenced by Wakita's prior works.

### *2.3.2. Thermochemical Properties of the Rare Earth Carbonates*

The thermochemical properties for the rare earth carbonates are differentiated into the distinct crystal systems for the normal carbonates and the hydroxycarbonates. Considering the distinct chemical nature(s) of the different rare earth carbonates, the thermochemical properties for the hydrated normal carbonates are not the same as those for the anhydrous normal carbonates. Likewise, the thermochemical properties for the hexagonal hydroxycarbonates are not the same as those for orthorhombic hydroxycarbonates. Thermochemical properties for the rare earth



carbonates have been determined by both calorimetric and solubility means, with some studies utilizing both methods to demonstrate that both are valid methodologies<sup>127</sup> when carefully performed and can arrive at similar thermochemical values. When done correctly, calorimetric methods of deriving enthalpies of formation can be accomplished in relatively short time periods (minutes/hours vs. weeks/months) compared to solubility methods. Solubility methods<sup>127–131</sup> require extraordinarily long time points to ensure that thermodynamic equilibrium has been established. In addition, solubility experiments also dictate that the initial and final solid phase in contact with water are the same, i.e., the experimental conditions should not result in a change of the crystallographic phase or chemical composition during the course of the equilibration. For phases with extremely low solubility, like the rare earth carbonates, appropriate adjustments in ionic strength and pH are utilized to increase the solubility of the solid phase(s) to concentration levels that can be accurately measured<sup>130,131</sup>.

The hydrated normal carbonates can be classified along the same lines as per their crystallography: the octahydrate lanthanites, the di-/trihydrate tengerites, and the hexahydrates of ytterbium and lutetium. It should be noted that thermochemical properties for scandium carbonate are not presented as no definitive conclusion has been reached in literature regarding the exact composition of scandium carbonate, if it exists at all<sup>121,122</sup>. The thermochemical values of the hydrated normal carbonates by Karapet'yants<sup>129,132</sup> (Figure 2.7) makes this apparent, with three distinct “levels” of thermochemical values (Gibbs free energies and enthalpies of formation). Though the report makes scant mention of the crystallographic identities, we assume that these hydrates are the isostructural groups associated with the degrees of hydration as the amount of water is strongly linked to the crystallographic phase<sup>6</sup>.

The Gibbs free energies and enthalpies for the anhydrous normal carbonates are smaller in magnitude than those for the hydrated normal carbonates (Figure 2.7). The difference in the

thermochemical quantities between the respective anhydrous and hydrated carbonates can be correlated with the enthalpy of hydration. Both Gibbs free energies and enthalpies of formation for the anhydrous normal carbonates decrease in magnitude with increasing atomic number, with a europium exception attributed to a strong tendency to form the divalent cation. This trend directly carries over to the hydrated carbonates and is found within the isostructural carbonate groups (i.e., lanthanites, tengerites, and hexahydrates).

The thermochemistry of the hydroxycarbonates is separated between the orthorhombic and hexagonal polymorphs, which are isostructural to ancylite and hydroxyl-bastnaesite, respectively. This requires that the presented thermochemical values account for the distinction between these two phases. Compared to studies of the thermochemical properties for the normal carbonates, studies of the thermochemistry of the hydroxycarbonates are not as extensive, but have been conducted more recently. Studies by Rorif<sup>127</sup> and Shivaramaiah<sup>99</sup> (Figure 2.8) have determined the enthalpies of formation for a number of hydroxycarbonates spanning the rare earths. In general, the enthalpies of formation for both hexagonal and orthorhombic hydroxycarbonates decrease in magnitude with increasing atomic number, and the hexagonal hydroxycarbonates are lower in magnitude than the orthorhombic hydroxycarbonates. The comparison of the orthorhombic and hexagonal hydroxycarbonates by Rorif<sup>127</sup> has led to the determination that though the orthorhombic hydroxycarbonates may be isolated at standard conditions, the orthorhombic carbonates are metastable compared to their hexagonal polymorphs.

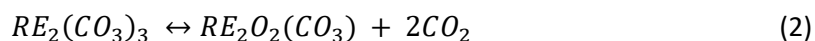
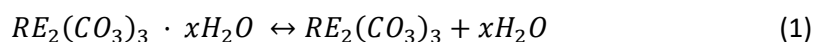
Overall, the present body of thermochemical values has allowed us to draw the following conclusions: the hydrated normal carbonates form preferentially hydroxycarbonates at standard conditions, the orthorhombic hydroxycarbonates are preferred over the hexagonal hydroxycarbonates at standard conditions, and thermochemical properties for normal carbonates

and hydroxycarbonates decrease in magnitude with increasing atomic number. However, additional studies into the thermochemistry of other hydroxycarbonates such as those of holmium, erbium, ytterbium, and gadolinium will flesh out the body of literature available. Literature on the thermochemical parameters for the normal carbonates may require revisiting as the work by Karapet'yants<sup>129,132</sup> was conducted over 40 years ago. More recent analytical methodologies may prove beneficial to refining and improving the thermochemical quantities for the hydrated normal carbonates<sup>130,131</sup>.

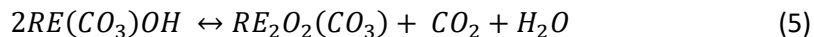
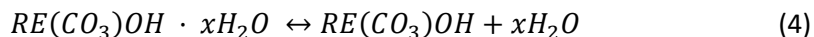
### 2.3.3. Thermal Behavior of the Rare Earth Carbonates

Literature regarding the thermal behavior of the rare earth carbonates has attempted to identify certain trends, intermediate phases, or simply show the decomposition profile to demonstrate that they have synthesized the desired rare earth carbonate. In general, all rare earth carbonates will follow the sequence of dehydration, partial decarbonation, and full decarbonation. The dehydration process can account for 5 to 20% of the mass loss; the lanthanites can lose up to 23% of their initial mass due to dehydration. Dehydration mainly occurs below 100 °C with any additional water, or crystalline water in the hydroxycarbonates, being lost between 200 and 500 °C. Following dehydration, the carbonate will partially decompose into an oxycarbonate. The oxycarbonate will then decompose into the respective oxide.

The normal carbonates in general follow the decomposition pathway of:



The hydroxycarbonates in general follow the decomposition pathway of:



Thermal decomposition profiles are affected by the decomposition atmosphere and heating rate. Relative to air, humidified air will not stabilize the hydrates or water bearing phases, CO<sub>2</sub> atmospheres will stabilize all carbonate phases, and vacuum atmospheres will expedite the decomposition of all phases<sup>84,85</sup>. High heating rates can mask the existence of intermediate phases<sup>89,90,133,134</sup> and make the accurate identification of phase transitions difficult. With all that said, most systematic studies on the thermal decomposition of both hydrated normal carbonates and hydroxycarbonates do not necessarily present specific values according to which the onset of thermal decomposition, and therefore trends across the rare earths, can be identified. This makes the specific identification of trends difficult, but correlations with increasing atomic number have been reported. In general, the decomposition temperature for all rare earth carbonates and all intermediate phases (anhydrous and oxycarbonate) trends downwards with increasing atomic number. It should be noted that the thermal decomposition of the rare earth oxycarbonates have been previously characterized<sup>86,135–137</sup>.

Comprehensive studies of the normal carbonates by Head<sup>84,85</sup>, Domingues and coworkers<sup>133,134</sup>, Wendlandt<sup>138</sup>, and Foger<sup>139</sup> demonstrate correlations in the stability of the representative intermediate carbonate with respect to atomic number. In general, the intermediate carbonate phases, the anhydrous normal carbonate and dioxymonocarbonate, will trend toward lower decomposition temperatures in air with increasing atomic number. It should be noted that this correlation is not perfect<sup>84,85</sup> and these exceptions, such as the greater decomposition temperature of gadolinium carbonate(s) over the europium carbonates, multiple dehydrations

steps for neodymium carbonate<sup>89</sup>, and the complex decomposition of praseodymium carbonate<sup>90</sup>, can be attributed to the unique electron configurations of the respective rare earths.

In contrast to the normal carbonates, the thermal decomposition behavior of the hydroxycarbonates has not been as comprehensively studied. A limited number of studies on the hydroxycarbonates by Eyring<sup>89,90</sup>, Charles<sup>83</sup>, and D'Assuncao<sup>140</sup> have demonstrated the general decomposition pathway as outlined by equations 3 – 5. Charles<sup>83</sup> gives a relatively qualitative view on the decomposition pathways of the hydroxycarbonates and the studies by Eyring<sup>89,90</sup> are in general agreement with this decomposition pathway.

D'Assuncao<sup>140</sup> has given one of the most comprehensive reports on the decomposition profiles of the rare earth hydroxycarbonates, but it should be noted that no mention of crystal phase for the rare earth hydroxycarbonates was given and thus it is difficult to assess to which hydroxycarbonate phase the results can be ascribed. Specific transition temperature(s) were also not reported as the high heating rates, which have also been known to shift the transition/decomposition temperature higher<sup>89,90,133,134</sup>, most likely made this very difficult. Based on the provided decomposition profiles and associated decomposition temperature ranges, we make the following conclusions:

- 1) Decreasing carbonate product crystallinity (lack of distinct plateaus in decomposition profiles) with increasing atomic number, with the relatively high heating rate (~20 °C/min), makes decomposition transition temperature difficult to identify
- 2) Dehydration of the hydroxycarbonates, due to their greater amorphous nature, occurs at much lower temperatures than those of the lighter hydroxycarbonates.

- 3) Within the lighter hydroxycarbonates (La – Eu), the temperature at which the partial decarbonation to form an oxycarbonate occurs trends downwards with increasing atomic number.
- 4) Oxycarbonate decomposition temperature trends downwards with increasing atomic number, which was also found for the oxycarbonates of the hydrated normal carbonates.

It should be noted that few if any of these observed decompositions represent equilibrium reactions, with these observations being kinetic rather than thermodynamic. These reactions have not been shown in these studies to be reversible and particle sizes were not necessarily controlled. Since particle size and therefore particle packing was not necessarily controlled, deviations in decomposition temperature due to these factors were also not controlled. Yet, these studies provide valuable insight into the thermal decomposition of the carbonates.

In comparing the available literature on the thermal decomposition of the rare earth carbonates, the normal carbonates have been better studied with many reporting the same downward trend in decomposition temperature of all intermediate phases with increasing atomic number. No distinct trend across the entire rare earth series could be established for the hydroxycarbonates due to the isolated nature of the literature, studying only one hydroxycarbonate at a time, and the high heating rate used in the most encompassing study. To firmly establish decomposition temperature trends, for either normal carbonates or hydroxycarbonates, with respect to atomic number, future studies should utilize extremely low heating rates (e.g., 0.25 °C/min)<sup>84,85,89,90</sup>, same crystallography (i.e., normal carbonates vs. hexagonal hydroxycarbonates vs. orthorhombic hydroxycarbonates), and same atmosphere (e.g., air or CO<sub>2</sub>)<sup>84,85</sup>.

#### *2.3.4. Behavior of Rare Earth Carbonates in Aqueous Environments*

The rare earth carbonates are known for two particular behavior patterns in water: they are very insoluble but undergo hydrolysis. Both normal carbonates and hydroxycarbonates are very insoluble in water, with systematic studies such as those by Jordanov<sup>141</sup>, Caro<sup>48</sup>, Spahiu<sup>142</sup>, and Rorif<sup>127</sup> showing  $K_{sp}$  values on the order of  $10^{-20}$  to  $10^{-35}$ . Yet, insolubility does not translate to resistance to hydrolysis. At ambient conditions, Caro demonstrated the tendency of the lighter normal rare earth carbonates (La – Eu) to readily hydrolyze while the heavier normal carbonates are resistant to hydrolysis<sup>49</sup>. All normal rare earth carbonates will hydrolyze into their respective hydroxycarbonates in water when temperature is increased close to 100 °C. Studies on the hydrothermal behavior of the  $RE_2O_3 - CO_2 - H_2O$  ternary system by Kutty and coworkers<sup>43–47</sup> show that at isobaric conditions (fixed mole fraction  $CO_2$ ) the hydroxycarbonates are the preferred phase at elevated temperatures.

The normal carbonates have  $K_{sp}$  on the order of  $10^{-30}$  to  $10^{-35}$  (Figure 2.9), much lower than the those of the hydroxycarbonates ( $10^{-15}$  to  $10^{-20}$ ), as determined at neutral pH and with sufficient  $pCO_2$ . Since solubility measurement requires that the solid in contact with water does not undergo a chemical change, this extremely low normal carbonate solubility is relevant with the caveat that the applied  $pCO_2$  prevents hydrolysis into the hydroxycarbonate. Caro demonstrated that the normal carbonates are stable at a  $pCO_2$  of 1 atm<sup>50</sup>. Both Jordanov<sup>141</sup> and Caro<sup>48</sup> utilized this knowledge to obtain solubility data on the entire series of normal carbonates, demonstrating increasing solubility with increasing atomic number. Normal yttrium carbonate falls within the expected range based upon ionic radius of the trivalent cation (Figure 2.9). Analysis of multiple solubility reports by Spahiu<sup>142</sup> have also concluded this general trend. Other collections of systematically acquired solubility data all show varying degrees of solubility for each of the carbonates, but in general demonstrate increasing solubility with increasing atomic number.

In general, the solubility of the normal carbonates increases with increasing atomic number. Solubility products for the hexagonal and orthorhombic hydroxycarbonates are from Rorif<sup>127</sup>. No trend with respect to atomic number may be established, but the orthorhombic carbonates are in general more soluble than their hexagonal counterparts.

Hydroxycarbonate solubility, for both orthorhombic and hexagonal phases, has been explored on a limited basis. Many of these studies have focused on the lighter lanthanide carbonates, particularly neodymium carbonate as it is a chemical homologue for radioactive actinide carbonates<sup>16,19</sup>. As such, understanding their aqueous solubility has been crucial as the hydroxycarbonate phases are the solubility limiting phases in natural water systems in the distribution of actinides/lanthanides. Yet, comprehensive studies on a scale similar to those of the normal carbonates are scarce. Rorif<sup>127</sup> presented a comparison of the aqueous solubilities of the hexagonal and orthorhombic lanthanum, neodymium, samarium, and europium hydroxycarbonates. Though no trends with respect to atomic number can be established, there is a marked difference in solubility between the hexagonal and orthorhombic hydroxycarbonates ( $K_{sp} = 10^{-23} - 10^{-25}$  vs.  $10^{-20} - 10^{-22}$ , respectively). Across the board, the orthorhombic hydroxycarbonates are more soluble than their respective hexagonal hydroxycarbonates (Figure 2.9).

#### **2.4. Final Remarks**

The rare earth carbonates, both normal and hydroxycarbonates, are important in understanding the distribution of rare earths in geological settings. Since the rare earths are chemically related to the actinides, understanding the behavior of the rare earths also furthers our knowledge of the distribution and chemistry of nuclear fuels and radioactive actinides in natural water systems, which contain CO<sub>2</sub>. Industrial production of rare earth solids fundamentally requires a consistent



and sound understanding of the crystallographic, thermochemical, thermal decomposition, and aqueous properties of the rare earth carbonates. Since many geological sources of rare earths are enriched carbonate minerals and the downstream production of other rare earth solids begins with the rare earth carbonates, the fully comprehensive understanding of these properties is of utmost importance. With that said, the current understanding of physical and chemical properties of the rare earth carbonates has been limited to extrapolations based upon what has been explored, i.e., representative rare earths for the light, middle, and heavy rare earths. As in the case of nuclear fuel applications, neodymium and europium carbonates/hydroxycarbonates have been studied as chemical homologues for americium.

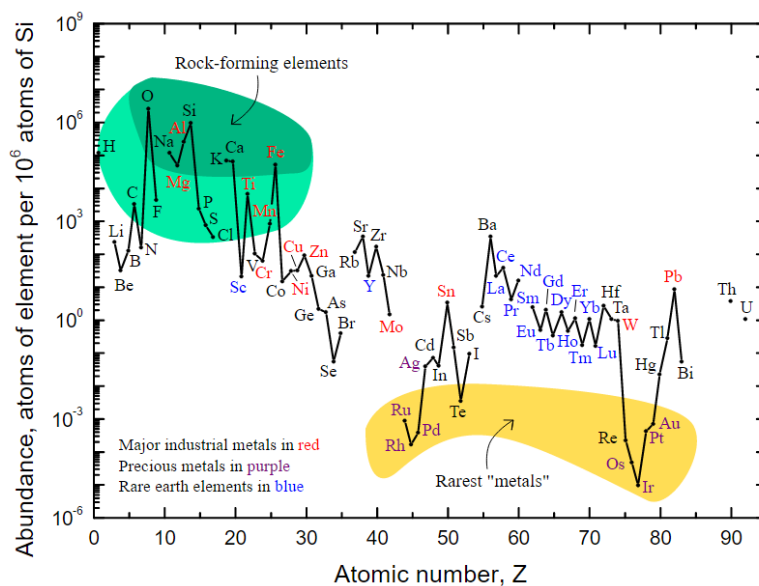
Trends in crystallography, thermochemistry, aqueous behavior, and thermal decomposition of the rare earth carbonates have informed us that physical and chemical parameter trends with respect to atomic number found for the rare earth elements also carry over to the carbonates. The shrinking lattice parameters, decreasing magnitude in thermochemical parameter(s), downward trending decomposition temperatures, and increasing solubility with increasing atomic number have basis within the concept of the lanthanide contraction and the chemical implications thereof. However, these parameters and trends can yet benefit from further refinement and studies. The lattice parameters for the normal carbonates, besides those for lanthanite-(La) and tengerite-(Y), are not found in ICSD, whilst those for the hydroxycarbonates for both hexagonal and orthorhombic polymorphs can be accessed through ICSD. The most comprehensive studies of normal carbonate thermochemistry can only be found in obscure compilations such as that by Karapet'yants. More easily accessible compilations contain the thermochemical values for singular carbonates or the anhydrous variants. Hydroxycarbonate thermochemistry is limited to the lighter rare earths with a small sampling of the heavier rare earths. The aqueous solubility of the carbonates is subject to the same limitations as the available

thermochemical literature, i.e., normal carbonate solubility is found in obscure literature or data for anhydrous variants are reported as valid for hydrated variants, and hydroxycarbonate solubility is limited to the lighter rare earths plus a sampling of the heavier rare earths. The thermal decomposition profiles and our understanding thereof for all carbonates would benefit from reevaluation. By utilizing extraordinarily slow heating rates, standardized atmospheres, and standardized transition analyses, firmer correlations may be established in the already established general correlation in the downward trending decomposition temperature with increasing atomic number. Updating these values and making them readily accessible would benefit our understanding of the rare earth elements.

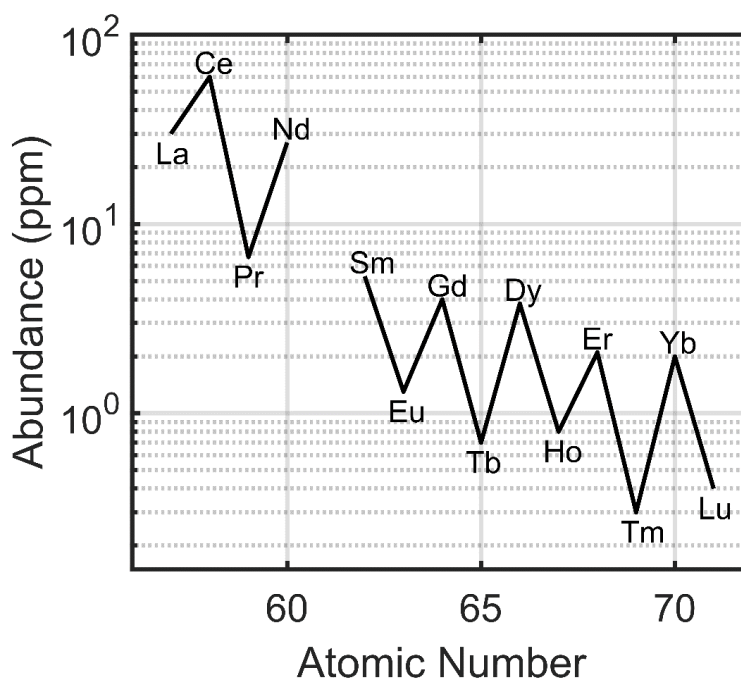
## 2.5. Figures

Applications of the Rare Earth Elements	
Rare Earth Element	Broad Uses
Scandium	Lasers, Ceramics, Phosphors, and High Performance Alloys
Yttrium	Phosphors, Lasers, Ceramics, Superconductors, and Optical Lenses
Lanthanum	NiMH batteries, petroleum catalysts, hydrogen storage, optical materials, and phosphors
Cerium	Catalysts, glass additives, ceramics, phosphors, metal refining, and phosphors
Praseodymium	Ceramic additive (coloring), permanent magnet additive, scintillators, and telecommunications
Neodymium	Permanent magnets, lasers, metal halide lamps, glass coloring, and dielectrics
Promethium	Limited uses: mainly research and small scale, beta-particle based lighting
Samarium	High temperature permanent magnets, glass coloring, phosphors, lasers, and radiation shielding
Europium	Red and blue phosphors, scintillators, and LEDs
Gadolinium	MRI contrast agents, scintillator host(s), optical lenses, fluorescent lamps
Terbium	Phosphors, magneto-optical disks, fluorescent lamps, display technologies, LEDs
Dysprosium	Permanent magnet additive and phosphors
Holmium	Metal halide lamps and research
Erbium	Fiber optic signal amplifiers, lasers, and coloring agent
Thulium	Metal halide lamps and research
Ytterbium	Optical lenses, phosphors, and research
Lutetium	Scintillator host and optical lenses

**Figure 2.1.** Applications of the rare earth elements broken down by element. Most applications are geared towards high-technology, such as lasers, magnets, phosphors, energy conversion, and catalysis. Adapted from Gschneidner, Jr<sup>2</sup>.



(a)



(b)

Figure 2.2. (a) Crustal abundances of the rare earth elements (REEs) relative to silicon (adapted from USGS<sup>5</sup>) and each other (adapted from Gupta<sup>15</sup>). (b) REEs are relatively abundant compared to palladium group metals (e.g., palladium, platinum, and rhodium).

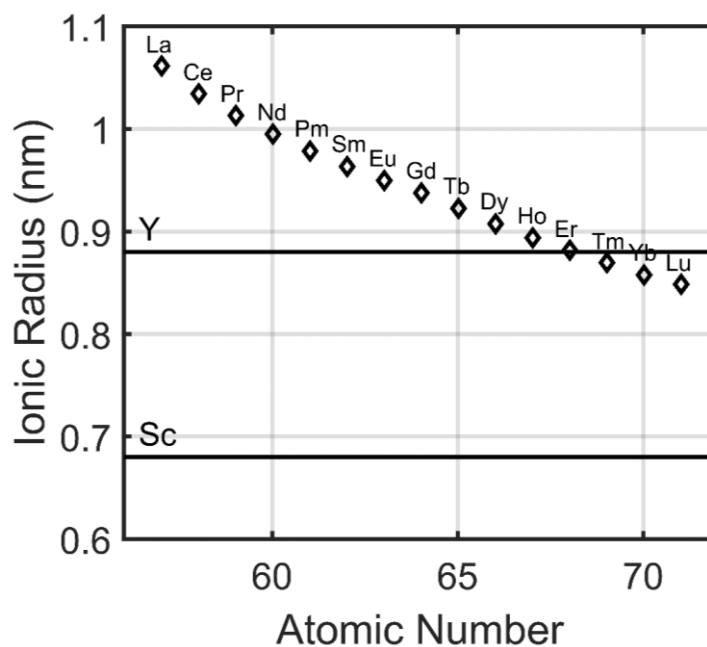


**Figure 2.3.** Ionic radius of the trivalent rare earth (RE) cations (adapted from Gupta<sup>15</sup>). Lanthanide contraction is observed due to the weak shielding of the valence electrons by the 4f electrons. Certain properties of rare earth carbonate phases can be correlated with atomic number.

**Electronic Configuration of  
Common Rare Earth Oxidation States**

	Atomic	2+	3+	4+
Scandium	[Ar]3d <sup>1</sup> 4s <sup>2</sup>	-	[Ar]	-
Yttrium	[Kr]4d <sup>1</sup> 5s <sup>2</sup>	-	[Kr]	-
Lanthanum	[Xe] 4f <sup>0</sup> 5d <sup>1</sup> 6s <sup>2</sup>	-	[Xe]4f <sup>0</sup>	-
Cerium	[Xe]4f <sup>1</sup> 5d <sup>1</sup> 6s <sup>2</sup>	-	[Xe]4f <sup>1</sup>	[Xe]4f <sup>0</sup>
Praseodymium	[Xe]4f <sup>3</sup> 6s <sup>2</sup>	-	[Xe]4f <sup>2</sup>	[Xe]4f <sup>1</sup>
Neodymium	[Xe]4f <sup>4</sup> 6s <sup>2</sup>	-	[Xe]4f <sup>3</sup>	[Xe]4f <sup>2</sup>
Promethium	[Xe]4f <sup>5</sup> 6s <sup>2</sup>	-	[Xe]4f <sup>4</sup>	-
Samarium	[Xe]4f <sup>6</sup> 6s <sup>2</sup>	[Xe]4f <sup>6</sup>	[Xe]4f <sup>5</sup>	-
Europium	[Xe]4f <sup>7</sup> 6s <sup>2</sup>	[Xe]4f <sup>7</sup>	[Xe]4f <sup>6</sup>	-
Gadolinium	[Xe]4f <sup>7</sup> 5d <sup>1</sup> 6s <sup>2</sup>	-	[Xe]4f <sup>7</sup>	-
Terbium	[Xe]4f <sup>9</sup> 6s <sup>2</sup>	-	[Xe]4f <sup>8</sup>	[Xe]4f <sup>7</sup>
Dysprosium	[Xe]4f <sup>10</sup> 6s <sup>2</sup>	-	[Xe]4f <sup>9</sup>	[Xe]4f <sup>8</sup>
Holmium	[Xe]4f <sup>11</sup> 6s <sup>2</sup>	-	[Xe]4f <sup>10</sup>	-
Erbium	[Xe]4f <sup>12</sup> 6s <sup>2</sup>	-	[Xe]4f <sup>11</sup>	-
Thulium	[Xe]4f <sup>13</sup> 6s <sup>2</sup>	[Xe]4f <sup>13</sup>	[Xe]4f <sup>12</sup>	-
Ytterbium	[Xe]4f <sup>14</sup> 6s <sup>2</sup>	[Xe]4f <sup>14</sup>	[Xe]4f <sup>13</sup>	-
Lutetium	[Xe]4f <sup>14</sup> 5d <sup>1</sup> 6s <sup>2</sup>	-	[Xe]4f <sup>14</sup>	-

**Figure 2.4. Electron configuration of the REE cations (adapted from Gupta<sup>151</sup>).**

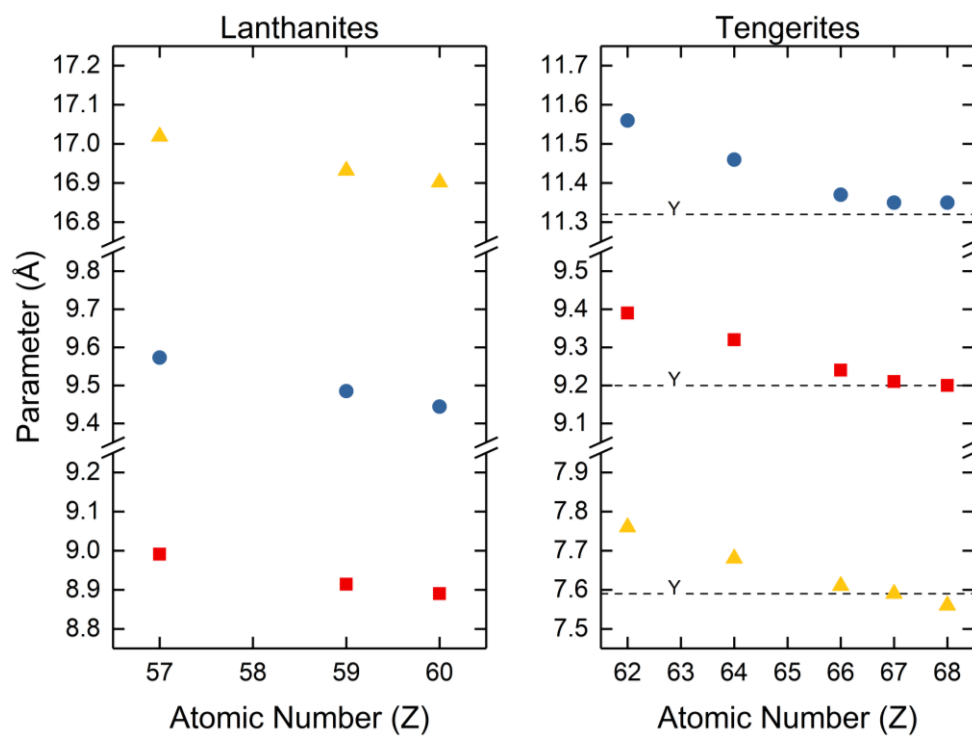


**Figure 2.5.** Lattice parameter data for the lanthanites and tengerites, the normal rare earth carbonate hydrates. Values for the lanthanites are from Caro and coworkers<sup>120</sup>. Values for the tengerites are from Wakita and coworkers<sup>123</sup>.

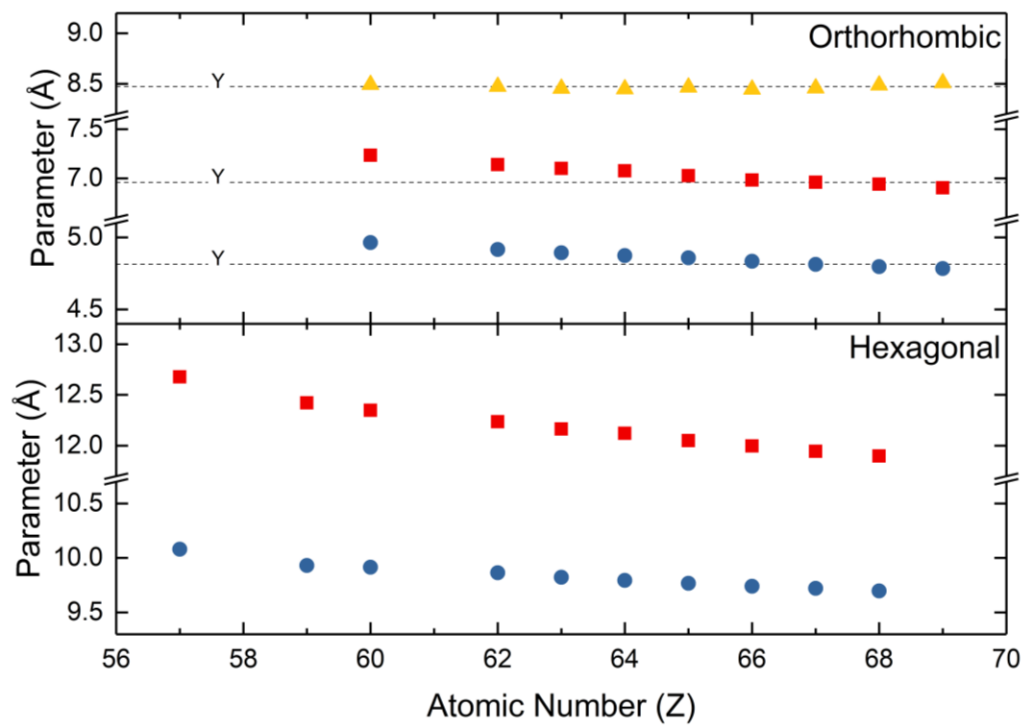


**Figure 2.6.** Lattice parameters for the orthorhombic and hexagonal rare earth hydroxycarbonates. Values for the orthorhombic hydroxycarbonates are from Tahara<sup>124</sup>. Values for the hexagonal hydroxycarbonates are from Michiba<sup>79</sup>.



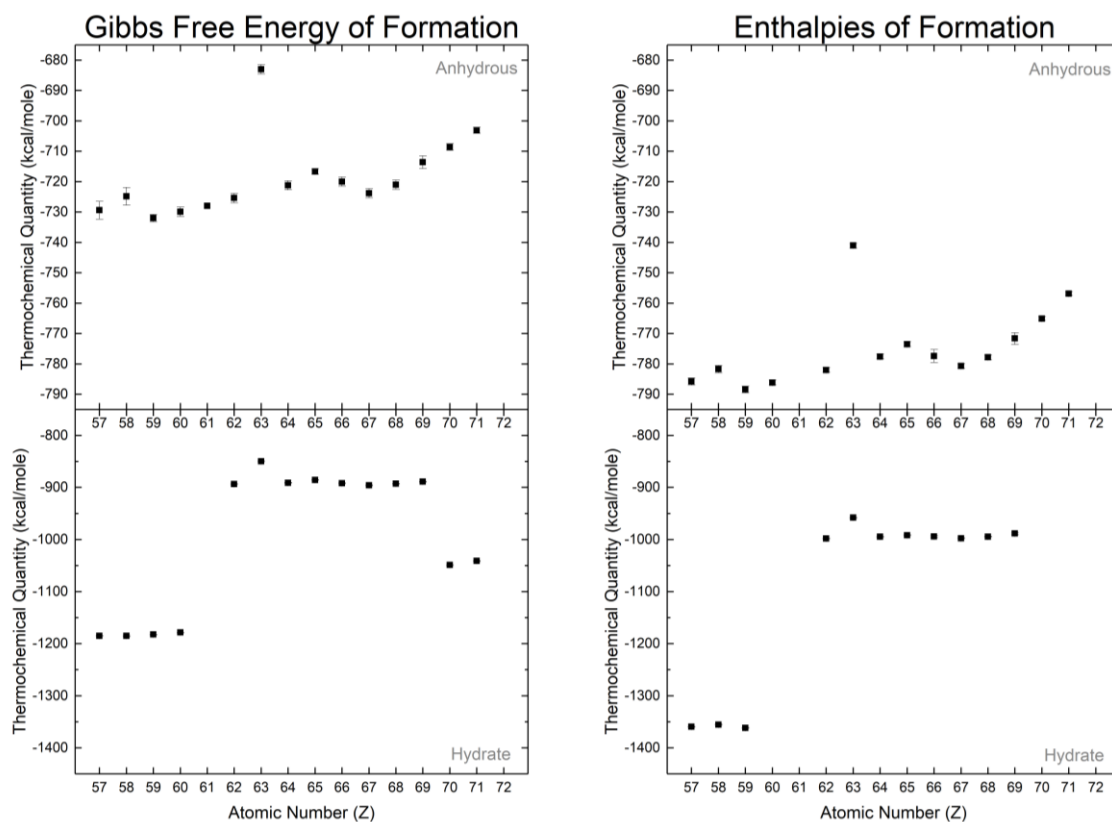


**Figure 2.7.** Gibbs free energies of formations and enthalpies of formation from Karapet'yants<sup>129, 132</sup>. Hydration of the rare earth carbonates masks decreasing thermochemical values with respect to atomic number as observed in the anhydrous phases.

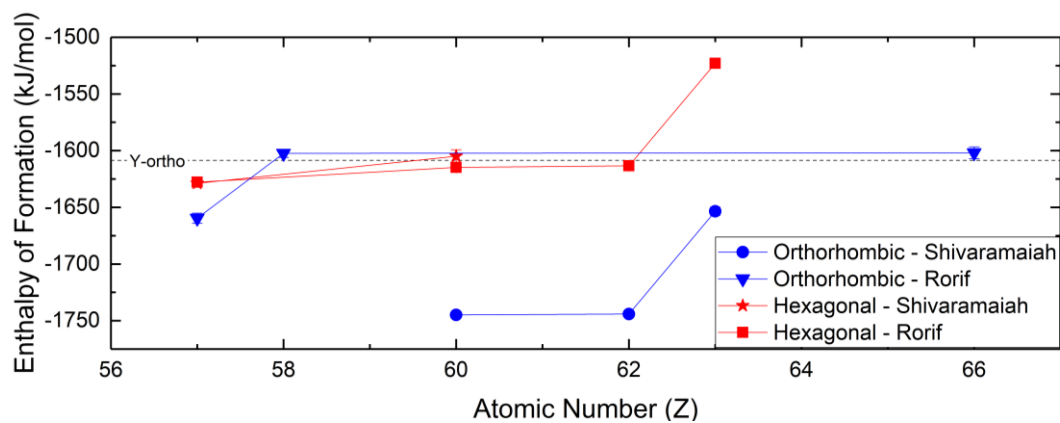


**Figure 2.8.** Enthalpies of formation for hexagonal and orthorhombic hydroxycarbonates from Rorif<sup>127</sup> and Shivaramaiah<sup>99</sup>. Value for orthorhombic yttrium hydroxycarbonate is from Shivaramaiah<sup>99</sup>.

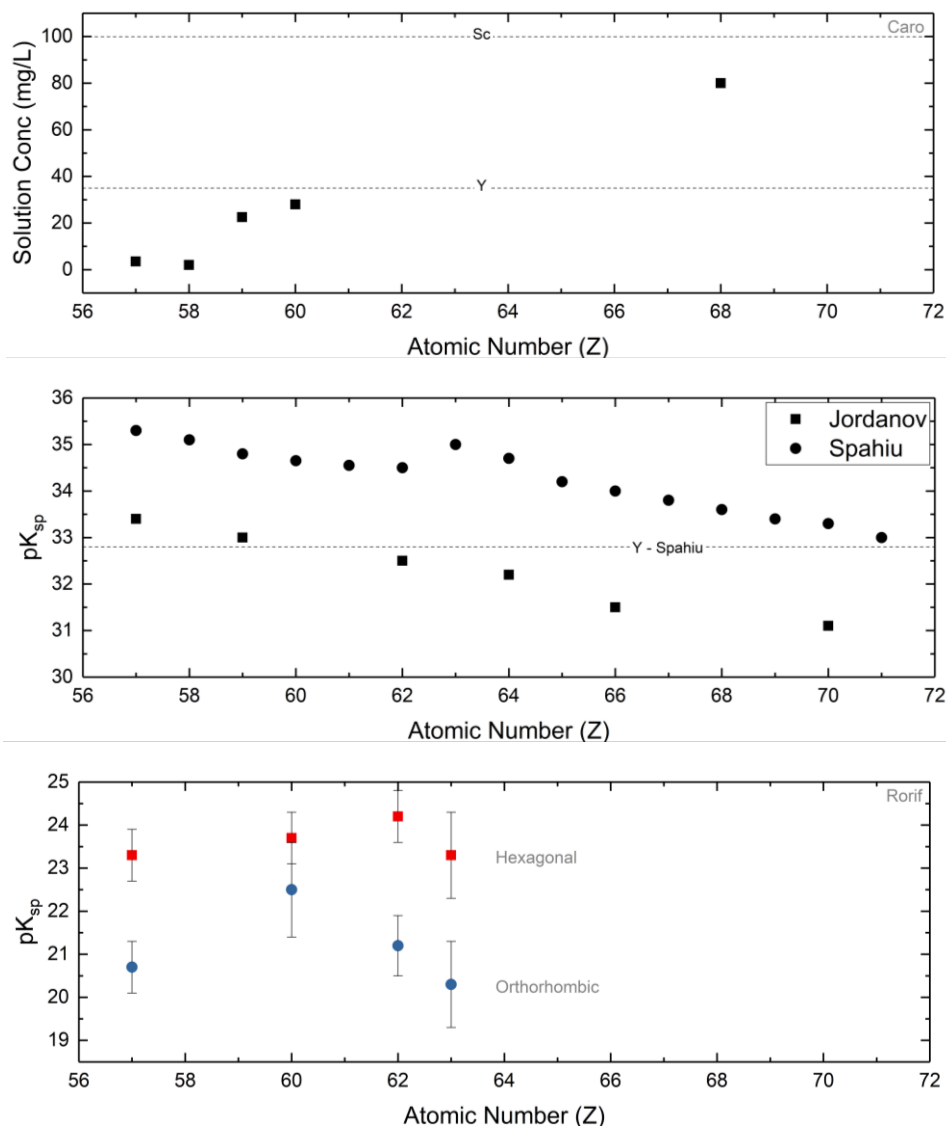


**Figure 2.9.** Solubility products and raw data for the normal carbonates are presented from Caro and coworkers<sup>48</sup>, Jordanov<sup>141</sup>, and Spahiu<sup>142</sup>. In general, the solubility of the normal carbonates increases with increasing atomic number. The dotted lines are the values for scandium carbonate and yttrium carbonate as reported by the respective authors and are presented for reference. Solubility products for the hexagonal and orthorhombic hydroxycarbonates are from Rorif<sup>127</sup>. No trend with respect to atomic number may be established, but the orthorhombic carbonates are in general more soluble than their hexagonal counterparts.

## 2.6. References

1. CMI. Critical Materials Institute - Grand Challenge Problems.
2. Gschneidner, Jr, K. A. The Rare Earth Crisis — The Supply / Demand Situation for 2010 – 2015. *Mater. Matters* **6**,
3. Connelly, N. G., Damhus, T., Hartshorn, R. M. & Hutton, A. T. *Nomenclature of inorganic chemistry - IUPAC recommendations 2005. Division of Chemical Nomenclature and Structure Representation* (2005). doi:10.1515/ci.2005.27.6.25
4. Emsley, J. *Nature's Building Blocks: An A-Z Guide to the Elements*. Oxford University Press (2011). doi:978-0-19-960563-7
5. Haxel, G. B., Hedrick, J. B. & Orris, G. *Rare Earth Elements - Critical Resources for High Technology*. United States Geological Survey (2002).
6. Railsback, L. B. Patterns in the Compositions, Properties, and Geochemistry of Carbonate Minerals. *Carbonates & Evaporites* **14**, 1–20 (1999).
7. Castor, S. B. The Mountain Pass rare-earth carbonatite and associated ultrapotassic rocks, California. *Can. Mineral.* **46**, 779–806 (2008).
8. Le Bas, M. J. *et al.* Carbonatite dykes at bayan Obo, inner Mongolia, China. *Mineral. Petrol.* **46**, 195–228 (1992).
9. Zhou, Z., Gongyuan, L., Tongyun, S. & Yuguan, L. On the geological characteristics and the genesis of the dolomitic carbonatites at Bayan Obo, Inner Mongolia. *Geol. Rev.* **26**, 35–42 (1980).
10. U.S. Geological Survey. *Mineral Commodities Summary 2011*. (2011). doi:10.1029/92GL00258
11. U.S. Geological Survey. *Mineral Commodity Summaries 2012*. (2012).
12. U.S. Geological Survey. *Mineral Commodities Summaries 2015 - Rare Earths*. Earth (2015).
13. U.S. Geological Survey. *Mineral Commodity Summaries 2016*. *Mineral Commodity Summaries* (2016). doi:http://dx.doi.org/10.3133/70140094.
14. Hurst, C. China's Rare Earth Elements Industry: What Can the West Learn? *Inst. Anal. Glob. Secur.* **43** (2010).
15. Gupta, C. K. & Krishnamurthy, N. *Extractive metallurgy of rare earths*. (CRC Press LLC, 2004).
16. Carroll, S. A. Precipitation of Nd-Ca carbonate solid solution at 25°C. *Geochim. Cosmochim. Acta* **57**, 3383–3393 (1993).
17. Meinrath, G. & Takeishi, H. Solid-liquid equilibria of Nd<sup>3+</sup> in carbonate solutions. *J. Alloys Compd.* **194**, 93–99 (1993).
18. Meinrath, G. & Kim, J. I. Solubility products of different Am (III) and Nd (III) carbonates. *Eur. J. Solid State Inorg. Chem.* **28**, 383–388 (1991).

19. Runde, W., Meinrath, G. & Kim, J. I. A Study of Solid-Liquid Phase-Equilibria of Trivalent Lanthanide and Actinide Ions in Carbonate Systems. *Radiochim. Acta* **58–9**, 93–100 (1992).
20. Zhao, D. & Pan, X. Precipitation of rare earth with carbonic acid. 4 (1991).
21. Yu, Q. & Li, X. Formation of crystalline rare earth carbonates from ore leaching liquors. *Zhongguo Xitu Xuebao* **11**, 171–173 (1993).
22. Vladescu, C. M. & Iusein, G. Separation of cerium from trivalent lanthanides. 3 (1985).
23. Tselik, I. N., Shvartsman, V. Y. & Fedorenko, V. D. Composition and thermal stability of carbonates of yttrium group rare earth elements. *Zhurnal Neorg. Khimii* **13**, 106–112 (1968).
24. Tong, Z., Chen, W. & Guan, X. Manufacture of rare earth carbonates from rare earth sulfates. 10 (1994).
25. Schmitt, A., Lorenz, H., Richter, H. & Kunze, G. Discontinuous process for the precipitation of rare earth carbonates from aqueous solutions containing other anions and cations. 4 (1986).
26. Osipova, T. P., Kharakoz, A. E. & Bleshinskii, S. V. Composition of precipitates obtained during the reaction of sodium carbonate with the salts of rare earth elements. *Fiz.-Khim. Issled. Redkozemel. Elem.* 52–60 (1972).
27. Osipova, T. P., Bleshinskii, S. V. & Kharakoz, A. E. Sodium carbonate as a reagent for the precipitation of rare earth elements. in (ed. Tananaev, I. V) 27–29 (Khim. Svoistva Soedin. Redkozemel. Elem., Dokl. Vses. Soveshch. Fiz.-Khim. Primen. Redkozemel. Elem., Ikh Soedin. Splavov, 6th, 1973).
28. Liu, S. & Ma, R. Preparation by crystalline precipitation of mixed rare earth carbonates. *Zhongguo Youse Jinshu Xuebao* **8**, 331–334 (1998).
29. Li, Y., Li, M., He, X., Hu, P. & Gu, Z. Precipitation and crystallization of rare earth carbonate. *Zhongguo Youse Jinshu Xuebao* **9**, 165–170 (1999).
30. He, L. & Gu, Z. Carbonate in separation of mixed rare earth metals. 7 (1991).
31. He, D., Liao, L. & Xu, R. Precipitation of rare earths with a mixed precipitant. 6 (1989).
32. Fischer, W., Muller, J. & Niemann, K. E. Separation of the rare earths by fractional precipitation of their carbonates. *Zeitschrift fuer Anorg. und Allg. Chemie* **282**, 63–79 (1955).
33. da Silva Queiroz, C. A. & Abrao, A. Behavior of rare earth (La, Ce, Pr, Nd, Sm) carbonates in ammonium carbonate and ammonium carbonate/ammonium hydroxide solution. *Publicacao ACIESP* **89**, 187–200 (1993).
34. Sylvester, C. *An Elementary Treatise on Chemistry Comprising The Most Important Facts of the Science, with Tables of Decomposition; To Which Is Added, An Appendix, Giving an Account of the Latest Discoveries.* (1809). doi:10.1016/0003-6870(73)90259-7
35. Reid, H. *Popular Treatise on Chemistry. I. Chemistry of Nature.* (1834). doi:10.1016/0003-6870(73)90259-7
36. Roscoe, H. E. & Schorlemmer, C. *A Treatise on Chemistry. Volume II. - Metals.* (Macmillan and Co., 1879).

37. Treadwell, F. P. *Analytical Chemistry Quantitative Analysis*. (John Wiley & Sons).
38. Blitz, H. & Blitz, W. *Laboratory Methods of Inorganic Chemistry*. (John Wiley & Sons, 1909). doi:10.1016/0003-6870(73)90259-7
39. Fresenius, C. R. *Manual of Qualitative Chemical Analysis*. (John Wiley & Sons, 1913). doi:10.1016/0003-6870(73)90259-7
40. Mochizuki, A., Nagashima, K. & Wakita, H. The synthesis of crystalline hydrated double carbonates of rare earth elements and sodium. *Bull. Chem. Soc. Jpn.* **47**, 755–756 (1974).
41. Fridman, Ya. D.; Sorochan, R. I.; Sarbaev, D. S. Solubility of rare earth carbonates in potassium carbonate solutions. in *Issled. Khim. Redk. Sopotstv. Elem.* 175–184 (1966).
42. Tselik, I. N.; Deineka, G. F.; Fedorenko, V. D.; Shvartsman, V. Y. Reaction of rare-earth chlorides with potassium carbonate in solution. *Ukr. Khimicheskii Zhurnal* **35**, 1042–1045 (1969).
43. Kutty, T. R. N., Viswanathiah, M. N. & Tareen, J. A. K. Hydrothermal equilibria in  $\text{Nd}_2\text{O}_3$  -  $\text{H}_2\text{O}$  -  $\text{CO}_2$  System. *Proc. Indian Acad. Sci. - Chem. Sci.* **87A**, 69–74 (1978).
44. Mohamed, I., Tareen, J. A. K. & Kutty, T. R. N. Hydrothermal phase equilibria in  $\text{Er}_2\text{O}_3$ - $\text{H}_2\text{O}$ - $\text{CO}_2$  and  $\text{Tm}_2\text{O}_3$ - $\text{H}_2\text{O}$ - $\text{CO}_2$  systems. *Proc. Indian Acad. Sci. - Chem. Sci.* **93**, 785–793 (1984).
45. Kutty, T. R. N., Mohamed, I. & Tareen, J. A. K. Hydrothermal phase equilibria in  $\text{Ln}_2\text{O}_3$ - $\text{H}_2\text{O}$ - $\text{CO}_2$  systems for Tm, Yb and Lu. *Mater. Chem. Phys.* **10**, 425–441 (1984).
46. Tareen, J. A. K. & Kutty, T. R. N. Hydrothermal phase equilibria in  $\text{Ln}_2\text{O}_3$ - $\text{H}_2\text{O}$ - $\text{CO}_2$  Systems. *J. Cryst. Growth* **50**, 527–532 (1980).
47. Tareen, J. A. K., Kutty, T. R. N. & Mohamed, I. The Stable Lanthanide Carbonates in the  $\text{Ln}_2\text{O}_3$ - $\text{H}_2\text{O}$ - $\text{CO}_2$  Systems. *Indian Mineral.* **21**, 43–48 (1980).
48. Trombe, F., Blaise, M. & Caro, P. E. Sur la solubilité des carbonate d'yttrium, de scandium et de quelques éléments du groupe des terres rares dans l'eau chargée de gaz carbonique. *Comptes rendus Hebd. des seances l'Academie des Sci. Ser. C* **263**, 521–524 (1966).
49. Caro, P. E. & Lemaitre-Blaise, M. Hydroxycarbonates de terres rares  $\text{Ln}_2(\text{CO}_3)_x(\text{OH})_{2(3-x)} \cdot n\text{H}_2\text{O}$  (Ln = terres rares). *Comptes rendus Hebd. des seances l'Academie des Sci. Ser. C* **269**, 687–690 (1969).
50. Caro, P., Lemaitre-Blaise, M. & Trombe, F. Identification et solubilités des phases solides à l'équilibre sous une atmosphère de gaz carbonique dans les systèmes ternaires oxydes de terres rares-gaz carbon. *Comptes rendus Hebd. des seances l'Academie des Sci. Ser. C* **267**, 1594–1597 (1968).
51. Sprycha, R., Jablonski, J. & Matijević, E. Zeta potential and surface charge of monodispersed colloidal yttrium(III) oxide and basic carbonate. *J. Colloid Interface Sci.* **149**, 561–568 (1992).
52. Zhang, Y., Han, K., Cheng, T. & Fang, Z. Synthesis, characterization, and photoluminescence property of  $\text{LaCO}_3\text{OH}$  microspheres. *Inorg. Chem.* **46**, 4713–4717 (2007).
53. Zhang, Y. et al. Synthesis, characterization and formation mechanism of dumbbell-like  $\text{YOHCO}_3$  and rod-like  $\text{Y}_2(\text{CO}_3)_3 \cdot 2.5\text{H}_2\text{O}$ . *J. Alloys Compd.* **474**, 598–604 (2009).

54. Li, K. & Zhao, P. Synthesis of single-crystalline  $\text{Ce}(\text{CO}_3)(\text{OH})$  with novel dendrite morphology and their thermal conversion to  $\text{CeO}_2$ . *Mater. Res. Bull.* **45**, 243–246 (2010).
55. Salavati-Niasari, M., Hosseinzadeh, G. & Davar, F. Synthesis of lanthanum hydroxide and lanthanum oxide nanoparticles by sonochemical method. *J. Alloys Compd.* **509**, 4098–4103 (2011).
56. Li, Z. *et al.* Synthesis of  $\text{LaCO}_3\text{OH}$  nanowires via a solvothermal process in the mixture of water and room-temperature ionic liquid. *Mater. Lett.* **59**, 963–965 (2005).
57. Qi, R. J., Zhu, Y. J., Cheng, G. F. & Huang, Y. H. Sonochemical synthesis of single-crystalline  $\text{CeOHCO}_3$  rods and their thermal conversion to  $\text{CeO}_2$  rods. *Nanotechnology* **16**, 2502–2506 (2005).
58. Salavati-Niasari, M., Javidi, J. & Davar, F. Sonochemical synthesis of  $\text{Dy}_2(\text{CO}_3)_3$  nanoparticles,  $\text{Dy}(\text{OH})_3$  nanotubes and their conversion to  $\text{Dy}_2\text{O}_3$  nanoparticles. *Ultrason. Sonochem.* **17**, 870–877 (2010).
59. Li, Q., Han, Z., Shao, M., Liu, X. & Qian, Y. Preparation of cerium hydroxycarbonate by a surfactant-assisted route. *J. Phys. Chem. Solids* **64**, 295–297 (2003).
60. Kawahashi, N. & Matijević, E. Preparation and properties of uniform coated colloidal particles. V. Yttrium basic carbonate on polystyrene latex. *J. Colloid Interface Sci.* **138**, 534–542 (1990).
61. Aiken, B. & Matijević, E. Preparation and properties of uniform coated inorganic colloidal particles. IV. Yttrium basic carbonate and yttrium oxide on hematite. *J. Colloid Interface Sci.* **126**, 645–649 (1988).
62. Matijević, E. & Hsu, W. P. Preparation and Properties of Monodispersed of Lanthanide Compounds Colloidal Particles of Lanthanide Compounds. *J. Colloid Interface Sci.* **118**, 506 (1987).
63. Zhu, W., Ma, J., Xing, X., Xu, L. & Chen, Y. Microemulsion-assisted solvothermal synthesis of  $\text{Nd}_2(\text{CO}_3)_3 \cdot 8\text{H}_2\text{O}$  microstructures. *Mater. Res. Bull.* **46**, 830–834 (2011).
64. Yang, X. *et al.*  $\text{LaCO}_3\text{OH}$  microstructures with tunable morphologies: EDTA-assisted hydrothermal synthesis, formation mechanism and adsorption properties. *RSC Adv.* **3**, 3907 (2013).
65. Gao, K. *et al.* Hydrothermal synthesis of single-crystal  $\text{CeCO}_3\text{OH}$  and their thermal conversion to  $\text{CeO}_2$ . *Chinese Chem. Lett.* **25**, 383–386 (2014).
66. Han, Z. H. *et al.* Hydrothermal crystal growth and characterization of cerium hydroxycarbonates. *J. Cryst. Growth* **219**, 315–318 (2000).
67. Zhong, S.-L. *et al.* Gelatin-mediated hydrothermal synthesis of apple-like  $\text{LaCO}_3\text{OH}$  hierarchical nanostructures and tunable white-light emission. *CrystEngComm* **13**, 4151 (2011).
68. Li, G. *et al.*  $\text{Eu}^{3+}/\text{Tb}^{3+}$  - Doped  $\text{La}_2\text{O}_2\text{CO}_2/\text{La}_2\text{O}_3$  Nano/Microcrystals with Multiform Morphologies: Facile Synthesis, Growth Mechanism, and Luminescence Properties. *Inorg. Chem.* **49**, 10522–10535 (2010).
69. Gu, F., Wang, Z., Han, D., Guo, G. & Guo, H. Crystallization of rare earth carbonate nanostructures in the reverse micelle system. *Cryst. Growth Des.* **7**, 1452–1458 (2007).

70. Qian, L. W., Wang, X. & Zheng, H. G. Controlled synthesis of three-fold dendrites of  $\text{Ce}(\text{OH})\text{CO}_3$  with multilayer caltrop and their thermal conversion to  $\text{CeO}_2$ . *Cryst. Growth Des.* **12**, 271–280 (2012).
71. Her, Y.-S., Matijević, E. & Wilcox, W. R. Continuous precipitation of monodispersed yttrium basic carbonate powders: Part III. Kinetics. *J. Mater. Res.* **7**, 2269–2272 (1992).
72. Her, Y. shein, Matijević, E. & Wilcox, W. R. Continuous precipitation of monodispersed yttrium basic carbonate powders. *Powder Technol.* **61**, 173–177 (1990).
73. Matijevic, E. Colloid science of ceramic powders. *Pure Appl. Chem.* **60**, 1479–1491 (1988).
74. Cress, C. D., Redino, C. S., Landi, B. J. & Raffaele, R. P. Alpha-particle-induced luminescence of rare-earth-doped  $\text{Y}_2\text{O}_3$  nanophosphors. *J. Solid State Chem.* **181**, 2041–2045 (2008).
75. Di, W., Ren, X., Zhang, L., Liu, C. & Lu, S. A facile template-free route to fabricate highly luminescent mesoporous gadolinium oxides. *CrystEngComm* **13**, 4831 (2011).
76. Raikow, P. N. The Action of Carbon Dioxide upon the Hydroxides of the Metals. *Chemiker-Zeitung* **31**, 55–57 (1907).
77. Trombe, F. & Caro, P. Process for Separating Rare Earths. **3**, 5 (1970).
78. Fernando, Q., Yanagihara, N., Dyke, J. T. & Vemulapalli, K. Formation of Rare Earth Carbonates using Supercritical Carbon Dioxide. **11** (1991).
79. Michiba, K., Tahara, T., Nakai, I., Miyawaki, R. & Matsubara, S. Crystal structure of hexagonal  $\text{RE}(\text{CO}_3)\text{OH}$ . *Zeitschrift fur Krist.* **226**, 518–530 (2011).
80. Tahara, T., Hokura, A., Nakai, I., Miyawaki, R. & Matsubara, S. Hydrothermal synthesis and crystal structure analysis of  $\text{RE}(\text{CO}_3)\text{OH}$  ( $\text{RE} = \text{La}, \text{Ce}, \text{Nd}, \text{Sm}, \text{Gd}, \text{Dy}, \text{Y}, \text{Er}, \text{Yb}$ ). *Kidorui* **42**, 216–217 (2003).
81. Head, E. L. Preparation of the carbonates of the rare earths from some of their organic acid salts. *Inorg. Nucl. Chem. Lett.* **2**, 33–37 (1966).
82. Salutsky, M. L. & Quill, L. L. The Rare Earth Metals and their Compounds. XII. Carbonates of Lanthanum, Neodymium and Samarium. *J. Am. Chem. Soc.* **72**, 3306–3307 (1950).
83. Charles, R. G. Rare-earth carbonates prepared by homogeneous precipitation. *J. Inorg. Nucl. Chem.* **27**, 1489–1493 (1965).
84. Head, E. L. & Holley Jr, C. E. *The Preparation and Thermal Decomposition of Some Rare Earth Carbonates*. (Los Alamos National Laboratory, 1963).
85. Head, E. L. & Holley, C. E. J. *The Preparation and Thermal Decomposition of the Carbonates of Tb, Dy, Ho, Er, Tm, Yb, Lu, Y, AND Sc*. (Los Alamos National Laboratory, 1963). doi:10.2172/4042280
86. Sastry, R. L. N., Yoganarasimhan, S. R., Mehrotra, P. N. & Rao, C. N. R. Preparation, characterization and thermal decomposition of praseodymium, terbium and neodymium carbonates. *J. Inorg. Nucl. Chem.* **28**, 1165–1177 (1966).



87. Wakita, H. & Kinoshita, S. A synthetic study of the solid solution in the systems  $\text{La}_2(\text{CO}_3)_3 \cdot 8\text{H}_2\text{O}$  -  $\text{Ce}_2(\text{CO}_3)_3 \cdot 8\text{H}_2\text{O}$  and  $\text{La}(\text{OH})\text{CO}_3$  -  $\text{Ce}(\text{OH})\text{CO}_3$ . *Bulletin of the Chemical Society of Japan* **52**, 428–432 (1979).
88. Shinn, D. B. & Eick, H. A. The Crystal Structure of Lanthanum Carbonate Octahydrate. *Inorg. Chem.* **7**, 1340–1345 (1968).
89. Hinode, H., Sharma, R. & Eyring, L. A study of the decomposition of neodymium hydroxy carbonate and neodymium carbonate hydrate. *J. Solid State Chem.* **84**, 102–117 (1990).
90. Sharma, R., Hinode, H. & Eyring, L. A study of the decomposition of praseodymium hydroxy carbonate and praseodymium carbonate hydrate. *J. Solid State Chem.* **92**, 401–419 (1991).
91. Sordelet, D. & Akinc, M. Preparation of spherical, monosized  $\text{Y}_2\text{O}_3$  precursor particles. *J. Colloid Interface Sci.* **122**, 47–59 (1988).
92. Akinc, M. & Sordelet, D. Preparation of Yttrium, Lanthanum, Cerium, and Neodymium Basic Carbonate Particles by Homogeneous Precipitation. *Adv. Ceram. Mater.* **2**, 232–238 (1987).
93. Refat, M. S. A novel method for the synthesis of rare earth carbonates. *Synth. React. Inorg. Met. Chem.* **34**, 1605–1613 (2004).
94. Deng, Hong-Mei; Xu, Yan; Gu, Y.-D. Growth kinetics of ultrafine monodispersed colloidal particles of rare earth compounds. *Huaxue Xuebao* **53**, 867–870 (1995).
95. Kang, Z. C. & Eyring, L. Sintering in colloidal particles of rare earth hydroxycarbonate and its decomposition products. *J. Alloys Compd.* **225**, 190–192 (1995).
96. Mochizuki, A. Synthetic study of crystalline rare earth carbonates. *Numazu Kogyo Koto Senmon Gakko Kenkyu Hokoku* **9**, 57–62 (1974).
97. Nagashima, K., Wakita, H. & Mochizuki, A. The synthesis of crystalline rare earth carbonates. *Bull. Chem. Soc. Jpn.* **46**, 152–156 (1973).
98. Shibata, J., Noda, S. & Mashimo, M. Crystallization of Rare Earths from Organic Phase by Urea Decomposition. *Shigen-to-Sozai* **110**, 185–189 (1994).
99. Shivaramaiah, R., Anderko, A., Riman, R. E. & Navrotsky, A. Thermodynamics of bastnaesite: A major rare earth ore mineral. *Am. Mineral.* **101**, 1129–1134 (2016).
100. Sklyarenko, Yu. S.; Ruzaikina, L. V. Formation of neodymium, europium, and ytterbium carbonates and their behavior in aqueous potassium carbonate solutions. *Zhurnal Neorg. Khimii* **15**, 778–784 (1970).
101. Goff, G. S. *et al.* Synthesis and structural characterization of molecular Dy(III) and Er(III) Tetra-carbonates. *Inorg. Chem.* **49**, 6558–6564 (2010).
102. Philippini, V., Vercoeur, T., Chaussé, A. & Vitorge, P. Precipitation of  $\text{Aln}(\text{CO}_3)_2 \cdot x\text{H}_2\text{O}$  and  $\text{Dy}_2(\text{CO}_3)_3 \cdot x\text{H}_2\text{O}$  compounds from aqueous solutions for  $\text{A}^+ = \text{Li}^+, \text{Na}^+, \text{K}^+, \text{Cs}^+, \text{NH}_4^+$ . *J. Solid State Chem.* **181**, 2143–2154 (2008).

103. Vercouter, T., Vitorge, P., Trigoulet, N., Giffcaut, E. & Moulin, C.  $\text{Eu}(\text{CO}_3)_3^{3+}$  and the limiting carbonate complexes of other  $\text{M}^{3+}$  f-elements in aqueous solutions: a solubility and TRLFS study. *New Jou* **29**, 544–553 (2005).
104. Ben Ali, A. *et al.* Cation and anion disorder in new cubic rare earth carbonates  $\text{Na}_2\text{LiLn}(\text{CO}_3)_3$  (Ln=Eu-Er, Yb, Lu, Y); Synthesis, crystal structures, IR, Raman and NMR characterizations. *Solid State Sci.* **6**, 1237–1243 (2004).
105. de Vasconcellos, M. E., da Rocha, S. M. R., Pedreira, W. R., Queiroz, C. A. d S. & Abrão, A. Solubility behavior of rare earths with ammonium carbonate and ammonium carbonate plus ammonium hydroxide: Precipitation of their peroxycarbonates. *J. Alloys Compd.* **451**, 426–428 (2008).
106. Wickleder, M. S. Inorganic lanthanide compounds with complex anions. *Chem. Rev.* **102**, 2011–2087 (2002).
107. Christensen, A. N. Hydrothermal preparation of rare earth hydroxy-carbonates. The crystal structure of  $\text{NdOHCO}_3$ . *Acta Chemica Scandinavica* **27**, 2973–2982 (1973).
108. Kutlu, I. & Meyer, G. Basic Carbonates of Dysprosium:  $\text{Dy}_2\text{O}_2(\text{CO}_3)$  and  $\text{Dy}(\text{OH})(\text{CO}_3)$ . **2**, 402–406 (1999).
109. Doert, T., Rademacher, O. & Getzschmann, J. Crystal structure of dysprosium hydroxide carbonate,  $\text{DyOHCO}_3$ . *Zeitschrift fur Krist. - New Cryst. Struct.* **214**, 11–12 (1999).
110. Beall, G., Milligan, W. & Mroczkowski, S. Yttrium carbonate hydroxide. *Acta Crystallogr. Sect. B.* **8**, 3143–3144 (1976).
111. Sungur, A. & Kizilyalli, M. Synthesis and Structure of  $\text{Gd}_2(\text{CO}_3)_3 \cdot n\text{H}_2\text{O}$  ( $n = 2, 3$ ). *J. Less-Common Met.* **93**, 419–423 (1983).
112. Miyawaki, R., Kuriyama, J. & Nakai, I. The redefinition of tenerite-(Y),  $\text{Y}_2(\text{CO}_3)_3 \cdot 2\text{-}3\text{H}_2\text{O}$ , and its crystal structure. *Am. Mineral.* **78**, 425–432 (1993).
113. Liu, S. & Ma, R. Synthesis of lutetium carbonate. *Acta Chemica Scandinavica* **51**, 893–895 (1997).
114. Liu, S. & Ma, R. Synthesis of a Crystalline Hydrated Basic Ytterbium Carbonate,  $\text{Yb}_2\text{O}_3 \cdot 2.17\text{CO}_2 \cdot 6.17\text{H}_2\text{O}$ . *Synth. React. Inorg. Met. Chem.* **27**, 1183–1190 (1997).
115. Liu, S., Ma, R., Jiang, R. & Luo, F. Synthesis and Structure of Hydrated Yttrium Carbonate,  $\text{Y}_2(\text{CO}_3)_3 \cdot 2.79\text{H}_2\text{O}$ . *Synth. React. Inorg. Met. Chem.* **30**, 271–279 (2000).
116. Liu, S. & Ma, R. Synthesis and characterization of hydrated holmium and erbium carbonates. *Asian J. Chem.* **19**, 1883–1887 (2007).
117. Liu, S., Ma, R., Jiang, R. & Luo, F. Synthesis and structure of hydrated neodymium carbonate. *J. Cryst. Growth* **203**, 454–457 (1999).
118. Song, L. & Rongjun, M. Synthesis and structure of hydrated terbium carbonate. *Indian J. Chem. - Sect. A Inorganic, Phys. Theor. Anal. Chem.* **35**, 992–994 (1996).
119. Song, L. & Rongjun, M. Synthesis and structure of hydrated europium carbonate. *J. Cryst. Growth* **169**, 190–192 (1996).

120. Caro, P. E., Sawyer, J. O. & Eyring, L. The infrared spectra of rare earth carbonates. *Spectrochim. Acta Part A Mol. Spectrosc.* **28**, 1167–1173 (1972).
121. Head, E. L. The preparation of scandium carbonate. *J. Inorg. Nucl. Chem.* **33**, 1201–1203 (1971).
122. Crookes, W. II. On Scandium. *Philos. Trans. R. Soc. London. Ser. A, Contain. Pap. a Math. or Phys. Character* 15–48 (1908).
123. Wakita, H. & Nagashima, K. Synthesis of Tengerite Type Rare Earth Carbonates. *Bulletin of the Chemical Society of Japan* **45**, 2476–2479 (1972).
124. Tahara, T., Nakai, I., Miyawaki, R. & Matsubara, S. Crystal chemistry of  $\text{RE}(\text{CO}_3)\text{OH}$ . *Zeitschrift für Krist.* **222**, 326–334 (2007).
125. Dal Negro, A., Rossi, G. & Tazzoli, V. The Crystal Structure of Ancylite,  $(\text{RE})_x(\text{Ca},\text{Sr})_{2-x}(\text{CO}_3)_2(\text{OH})_x(2-x)\text{H}_2\text{O}$ . *Am. Mineral.* **60**, 280–284 (2015).
126. Dexpert, H. & Caro, P. Determination de la structure cristalline de la variété a des hydroxycarbonates de terres rares  $\text{LnOHCO}_3$  ( $\text{Ln} = \text{Na}$ ). *Mater. Res. Bull.* **9**, 1577–1585 (1974).
127. Rorif, F., Fuger, J. & Desreux, J. F. Thermochemistry of selected trivalent lanthanide and americium compounds: Orthorhombic and hexagonal hydroxycarbonates. *Radiochim. Acta* **93**, 103–110 (2005).
128. Batkibekova, M.; Usubaliev, D. Thermal chemistry of rare earth carbonates. *Zhurnal Fiz. Khimii* **48**, 1615 (1974).
129. Karapet'yants, M. K., Maier, A. I. & Bas'kova, N. Gibbs Standard Energies of Formation of Rare Earth Element Yttrium Carbonates and their Entropies. *Neorg. Mater.* **13**, 1055–1058 (1977).
130. Gamsjäger, H., Marhold, H., Königsberger, E., Tsai, Y. J. & Kolmer, H. Solid-Solute Phase Equilibria in Aqueous Solutions IX. Thermodynamic Analysis of Solubility Measurements:  $\text{La}(\text{OH})_m(\text{CO}_3)_q \cdot r\text{H}_2\text{O}$ . *Zeitschrift für Naturforsch. A.* **50**, 59–64 (1995).
131. Nguyen, A. M., Königsberger, E., Marhold, H. & Gamsjäger, H. Solid-Solute Phase Equilibria in Aqueous Solutions, VIII: The Standard Gibbs Energy of  $\text{La}_2(\text{CO}_3)_3 \cdot 8\text{H}_2\text{O}$ . *Monatshefte fuer Chemie* **124**, 1011–1018 (1993).
132. Karapet'yants, M. K., Maier, A. I. & Bas'kova, N. Standard heats of formation of rare earth element and yttrium carbonates. *Neorg. Mater.* **13**, 1279–1281 (1977).
133. Wilfong, R. L., Domingues, L. P. & Furlong, L. R. Thermogravimetric Analysis of Five Salts of Praseodymium, Neodymium, and Samarium. *J. Am. Ceram. Soc.* **47**, 240–241 (1964).
134. Domingues, L. P., Wilfong, R. L. & Furlong, L. R. Pyrolysis of Five Salts of Yttrium, Lanthanum, and Cerium. *Bur. Mines Rep. Investig.* (1962).
135. Patil, K. C., Chandrashekhara, G. V., George, M. V. & Rao, C. N. R. Infrared spectra and thermal decompositions of metal acetates and dicarboxylates. *Can. J. Chem.* **46**, 257–265 (1968).
136. Watanabe, Y., Miyazaki, S., Maruyama, T. & Saito, Y. Dissociation pressure of lanthanum dioxide carbonate. *J. Mater. Sci. Lett.* **5**, 135–136 (1986).

137. Olafsen, A. & Fjellvag, H. Synthesis of rare earth oxide carbonates and thermal stability of  $\text{Nd}_2\text{O}_2\text{CO}_3$  II. *J. Mater. Chem.* **9**, 2697–2702 (1999).
138. Wendlandt, Wesley W.; George, T. D. The thermal decomposition of inorganic compounds. IV. Rare earth carbonates. *Texas J. Sci.* **13**, 316–328 (1961).
139. Foger, K., Hoang, M. & Turney, T. W. Formation and thermal decomposition of rare-earth carbonates. *J. Mater. Sci.* **27**, 77–82 (1992).
140. D'Assunção, L. M., Ionashiro, M., Rasera, D. E. & Giolito, I. Thermal decomposition of the hydrated basic carbonates of lanthanides and yttrium in  $\text{CO}_2$  atmosphere. *Thermochim. Acta* **219**, 225–233 (1993).
141. Jordanov, N. & Havezov, I. Löslichkeitsprodukte der normalen Carbonate einiger dreiwertiger Seltener Erden ( $\text{Er}_2(\text{CO}_3)_3 \cdot n\text{H}_2\text{O}$ ). *Zeitschrift für Anorg. und allgemeine Chemie* **347**, 101–106 (1966).
142. Spahiu, K. & Bruno, J. *A selected thermodynamic database for REE to be used in HLNW performance assessment exercises.* (1995).

### **Chapter 3. PRECIPITATION OF RARE EARTH CARBONATES USING MONOETHANOLAMINE**

#### **3.1 Introduction**

The rare earth elements comprise an important aspect of modern society. Cellphones, internet, renewable energy, optics, lasers, energy storage, metallic alloys, and high temperature applications to name a few, all made possible by the unique properties of the rare earth elements<sup>1,2</sup>. Actually, to say the rare earth elements are an important aspect of modern life is an understatement. They are essential. Despite their importance, they are not well known to the greater public as they fall rather low on the total production chain, but their impact on modern technology and current standards of living is undeniable. The rare earths have and will continue to be of significant importance to future technological and global development<sup>3</sup>.

Given their importance, one could reasonably ask whether or not global rare earth reserves will be sufficient to meet demand for the foreseeable future. Global surveys have determined that the planet has more than sufficient amounts of rare earth to meet current and expected increases in demand for the rare earth for multiple centuries. So the real questions are where and how they will be produced. Rare earth production from mineral resources is a complex, chemically intensive process requiring significant capital and intellectual investment. In efforts to modernize and maintain control over a strategic resource, China has invested significantly in rare earth production since the mid 1980's<sup>4,5</sup>. This aggressive expansion has allowed China to singularly dominate global rare earth production beginning in the late 1990's. In 2009, China accounted for  $\geq 95\%$  of global production of rare earth oxides (REO)<sup>6</sup>. However, to essentially be the world's only producer of REOs, China and its environment have paid dearly.

Chinese producers can often produce REOs without having to address the environmental concerns associated with rare earth refinement. This is not for the lack of policies in China

regarding waste management, but rather the inability or unwillingness to enforce these policies on all Chinese rare earth producers. The refinement process uses significant quantities of acids and bases, which often results in acidified wastewater, concentrated radioactive waste, acid rain, ammonia laden water, and others. The Bayan Obo mine, the world's largest rare earth mine, has been estimated to create 8.5 kg of fluorine, 13 kg of dust, 9600 – 12000 m<sup>3</sup> of waste gas that contains hydrofluoric acid, sulfur dioxide, and sulfuric acid, 75 m<sup>3</sup> of acidic wastewater, 1 ton of radioactive residue (usually thorium), and 2000 tons of potentially radioactive tailings per 1 ton of REO produced<sup>5</sup>. These figures do not include an estimated >25000 tons/year of ammonia laden wastewater generated by the refinement process<sup>7</sup>. Most of this is stored within the immediate vicinity of Bayan Obo and has created a >10 km<sup>2</sup> radioactive, acidic lake that has been linked to underground water pollution, deforestation, and numerous human health issues<sup>8</sup>. Combined with black market mining/refinement operations where any semblance of pollution control is nonexistent, the damage to China's environment demonstrates the unsustainable nature of rare earth refinement using existing methodologies.

United States REO production often requires strict management of waste streams according to even more strictly enforced environmental protection mandates<sup>9</sup>. Abiding by these mandates while using the same unsustainable technologies as Chinese REO producers proved too costly as waste management hindered the ability of US producers to compete. For US producers to be environmentally sustainable and competitive, research into the REO production process, including ways to manage waste, is necessary. Waste management can be achieved by addressing the chemical treatment processes associated with rare earth refinement and their significant consumption of acids and bases<sup>2,10–18</sup>. The stripping process, where a rare earth loaded solvent extractant is stripped of its rare earth content by another solution, consumes a significant quantity of acid and base. The stripping solution is an aqueous mineral acid solution that pulls the rare

earths out of the solvent extractant while regenerating said extractant for continued use. This creates an acidic rare earth salt solution that is then neutralized and depleted of its rare earth content using base and precipitants, such as ammonium bicarbonate or sodium carbonate<sup>19–32</sup>. The large volumes of base/precipitant required to create the precipitate, often a rare earth carbonate, is environmentally unsustainable as the remaining aqueous solution poses a significant downstream waste management issue<sup>5,8,9</sup>. Decreasing the amount of base/precipitant used would improve the sustainability of the process.

Monoethanolamine, or 2-aminoethanol or ethanolamine, is a weak base that has been extensively used as part of a host of technologies under the carbon capture and storage (CCS) umbrella<sup>33–35</sup>. As one of the more mature chemical absorption technologies, the carbon capture ability of monoethanolamine (MEA) is well understood<sup>36–38</sup>. On a per mole of basis, 1.0 mole of MEA is able to absorb 0.5 mole of CO<sub>2</sub> (~30 wt%). The specific mechanism by which MEA absorbs CO<sub>2</sub> and creates the carbamate salt is still not fully understood<sup>39</sup>, but the most important aspect is that this absorption process is reversible. In MEA based CCS systems, CO<sub>2</sub> is released from MEA by heating the amine solution between 100 – 120 °C<sup>33</sup>. This CO<sub>2</sub> is pressurized and then sequestered to decrease anthropogenic greenhouse gas emissions. Others, have utilized solutions of MEA loaded with CO<sub>2</sub> as a source of carbon dioxide for means of chemical reactions. A body of literature that exists for this particular application of MEA is devoted to the study of a calcium solid to calcium carbonate. Li, Gupta, and Riman demonstrated the conversion of calcium silicate to calcium carbonate<sup>40</sup>. Park and Park demonstrated the conversion of a calcium hydroxide slurry to calcium carbonate<sup>41</sup>. A separate body of literature has focused on the precipitation of calcium carbonate from aqueous solution of a calcium salt. Vučak precipitated different polymorphs of calcium carbonate depending upon specific conditions from solutions of calcium nitrate<sup>42,43</sup>. Park and Park precipitated multiple polymorphs of calcium carbonate from solutions of calcium

chloride<sup>44</sup>. Herein, we will also utilize CO<sub>2</sub> loaded MEA to precipitate a carbonate product from an aqueous solution of its respective water soluble salt. This work will demonstrate the precipitation of rare earth carbonates from aqueous solutions of their respective rare earth chlorides using MEA. The chemical products in the resulting neutralization/precipitation reaction can be easily isolated from one another for further processing or reuse.

### 3.2 Materials and Methods

#### 3.2.1. Thermodynamic Process Simulation

Stability and equilibrium diagrams (Figure 3.1) for the reaction of aqueous solutions of rare earth chlorides with aqueous solutions of MEA-CO<sub>2</sub> were calculated using OLI thermochemical simulation software (OLI Systems, Inc., Morris Plains, NJ, USA). Parameters input for the calculation of neodymium carbonate precipitation (Nd<sub>2</sub>(CO<sub>3</sub>)<sub>3</sub> and Nd(OH)CO<sub>3</sub>) were based on inflows of neodymium chloride (NdCl<sub>3</sub>) and MEA at the desired conditions; temperature = 25 °C, pCO<sub>2</sub> = 1 atm, and yield 0.99. NdCl<sub>3</sub> concentration input ranged from 10<sup>-8.0</sup> to 10<sup>0</sup> molal. MEA concentration input ranged from 0 to 3.0 molal. The precipitation conditions for NdCl<sub>3</sub> concentration vs. MEA concentration that fall within the 99% depletion space (marked green) helped determine exact concentrations of each inflow used in the precipitation experiments.

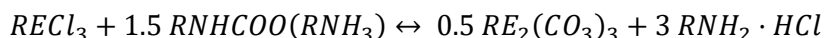
#### 3.2.2. Rare Earth Carbonate Precipitation

The normal carbonates of lanthanum (La<sub>2</sub>(CO<sub>3</sub>)<sub>3</sub> · 8H<sub>2</sub>O), neodymium (Nd<sub>2</sub>(CO<sub>3</sub>)<sub>3</sub> · 8H<sub>2</sub>O), and yttrium (Y<sub>2</sub>(CO<sub>3</sub>)<sub>3</sub> · 3H<sub>2</sub>O) were precipitated from aqueous solutions of their respective chloride salts mixed with a separate aqueous solution of monoethanolamine (MEA) loaded with CO<sub>2</sub>. All chemicals were used without further purification. ACS reagent grade lanthanum (III) chloride heptahydrate (LaCl<sub>3</sub> · 7H<sub>2</sub>O) and ACS reagent grade monoethanolamine (ethanolamine, 2-Aminoethanol) were purchased from Millipore Sigma (Saints Louis, Missouri, USA). 99.9% (REO)



neodymium (III) chloride hydrate ( $\text{NdCl}_3 \cdot x\text{H}_2\text{O}$ ) was purchased from Fisher Scientific (Pittsburgh, Pennsylvania, USA). Industrial grade carbon dioxide ( $\text{CO}_2$ ) was purchased from Airgas (Radnor, Pennsylvania, USA). 18.2 M $\Omega$  electrical resistivity water as dispensed from a Milli-Q® Direct 8 Water Purification System from Millipore Sigma (Billerica, Massachusetts, USA) was used as the solvent for all solutions. Precipitates were collected via vacuum filtration through Grade 151 – Ahlstrom™ glass microfiber filters (VWR International, Radnor, Pennsylvania, USA) placed in 70 mm porcelain Buchner funnels (Fisher Scientific, Pittsburgh, Pennsylvania, USA) attached via Pluro stoppers (VWR International, Radnor, Pennsylvania, USA) to heavy wall filter flasks.

The process simulation (Figure 3.1) dictated the specific concentrations of the inflow solutions of rare earth chloride(s) and MEA with which we could achieve  $\geq 99\%$  depletion of the rare earth chloride solutions. In Table 3.1, the concentrations of the rare earth chlorides solutions ( $m = 10^{-2} - 10^{-4}$ ) with the concentrations of the respective MEA solutions ( $m = 0.25 - 2.5$ ) for a number of precipitation experiments are outlined. With the inflow solution concentrations established, the following chemical equation was used to determine the exact amounts of each inflow solution to precipitate the desired amount of precipitate:



$\text{RNHCOO}(\text{RNH}_3)$  and  $\text{RNH}_2 \cdot \text{HCl}$  are the carbamate and hydrogen chloride salts formed by MEA when loaded with  $\text{CO}_2$  and  $\text{HCl}$ , respectively. The loading capacity of MEA is known to be 0.5 mol of  $\text{CO}_2$  per 1.0 mol MEA, which roughly translates to 30 g of  $\text{CO}_2$  per 100 g of MEA (~30 wt%).  $\text{CO}_2$  loaded MEA solutions are created by bubbling  $\text{CO}_2$  into the MEA solution. The mass gain of the solution due to  $\text{CO}_2$  absorption plateaus after approximately 9 minutes. Subsequent mentions of MEA solutions are implied to contain the theoretical maximum amount of  $\text{CO}_2$  unless explicitly specified.

All precipitation experiments were conducted at room temperature (25 °C) and ambient pressure (1 atm). The exact amounts of the inflow solutions were calculated so that MEA solutions provided the stoichiometric amounts of CO<sub>2</sub> necessary to precipitate the normal carbonate. The rare earth chloride solution was poured into the MEA solution while stirring; a precipitate is immediately observed. The mixture was then stirred for 5 additional minutes before being collected via vacuum filtration. Aged samples were stirred under CO<sub>2</sub>-bubbling at 25 °C for 5 to 7 days before collection. The filtrate was retained for ICP-OES analysis. The precipitates were then air dried (25 °C) and ground using a 3-inch agate mortar and pestle. The precipitates were not modified prior to characterization.

### *3.2.3. Characterization*

The structure and phase of the rare earth carbonate powders were characterized using powder X-ray diffraction (XRD) on a Bruker D8 Discover (Bruker AXS, Inc, Madison, Wisconsin, USA) with a step size of 0.018° (2θ) with a 0.5 s dwell time. The instrument was equipped with a Vantec 1 Detector, copper K-alpha source operating at 40 kV and 40 mA (1600 Watts), and a horizontal goniometer. Pattern-fitting and Rietveld-analysis were conducted using MDI Jade 9 (Materials Data, Inc., Livermore, California, USA) equipped with Fachinformationszentrum Karlsruhe/National Institute of Standards and Technology Inorganic Crystal Structure Database (FIZ/NIST ICSD, National Institute of Standards and Technology, Gaithersburg, Maryland, USA).

The chemical identities of all rare earth carbonates were determined using Fourier-transform infrared spectroscopy (FTIR) on a Nicolet 6700 FT-IR Spectrometer in transmission mode (Thermo Fisher Scientific, Waltham, Massachusetts, USA). 10 mg of samples were mixed with 200 mg of FTIR grade potassium bromide (KBr) purchased from Millipore Sigma (Saint Louis, Missouri, USA)

and then pressed into 10 mm pellets. FTIR spectra were collected via the average of 32 scans at a resolution of  $1\text{ cm}^{-1}$  over a range of  $4000\text{ cm}^{-1}$  to  $650\text{ cm}^{-1}$ .

The thermal decomposition profiles of all rare earth carbonate powders were collected via thermogravimetric analysis (TGA) on a Q5000IR from TA Instruments (New Castle, Delaware, USA) in a nitrogen ( $\text{N}_2$ ) atmosphere, with a flow rate of  $50\text{ mL/min}$ , at a heating rate of  $0.25\text{ }^\circ\text{C/min}$  to  $900\text{ }^\circ\text{C}$ . Samples were loaded onto high temperature, ceramic tipped platinum pans. Decomposition profiles were analyzed using TA Universal Analysis (TA Instruments, New Castle, Delaware, USA).

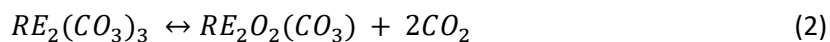
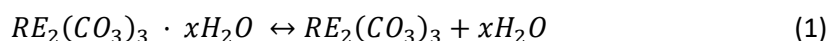
Aqueous concentrations of rare earth ions were determined using inductively coupled plasma optical emission spectroscopy (ICP-OES) on a Perkin Elmer Optima 7300 DV (Waltham, Massachusetts, USA). Concentrations for aqueous lanthanum were collected from the La 379.478 nm and La 384.902 nm peaks. Concentrations for aqueous neodymium were collected from the Nd 401.225 nm and Nd 430.358 nm peaks. Concentrations for aqueous yttrium were collected from the Y 360.073 nm and Y 324.227 nm peaks. Calibration curves up to 1000 ppm using ICP standards at 1000 ppm, 100 ppm, and 1 ppm purchased from SCP Science (Champlain, New York, USA). Theoretical sample concentrations in parts per million (ppm) were calculated from their desired concentrations in molal. Samples were diluted prior to analysis so that the theoretical concentrations would fall within the concentration calibration range ( $< 1000\text{ ppm}$ ).

### **3.3. Results and Discussion**

XRD analysis of the unaged precipitates reveal that they are amorphous (Figure 3.2) with only the lanthanum carbonate precipitates exhibiting any amount of crystallinity, which corresponded to the lanthanite-(La) (PDF#: 97-002-224) phase. On the other hand, XRD analysis of the aged precipitates indicate the formation of the normal carbonates for their respective rare earth

elements (Figure 3.2): lanthanite-(La) (PDF: 97-002-224), lanthanite-(Nd) (PDF: 99-000-2054), and tengerite-(Y) (PDF: 97-007-2940). It should be stated that additional precipitate samples were aged to allow for their chemical identification via XRD.

To help confirm the chemical identity of the unaged precipitates, additional FTIR analysis (Figure 3.3) and TGA (Figure 3.4) were conducted. FTIR analysis of all precipitates indicate the formation of the normal carbonates. All carbonate samples exhibit the absorption bands characteristic for the rare earth element's respective normal carbonate<sup>45</sup> (Figure 3.3 & Table 3.2), while all filtrates show the peaks characteristic for monoethanolamine-hydrogen chloride (MEA-HCl). TGA (Figure 3.4) results are also indicative of the formation of the normal carbonates. The normal carbonates are known to undergo the following general pathway during thermal decomposition<sup>46–54</sup>:



The mass loss due to dehydration is not an insignificant quantity.  $La_2(CO_3)_3 \cdot 8H_2O$  and  $Nd_2(CO_3)_3 \cdot 8H_2O$  lose greater than 20% of their initial masses and  $Y_2(CO_3)_3 \cdot 2H_2O$  loses greater than 10% of its initial mass in the formation of their respective anhydrous carbonate. The final formation of all rare earth oxides results in greater than 40% mass loss. In the decomposition profiles, the presence of three distinct plateaus are indicative of the formation of the three decomposition products associated with the normal carbonates: the anhydrous normal carbonate, the oxycarbonate, and the oxide. It should be noted that the respective hydroxycarbonates are known to follow a thermal decomposition pathway similar to that of the normal carbonates<sup>46,47,55,56</sup>, but a significant mass loss associated with dehydration is noticeably absent.

Though the chemical identity of the observed precipitate has been established, this precipitation methodology would be relatively inefficient if it is unable to utilize the full content of the rare earth chloride solution from which the precipitates are created. That is, the precipitation methodology should be able to deplete the majority of, if not all, of the rare earths from the input rare earth chloride solution. ICP-OES shows that utilizing precipitation parameters within the 99% depletion space as determined by the process simulation (Figure 3.1) results in greater than 99% depletion of the starting rare earth chloride solution (Table 3.3). Utilizing precipitation parameters outside the predicted 99% depletion space results in sub-optimal yields. Attempts to precipitate carbonate samples from 1 molal neodymium chloride ( $\text{NdCl}_3$ ) solutions ( $10^0$  m) using stoichiometric amounts of 1 molal MEA solution resulted in an incomplete depletion of the  $\text{NdCl}_3$  solution. Though a neodymium precipitate, which itself had the characteristic purple color when viewed under sunlight, was observed, the filtrate still retained the purple color characteristic of aqueous  $\text{NdCl}_3$  solutions when also viewed under sunlight. This is indicative of an incomplete, very much less than 99% depletion of the  $\text{NdCl}_3$  solution.

Additional carbonate precipitation experiments conducted with relatively extreme conditions within the 99% depletion space, such as a very large stoichiometric excess of MEA, do not yield significant improvements in precipitate quality or ease of processing. Process simulations (Figure 3.1) show that dilute solutions of rare earth chlorides ( $10^{-5.0} - 10^{-2.0}$ ) can be depleted with relatively dilute solutions of MEA. Using concentrated solutions of MEA does not make it easier to deplete dilute rare earth chloride solutions. On the other hand, when working with more concentrated rare earth chloride solutions ( $10^{-1.0} - 10^{-0.4}$ ), the use of more concentrated MEA solutions (1.0 – 2.0 m) is an absolute requirement to achieve greater than 99% depletion. It should also be noted that even within the predicted 99% yield space, using MEA solutions at concentrations of 2.5 molal and greater result in the preferred/competing formation of the rare

earth hydroxide, making the separation of the precipitate from the aqueous phase extraordinarily difficult. Finally, attempting to deplete a rare earth chloride solution using insufficiently loaded MEA (not at maximum CO<sub>2</sub> loading capacity) or pure MEA of any quantity results in the formation of the rare earth hydroxide, which again makes separation of the precipitate from the aqueous phase extremely difficult.

As aforementioned, the conditions at which precipitation experiments were conducted were informed by the thermodynamic process simulations (Figure 3.1). Within the predicted 99% depletion spaces, all findings have validated the greater than 99% depletion of the rare earth chloride solution. Yet the observed inconsistencies in the predicted chemical identity of the precipitate, alongside the lack of process simulations for the lanthanum and yttrium systems, serves to highlight an incomplete understanding of the normal carbonates, the hydroxycarbonates, and the exact relationship between the two phases. The lack of process simulations for the lanthanum and yttrium systems can be attributed to the incomplete development of the software specific database used to generate the phase diagrams and may be addressed by ongoing development. Given the fact that the rare earth elements are chemically similar to one another, the same or similar precipitation conditions used to generate the neodymium carbonates in this study could be used to generate the lanthanum and yttrium carbonates, which they were. Of more concern is the difference between the observed and predicted precipitate.

Figure 3.1 presents the equilibrium phase diagrams for both Nd(OH)CO<sub>3</sub> and Nd<sub>2</sub>(CO<sub>3</sub>)<sub>3</sub>. It should be noted at the same MEA, CO<sub>2</sub>, temperature, and NdCl<sub>3</sub> conditions, both phases have been predicted as possible, but only the normal carbonate is experimentally observed. Depending upon perspective, this difference could be meaningful or meaningless. From an industrial processing perspective, the difference between the normal carbonate and hydroxycarbonate is meaningless

as both are equally useful in the downstream production of other rare earth solids. From a purely predictive and scientific basis, this difference should be indicative of the inconsistent understanding of the relationship between the normal carbonates and hydroxycarbonates. What is known from literature is that the hydroxycarbonates are the preferred carbonate phase at higher temperatures in the  $\text{RE}_2\text{O}_3 - \text{CO}_2 - \text{H}_2\text{O}$  ternary systems<sup>57–61</sup>. At standard temperatures and pressures (25 °C, 1 atm), the normal carbonates are the preferred carbonate phase. According to available literature on the thermochemical values for the rare earth carbonates, the normal carbonates are at least 2500 kJ/mol more stable than their hydroxycarbonate counterparts<sup>54</sup>. However, when considering the rare earths in geological settings, where there is a preponderance of  $\text{CO}_2$  and  $\text{H}_2\text{O}$ , the hydroxycarbonates seem to predominate and have been of research interest<sup>62–65</sup>. So, at standard temperature and pressure, it can be logically assumed that the hydroxycarbonates would be the preferred phase. Yet, what is often overlooked is that the hydroxycarbonates form as a result of the hydrolysis of the normal carbonates. This hydrolysis has been shown to occur to all of the normal carbonates, the degree and rate of which increases with increasing atomic number. Sufficient  $p\text{CO}_2$  ( $\geq 1$  atm) prevents this hydrolysis outright while normal carbonates in water at atmospheric  $p\text{CO}_2$  ( $p\text{CO}_2 = 3 \times 10^{-4}$  atm) will undergo hydrolysis<sup>66</sup>.

The difference between the observed and predicted precipitate should not be the basis for disregarding the thermodynamic process simulation. If anything, this difference highlights the fact that current understanding on the rare earth carbonates does not necessarily grasp their full nuanced nature. Improving modeling parameters to account for such differences can be implemented in subsequent releases and simulations. The value of the process simulations has been established by the predicted and observed  $\geq 99\%$  depletion of rare earth chloride solutions at varying concentrations. Further refinement and expansion of the simulation capabilities will

help mature both the MEA-based precipitation methodology and the theoretical understanding of behavior of rare earths.

### 3.4. Conclusion

Thermodynamic process simulations of the  $\text{NdCl}_3 - \text{MEA} - \text{H}_2\text{O}$  system at  $p\text{CO}_2 = 1 \text{ atm}$  have identified conditions at which inflow solutions of  $\text{NdCl}_3$ , up to  $10^{-0.4} \text{ m}$  or  $100 \text{ g/L}$  in concentration, can be depleted with  $\geq 99\%$  efficiency using MEA loaded with  $\text{CO}_2$ . Analysis of precipitates and filtrates created using the predicted conditions verified the  $\geq 99\%$  depletion of the inflow  $\text{NdCl}_3$  solution, formation of MEA-HCl in the filtrate, and the formation of  $\text{Nd}_2(\text{CO}_3)_3 \cdot 8\text{H}_2\text{O}$ . Due to the chemical similarity of the rare earth elements, application of precipitation conditions similar to those used for the neodymium system to lanthanum and yttrium resulted in  $>99\%$  depletion of their respective rare earth chloride solutions, formation of the MEA-HCl in the filtrate, and the formation of their respective normal carbonate:  $\text{La}_2(\text{CO}_3)_3 \cdot 8\text{H}_2\text{O}$  and  $\text{Y}_2(\text{CO}_3)_3 \cdot 2\text{H}_2\text{O}$ . The facile separation of MEA-HCl from the precipitates allows for further processing and use. However, we have also demonstrated that further development of the process simulation(s) and the supporting database are necessary to better account for the nuances associated with the rare earth carbonates. The difference in the predicted and observed precipitate underlies a greater lack of understanding in the relationship between the normal carbonate, hydroxycarbonate, and the factors that determine which of these are actually observed. Despite the differences, the value of the process simulation has been established.



## 3.5. Figures

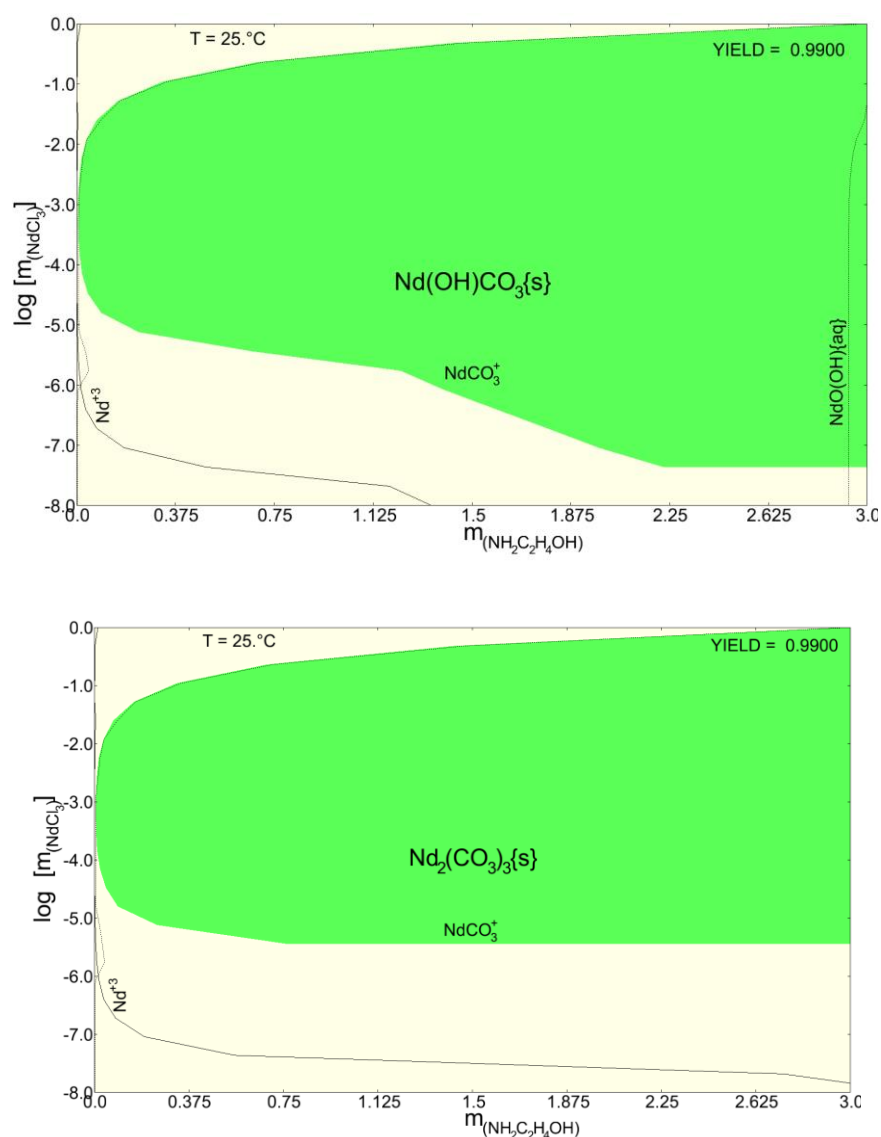


**Figure 3.10.** Thermodynamic simulation from OLI software. Equilibrium phase diagram as a function of MEA concentration (molality) with respect to  $\text{NdCl}_3$  concentration (molality) at a fixed  $p\text{CO}_2 = 1 \text{ atm}$  and  $T = 25^\circ\text{C}$ . Phase stability diagrams for  $\text{Nd(OH)CO}_3$  and  $\text{Nd}_2(\text{CO}_3)_3$  are presented. Green areas represent conditions at which the solids may be recovered at 99% yield.

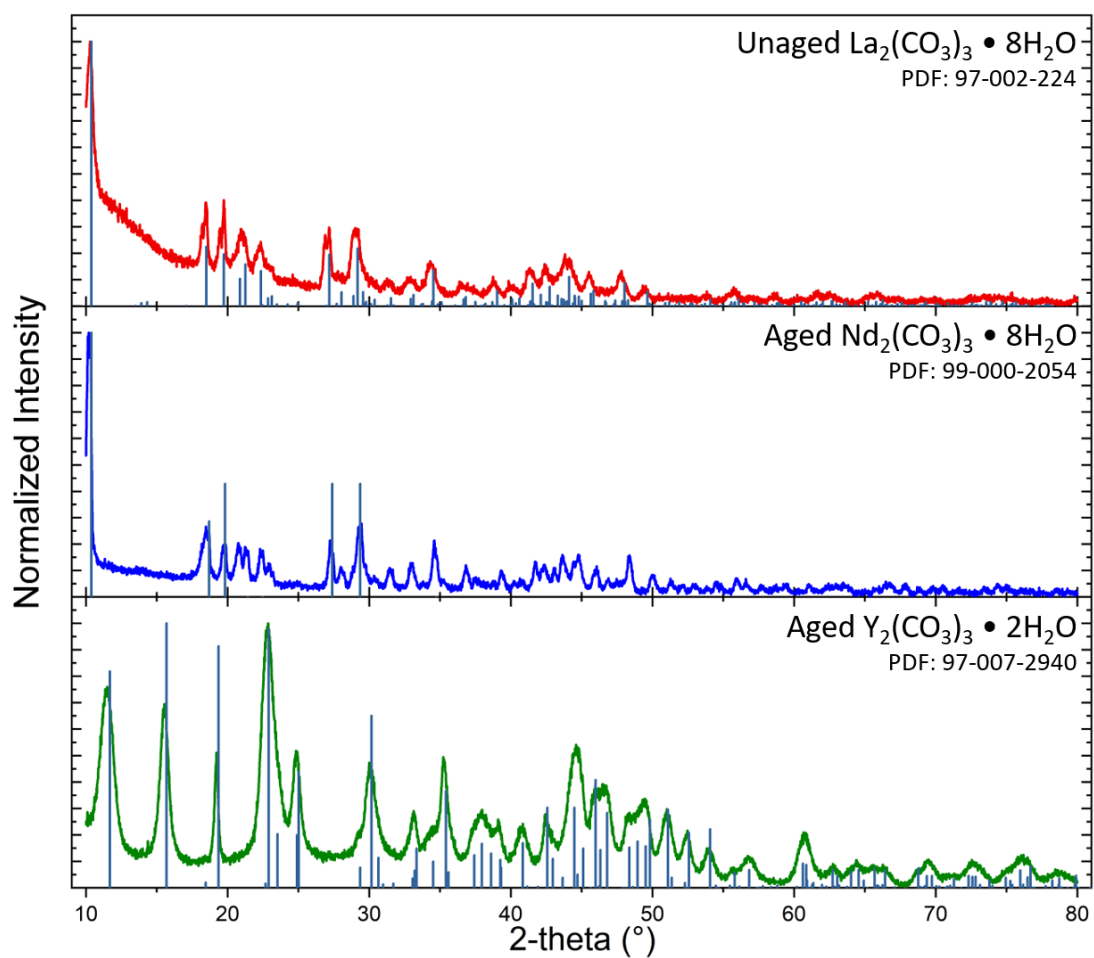


**Figure 3.2.** X-ray diffraction spectra for selected unaged and aged rare earth carbonate samples.

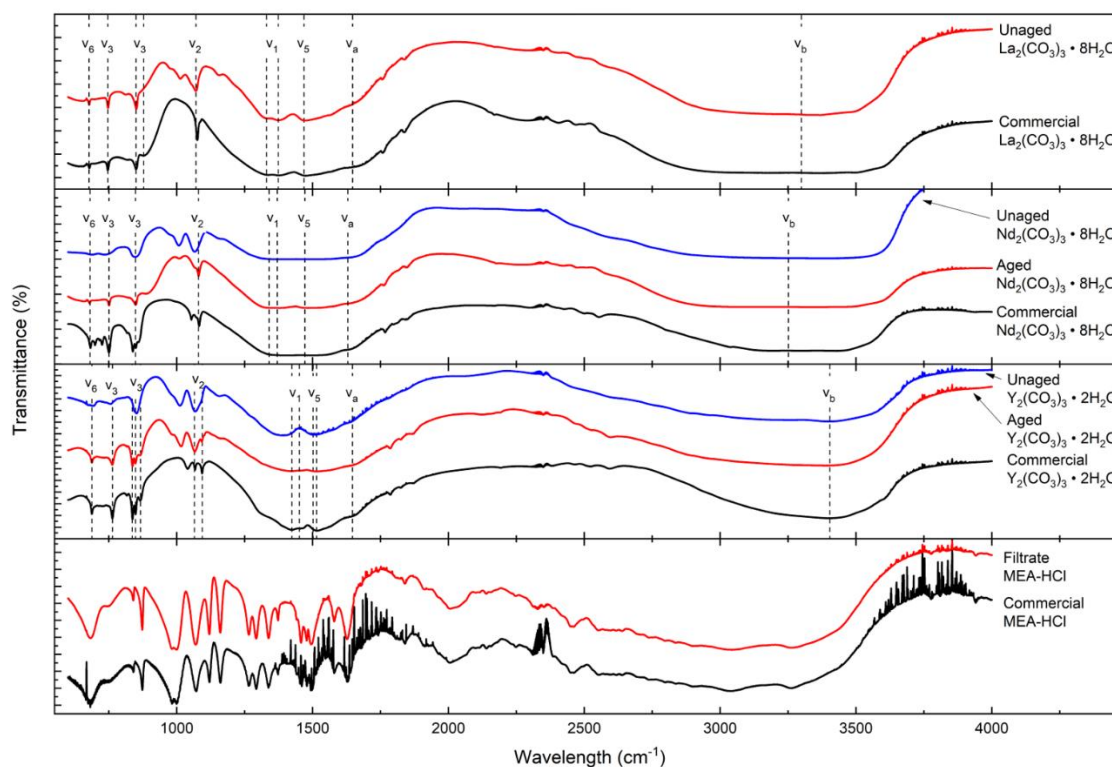


**Figure 3.3.** FTIR spectra of unaged, aged, and commercial variants of the respective rare earth carbonates. Reference positions for known vibration peaks for the respective rare earth carbonates are labeled as v<sub>1</sub> - v<sub>6</sub> with corresponding dotted lines. Exact positions of reference vibration peaks can be found in Table 3.2.

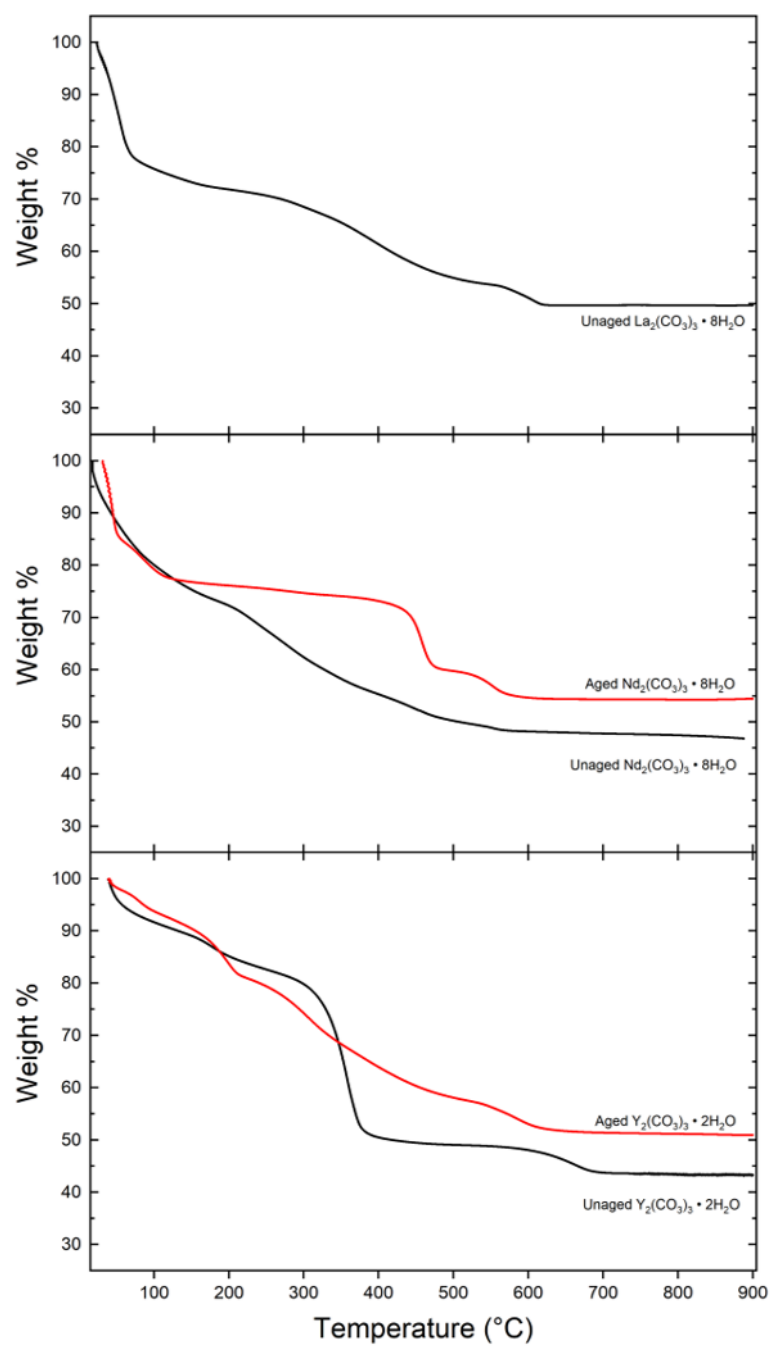


Figure 3.4. Thermal decomposition profiles for the unaged and aged rare earth carbonates.

### 3.6. Tables

**Table 3.1. Inflow solution conditions for select precipitation experiments**

	Rare Earth Conc (m)	MEA Conc (m)	Aging Time (days)
<b>Lanthanum</b>			
La1	$10^{-2}$	0.125	0
La2	$10^{-2}$	0.25	0
<b>Neodymium</b>			
Nd1	$10^{-2}$	0.125	0
Nd2	$10^{-2}$	0.25	0
Nd3	$10^{-2}$	0.25	5
Nd4	$10^{-0.4}$	1.5	0
Nd5	$10^{-0.4}$	2.0	0
Nd6	$10^{-0.4}$	2.5	0
<b>Yttrium</b>			
Y1	$10^{-2}$	0.125	0
Y2	$10^{-2}$	0.25	0
Y3	$10^{-2}$	0.25	5

**Table 3.2. Infrared spectra as reported by Caro et al<sup>45</sup> (Fujita notation, cm<sup>-1</sup>) for the normal carbonates. V<sub>1</sub> – V<sub>6</sub> correspond with those in Figure 3.3.**

	V <sub>6</sub>	V <sub>3</sub>	V <sub>3</sub>	V <sub>2</sub>	V <sub>1</sub>	V <sub>5</sub>	V <sub>a</sub>	V <sub>b</sub>
La <sub>2</sub> (CO <sub>3</sub> ) <sub>3</sub> • 8H <sub>2</sub> O	675 m sp	743 m sp	860 w 850 s sp	1075 m sp	1360 s sp 1330 m sh	1460 s sp	1650 w sh (HOH bending)	3200 – 3400 s b (H <sub>2</sub> O)
Nd <sub>2</sub> (CO <sub>3</sub> ) <sub>3</sub> • 8H <sub>2</sub> O	675 m sp	748 m sp	847 s sp	1080 m sp	1370 s sp 1340 m sh	1470 s sp	1630 w sh (HOH bending)	3200 – 3300 s b (H <sub>2</sub> O)
Y <sub>2</sub> (CO <sub>3</sub> ) <sub>3</sub> • 2H <sub>2</sub> O	683 s sp	760 s sp	862 m 846 s sp 835 s sp	1087 w sp 1062 w sp	1450 w sh 1420 s sh	1540 w sh 1500 s sp	1630 w sh (HOH bending)	3400 b (H <sub>2</sub> O)

Intensity codes: s = strong, m = medium, w = weak, vw = very weak, sp = sharp, b = broad, d = diffuse, & sh = shoulder.

**Table 3.3. Concentrations of rare earth chloride solutions before and after precipitation with MEA as determined by ICP-OES. N/A refers to concentrations below detectable limits.**

	ICP Wavelength (nm)	RE Conc Before (ppm)	RE Conc After (ppm)	Depletion (%)
Lanthanum				
La1	La 379.478	1887.6	N/A	> 99%
	La 384.902	1868.8	7.2	> 99%
La2	La 379.478	1739.4	N/A	> 99%
	La 384.902	1683.6	7.3	> 99%
Neodymium				
Nd1	Nd 401.225	2162.0	N/A	> 99%
	Nd 430.358	2042.0	N/A	> 99%
Nd2	Nd 401.225	2086.0	N/A	> 99%
	Nd 430.358	2010.0	N/A	> 99%
Nd3	Nd 401.225	-	N/A	-
	Nd 430.358	-	N/A	-
Nd4	Nd 401.225	55910	25.7	> 99%
	Nd 430.358	54480	24	> 99%
Nd5	Nd 401.225	57990	3.1	> 99%
	Nd 430.358	55150	3.3	> 99%
Nd6	Nd 401.225	56800	3.2	> 99%
	Nd 430.358	53450	3.4	> 99%
Yttrium				
Y1	Y 360.073	1577.4	N/A	> 99%
	Y 324.227	1595.0	N/A	> 99%
Y2	Y 360.073	1496.8	N/A	> 99%
	Y 324.227	1488.8	N/A	> 99%
Y3	Y 360.073	-	-	-
	Y 324.227	-	-	-

### 3.7. References

1. Gschneidner, Jr, K. A. The Rare Earth Crisis — The Supply / Demand Situation for 2010 – 2015. *Mater. Matters* **6**,
2. Gupta, C. K. & Krishnamurthy, N. *Extractive metallurgy of rare earths*. (CRC Press LLC, 2004).
3. CMI. Critical Materials Institute - Grand Challenge Problems.
4. Haxel, G. B., Hedrick, J. B. & Orris, G. *Rare Earth Elements - Critical Resources for High Technology*. United States Geological Survey (2002).
5. Hurst, C. China's Rare Earth Elements Industry: What Can the West Learn? *Inst. Anal. Glob. Secur.* 43 (2010).
6. U.S. Geological Survey. *Mineral Commodities Summary 2011*. (2011). doi:10.1029/92GL00258
7. Schüler, D., Buchert, M., Liu, D. & Liu, R. Study on Rare Earths and Their Recycling. *Öko-Institut eV ...* **49**, 30–40 (2011).
8. Schüler, D., Buchert, M., Liu, D. & Liu, R. Study on Rare Earths and Their Recycling. *Öko-Institut eV ...* **49**, 30–40 (2011).
9. EPA. Rare Earth Elements : A Review of Production , Processing , Recycling, and Associated Environmental Issues. *United States Environ. Prot. Agency* 135 (2012).
10. Banks, C. V.; Carlson, O. N.; Daane, A. H.; Fassel, V. A.; Fisher, R. W.; Olson, E. H.; Powell, J. E.; and Spedding, F. H. *Studies on the preparation , properties and analysis of high purity yttrium oxide and yttrium metal at the Ames Laboratory*. Ames Laboratory Technical Reports. (1959).
11. Barghusen, J. & Smutz, M. Processing of Monazite Sands. *Ind. Eng. Chem.* **50**, 1754–1755 (1958).
12. Bril, K. J. *Mass Extraction and Separation, Progress in the Science and Technology of the Rare Earths*. **1**, (The Macmillian Company, 1965).
13. de Rohden, C. & Maurice, P. Treatment of monazite. (1957).
14. Hart, K. P. & Levins, D. M. Management of wastes from the processing of rare earth minerals. *Chemeca 88 Aust. Bicenten. Int. Conf. Process Ind. Prepr. Pap.* 82 (1988).
15. Koch, D. F. A. Rare earth extraction and separation. in *In Rare Earth Horizon 1987, Proceedings of a Conference at National Measurement Laboratory* 73–85 (1987).
16. Parker, J.G.; Baroch, C.T.; Adams, J. . *RARE-EARTH ELEMENTS, YTTRIUM, AND THORIUM. A Materials Survey*. (1971).
17. Shaw, K. G. A process for separating thorium compounds from monazite sands. *Retrospective Theses and Dissertations* (Iowa State College, 1953).
18. Smutz, M., Bridger, G.L., Shaw, K.G., and Whatley, M. E. The Ames process for separation



- of monazite, *Chem. Eng. Prog. Symp. Ser.* **13**, 167–170 (1954).
19. Fischer, W., Muller, J. & Niemann, K. E. Separation of the rare earths by fractional precipitation of their carbonates. *Zeitschrift fuer Anorg. und Allg. Chemie* **282**, 63–79 (1955).
  20. He, D., Liao, L. & Xu, R. Precipitation of rare earths with a mixed precipitant. 6 (1989).
  21. He, L. & Gu, Z. Carbonate in separation of mixed rare earth metals. 7 (1991).
  22. Li, Y., Li, M., He, X., Hu, P. & Gu, Z. Precipitation and crystallization of rare earth carbonate. *Zhongguo Youse Jinshu Xuebao* **9**, 165–170 (1999).
  23. Liu, S. & Ma, R. Preparation by crystalline precipitation of mixed rare earth carbonates. *Zhongguo Youse Jinshu Xuebao* **8**, 331–334 (1998).
  24. Osipova, T. P., Bleshinskii, S. V. & Kharakoz, A. E. Sodium carbonate as a reagent for the precipitation of rare earth elements. in (ed. Tananaev, I. V) 27–29 (Khim. Svoistva Soedin. Redkozemel. Elem., Dokl. Vses. Soveshch. Fiz.-Khim. Primen. Redkozemel. Elem., Ikh Soedin. Splavov, 6th, 1973).
  25. Osipova, T. P., Kharakoz, A. E. & Bleshinskii, S. V. Composition of precipitates obtained during the reaction of sodium carbonate with the salts of rare earth elements. *Fiz.-Khim. Issled. Redkozemel. Elem.* 52–60 (1972).
  26. Schmitt, A., Lorenz, H., Richter, H. & Kunze, G. Discontinuous process for the precipitation of rare earth carbonates from aqueous solutions containing other anions and cations. 4 (1986).
  27. Tong, Z., Chen, W. & Guan, X. Manufacture of rare earth carbonates from rare earth sulfates. 10 (1994).
  28. Tselik, I. N.; Deineka, G. F.; Fedorenko, V. D.; Shvartsman, V. Y. Reaction of rare-earth chlorides with potassium carbonate in solution. *Ukr. Khimicheskii Zhurnal* **35**, 1042–1045 (1969).
  29. Tselik, I. N., Shvartsman, V. Y. & Fedorenko, V. D. Composition and thermal stability of carbonates of yttrium group rare earth elements. *Zhurnal Neorg. Khimii* **13**, 106–112 (1968).
  30. Vladescu, C. M. & Iusein, G. Separation of cerium from trivalent lanthanides. 3 (1985).
  31. Yu, Q. & Li, X. Formation of crystalline rare earth carbonates from ore leaching liquors. *Zhongguo Xitu Xuebao* **11**, 171–173 (1993).
  32. Zhao, D. & Pan, X. Precipitation of rare earth with carbonic acid. 4 (1991).
  33. Rao, A. B. & Rubin, E. S. A Technical, Economic, and Environmental Assessment of Amine-Based CO<sub>2</sub> Capture Technology for Power Plant Greenhouse Gas Control. *Environ. Sci. Technol.* **36**, 4467–4475 (2002).
  34. Rochelle, G. T. Amine Scrubbing for CO<sub>2</sub> Capture. *Science (80-. )*. **325**, 1652–1654 (2009).
  35. Metz, B., Davidson, O., de Coninck, H., Loos, M. & Meyer, L. *IPCC Special Report on Carbon Dioxide Capture and Storage. Intergovernmental Panel on Climate Change* (2005).

36. Luis, P. Use of monoethanolamine (MEA) for CO<sub>2</sub> capture in a global scenario: Consequences and alternatives. *Desalination* **380**, 93–99 (2016).
37. Li, K. *et al.* Systematic study of aqueous monoethanolamine-based CO<sub>2</sub> capture process: model development and process improvement. *Energy Sci. Eng.* **4**, 23–39 (2016).
38. Yu, C. H., Huang, C. H. & Tan, C. S. A review of CO<sub>2</sub> capture by absorption and adsorption. *Aerosol Air Qual. Res.* **12**, 745–769 (2012).
39. Lv, B., Guo, B., Zhou, Z. & Jing, G. Mechanisms of CO<sub>2</sub> Capture into Monoethanolamine Solution with Different CO<sub>2</sub> Loading during the Absorption/Desorption Processes. *Environ. Sci. Technol.* **49**, 10728–10735 (2015).
40. Li, Q. *et al.* A Novel Strategy for Carbon Capture and Sequestration by rHLPD Processing. *Front. Energy Res.* **3**, 1–11 (2016).
41. Park, S., Jo, H., Kang, D. & Park, J. A study of CO<sub>2</sub> precipitation method considering an ionic CO<sub>2</sub> and Ca(OH)<sub>2</sub> slurry. *Energy* **75**, 624–629 (2014).
42. Vučak, M., Perić, J. & Krstulović, R. Precipitation of calcium carbonate in a calcium nitrate and monoethanolamine solution. *Powder Technol.* **91**, 69–74 (1997).
43. Vučak, M., Perić, J., Pons, M. N. & Chancel, S. Morphological development in calcium carbonate precipitation by the ethanolamine process. *Powder Technol.* **101**, 1–6 (1999).
44. Park, S., Lee, M.-G. & Park, J. CO<sub>2</sub> (carbon dioxide) fixation by applying new chemical absorption-precipitation methods. *Energy* **59**, 737–742 (2013).
45. Caro, P. E., Sawyer, J. O. & Eyring, L. The infrared spectra of rare earth carbonates. *Spectrochim. Acta Part A Mol. Spectrosc.* **28**, 1167–1173 (1972).
46. Hinode, H., Sharma, R. & Eyring, L. A study of the decomposition of neodymium hydroxy carbonate and neodymium carbonate hydrate. *J. Solid State Chem.* **84**, 102–117 (1990).
47. Sharma, R., Hinode, H. & Eyring, L. A study of the decomposition of praseodymium hydroxy carbonate and praseodymium carbonate hydrate. *J. Solid State Chem.* **92**, 401–419 (1991).
48. Head, E. L. & Holley, C. E. J. *The Preparation and Thermal Decomposition of the Carbonates of Tb, Dy, Ho, Er, Tm, Yb, Lu, Y, AND Sc.* (Los Alamos National Laboratory, 1963). doi:10.2172/4042280
49. Head, E. L. & Holley Jr, C. E. *The Preparation and Thermal Decomposition of Some Rare Earth Carbonates.* (Los Alamos National Laboratory, 1963).
50. Domingues, L. P., Wilfong, R. L. & Furlong, L. R. Pyrolysis of Five Salts of Yttrium, Lanthanum, and Cerium. *Bur. Mines Rep. Investig.* (1962).
51. Foger, K., Hoang, M. & Turney, T. W. Formation and thermal decomposition of rare-earth carbonates. *J. Mater. Sci.* **27**, 77–82 (1992).
52. Wendlandt, Wesley W.; George, T. D. The thermal decomposition of inorganic compounds. IV. Rare earth carbonates. *Texas J. Sci.* **13**, 316–328 (1961).
53. Wilfong, R. L., Domingues, L. P. & Furlong, L. R. Thermogravimetric Analysis of Five Salts of Praseodymium, Neodymium, and Samarium. *J. Am. Ceram. Soc.* **47**, 240–241 (1964).

54. Kim, P., Anderko, A., Navrotsky, A. & Riman, R. Trends in Structure and Thermodynamic Properties of Normal Rare Earth Carbonates and Rare Earth Hydroxycarbonates. *Minerals* **8**, 106 (2018).
55. Charles, R. G. Rare-earth carbonates prepared by homogeneous precipitation. *J. Inorg. Nucl. Chem.* **27**, 1489–1493 (1965).
56. D'Assunção, L. M., Ionashiro, M., Rasesa, D. E. & Giolito, I. Thermal decomposition of the hydrated basic carbonates of lanthanides and yttrium in CO<sub>2</sub> atmosphere. *Thermochim. Acta* **219**, 225–233 (1993).
57. Kutty, T. R. N., Tareen, J. A. K. & Mohammed, I. Correlation between the stability of carbonates in ternary Ln<sub>2</sub>O<sub>3</sub>-H<sub>2</sub>O-CO<sub>2</sub> hydrothermal systems and lanthanide systematics. *J. Less-Common Met.* **105**, 197–209 (1985).
58. Kutty, T. R. N., Mohamed, I. & Tareen, J. A. K. Hydrothermal phase equilibria in Ln<sub>2</sub>O<sub>3</sub>-H<sub>2</sub>O-CO<sub>2</sub> systems for Tm, Yb and Lu. *Mater. Chem. Phys.* **10**, 425–441 (1984).
59. Kutty, T. R. N., Viswanathiah, M. N. & Tareen, J. A. K. Hydrothermal equilibria in Nd<sub>2</sub>O<sub>3</sub> - H<sub>2</sub>O - CO<sub>2</sub> System. *Proc. Indian Acad. Sci. - Chem. Sci.* **87A**, 69–74 (1978).
60. Tareen, J. A. K. & Kutty, T. R. N. Hydrothermal phase equilibria in Ln<sub>2</sub>O<sub>3</sub>-H<sub>2</sub>-CO<sub>2</sub> Systems. *J. Cryst. Growth* **50**, 527–532 (1980).
61. Tareen, J. A. K., Kutty, T. R. N. & Mohamed, I. The Stable Lanthanide Carbonates in the Ln<sub>2</sub>O<sub>3</sub>-H<sub>2</sub>O-CO<sub>2</sub> Systems. *Indian Mineral.* **21**, 43–48 (1980).
62. Carroll, S. A. Precipitation of Nd-Ca carbonate solid solution at 25°C. *Geochim. Cosmochim. Acta* **57**, 3383–3393 (1993).
63. Meinrath, G. & Kim, J. I. Solubility products of different Am (III) and Nd (III) carbonates. *Eur. J. Solid State Inorg. Chem.* **28**, 383–388 (1991).
64. Meinrath, G. & Takeishi, H. Solid-liquid equilibria of Nd<sup>3+</sup> in carbonate solutions. *J. Alloys Compd.* **194**, 93–99 (1993).
65. Runde, W., Meinrath, G. & Kim, J. I. A Study of Solid-Liquid Phase-Equilibria of Trivalent Lanthanide and Actinide Ions in Carbonate Systems. *Radiochim. Acta* **58–9**, 93–100 (1992).
66. Caro, P., Lemaitre-Blaise, M. & Trombe, F. Identification et solubilités des phases solides à l'équilibre sous une atmosphère de gaz carbonique dans les systèmes ternaires oxydes de terres rares-gaz carbon. *Comptes rendus Hebd. des seances l'Academie des Sci. Ser. C* **267**, 1594–1597 (1968).

## **Chapter 4. REFRACTIVE INDEX TUNING OF HYBRID MATERIALS FOR HIGHLY TRANSMISSIVE LUMINESCENT LANTHANIDE PARTICLE – POLYMER COMPOSITES**

### **4.1. Introduction**

Progress on lanthanide-ion-doped materials is developing rapidly due to their optical properties for integrated photonics applications in displays<sup>1,2</sup>, solid-state lasers<sup>2,3</sup>, telecommunications<sup>1,4</sup>, and biomedical imaging<sup>5</sup>. Directly doping polymers with lanthanide ions to create emissive components has proven challenging due to lanthanide ion quenching by the organic ligands and low lanthanide solubility in polymers<sup>6-8</sup>. The low solubility of lanthanide ions results in low emissivity components and a tendency for the lanthanide ions to cluster, leading to self-quenching<sup>6-8</sup>. To resolve this issue, it is desirable to formulate polymer matrix nanocomposites with lanthanide ion doped inorganic particles. Such materials would combine the high quantum efficiency of inorganic phosphors with the ease of polymer processibility.

Transmittance is of great importance for optical composites. Composites with low absorption and scattering values are desirable in integrated photonics that excite at 980 nm and emit at 1530 nm<sup>7</sup>. These are the wavelengths where the nanocomposite must have a transmittance close to unity as possible. However, this is a challenging goal. Loss factors on the order of 2 db/cm are required for integrated photonics. According to Rayleigh scattering theory, transparent nanocomposites with low scattering require particle or agglomerate sizes on the order of  $1/20^{\text{th}}$  of the wavelength(s)<sup>9-13</sup>. Optical losses due to scattering by particles proportionally increases to the 6<sup>th</sup> power with particle size. Light scattering also increases to the square (2<sup>nd</sup> power) of the difference in refractive index between the particle(s) and the matrix. Reducing particle size and/or reducing refractive index mismatch decreases scattering. The latter is the focus of this work.

For this application, refractive index (RI) matching has greater merits than attempts to reduce the particle size of the emitter. First, luminescence intensity and emission lifetime of lanthanide-ion-doped particles increase with increasing particle size<sup>14–17</sup>, especially as the nano- to micro- meter size range is traversed. This is because the surface area to volume ratio for a nanoparticle decreases with increasing particle size. The decreasing surface area to volume ratio with increasing particle size results in smaller amounts of lanthanide ions at particle surfaces affected by 4f-4f electronic transition quenching surface groups such as hydroxyls and organic ligands. Second, the ability to deagglomerate particles greatly improves with increasing particle size because of the relatively decreasing contribution of the attractive van der Waals forces while decreasing surface free energy and proportionally scaling mechanically-convective forces (e.g., gravity, fluid, shear, etc.) accounts for the improved deagglomeration. Proper deagglomeration along with dispersion stabilization enables better composite chemical and physical homogeneity which better ensures uniform optical properties. Furthermore, luminescent lanthanide-ion-doped particles on the order tens of nanometers<sup>18–21</sup> are made at dilute conditions, making synthesis of large quantities of these nanomaterials time-consuming and expensive. While the synthesis of micron-sized powders yields luminescent particles with greater quantum efficiencies in greater quantities, decreasing overall cost. Furthermore, even if nanoparticles can be synthesized cost effectively, surface modification of these nanoparticles required to deagglomerate and stabilize them in a polymer matrix<sup>11,22–25</sup> could degrade their optical performance due to quenching by the ligands<sup>14,26</sup>.

Rayleigh theory predicts that when refractive index mismatch ( $\Delta n$ ), the difference in refractive index between that of the particles ( $n_p$ ) and that of the matrix ( $n_m$ ), goes to zero ( $\Delta n = n_p - n_m = 0$ ), scattering loss goes to zero and transmittance becomes independent of particle size and light wavelength(s). Transparent polymer composites fabricated using the principle of “RI

matching” have been reported<sup>22,23,27</sup>. For example, Tan et al. has shown that polystyrene (PS)/CeF<sub>3</sub>:Yb-Er composites have higher transmittance than polymethylmethacrylate (PMMA)/CeF<sub>3</sub>:Yb-Er composites with CeF<sub>3</sub>:Yb-Er size and loading remaining constant between the systems<sup>19</sup>. They demonstrated that the PS/CeF<sub>3</sub>:Yb-Er composites were more transparent since they have lower RI mismatch (0.03) than that of the PMMA composites (0.12). When the RI mismatch was low, higher transmittance could be achieved even with a high particle loading of 20 vol%. Yet higher transmittance can be achieved if the RI mismatch between the polymer matrix and the phosphor particles could be further decreased. A greater degree of control over the RI of the polymer matrix in general would afford these transmittance improvements.

The RI of polymer matrices, such as acrylates, polyimides, and olefins, can be tuned via blending and copolymerization methods with an accuracy of greater than 0.0001<sup>28</sup>. However, the RIs of polymers range from 1.30 to 1.80, limiting their use as RI matching materials for particles that have RIs within this narrow range<sup>29</sup>, precluding the lanthanide oxides ( $n = 1.85 - 2.20$ ,  $\lambda = 980$  nm)<sup>30,31</sup> but encompass the range of RIs for the lanthanide fluorides ( $n = 1.40 - 1.63$ ,  $\lambda = 980$  nm)<sup>32</sup> and fluoride host materials (e.g., NaYF<sub>4</sub> ( $n = 1.48$ ,  $\lambda = 500$  nm) and CaF<sub>2</sub> ( $n = 1.43$ ,  $\lambda = 980$  nm)<sup>33</sup>).

Another strategy for fabricating high RI polymers is to blend high RI, sub-10 nm inorganic nanoparticles with relatively low RI polymers, which are both low-cost and highly transmissive. Highly dispersible materials such as anatase TiO<sub>2</sub> ( $n = 2.10$ ,  $\lambda = 980$  nm), rutile TiO<sub>2</sub> ( $n = 2.50$ ,  $\lambda = 980$  nm), ZrO<sub>2</sub> ( $n = 2.10$ ,  $\lambda = 980$  nm), and silicon ( $n = 3.58$ ,  $\lambda = 980$  nm) can be used to increase the RI of a polymer matrix by controlling their volume fraction in the polymer matrix<sup>13,34-39</sup>. Based upon the Maxwell-Garnett and Lorentz-Lorenz effective medium approximations, the RI of a blended polymer matrix can vary from that of the pure polymer to a value greater than that of the polymer but less than that of the inorganic nanoparticle(s)<sup>40,41</sup>; the upper bound on the RI range is fluid and is determined by the amount of inorganic nanoparticles that can be loaded into

the polymer matrix. Methods to fabricate high RI polymer nanocomposites include sol-gel<sup>42,43</sup>, *in-situ* synthesis<sup>44,45</sup>, and *ex-situ* blending<sup>40,46,47</sup>.

Lanthanum fluoride (LaF<sub>3</sub>) was chosen as the host material for the rare-earth ions due to its relatively low phonon energy ( $\sim 350 \text{ cm}^{-1}$ ) and RI ( $n = 1.604$ ). The low phonon energy of the LaF<sub>3</sub> is particularly important as reducing the phonon energy increases the radiative transition probabilities for lanthanide ions. The 1530 nm ( $^4I_{13/2} \rightarrow ^4I_{15/2}$ ) radiative emission from Er<sup>3+</sup> is important for integrated photonics. Lanthanum fluoride doped with ytterbium and erbium ions is well known to emit brightly at 1530 nm when excited at 975 nm<sup>22</sup>. High phonon energy host materials such as silica (SiO<sub>2</sub>,  $\sim 1100 \text{ cm}^{-1}$ ) increases non-radiative transitions for the lanthanide ions, decreasing emission intensity. Lower phonon energy host materials such as lanthanum chloride (LaCl<sub>3</sub>,  $\sim 260 \text{ cm}^{-1}$ ) are chemically unstable or difficult to produce in large, cost effective quantities, thus unsuitable as phosphors.

This work will demonstrate RI matching is a highly effective strategy in the preparation of lanthanum fluoride-polymer composites with transparency suitable for this excitation-emission scheme (Figure 4.1).

## 4.2. Experimental Sections

### 4.2.1. Hydrothermal Synthesis of La<sub>0.92</sub>Yb<sub>0.075</sub>Er<sub>0.005</sub>F<sub>3</sub> Nanoparticles

La<sub>0.92</sub>Yb<sub>0.075</sub>Er<sub>0.005</sub>F<sub>3</sub> (LYEF) was synthesized via a hydrothermal process in 125 ml Parr<sup>®</sup> Acid Digestion Bombs (Parr Instrument Company, Moline, Illinois, USA). The solvent was water with 18.2 MΩ-cm electrical resistivity as dispensed by Rios5/MilliQ water purification system from EMD Millipore (Billerica, Massachusetts, USA). 99.99% metals basis lanthanum (III) nitrate hexahydrate (La(NO<sub>3</sub>)<sub>3</sub> · 6H<sub>2</sub>O), 99.9% metals basis ytterbium (III) nitrate pentahydrate (Yb(NO<sub>3</sub>)<sub>3</sub>

• 5H<sub>2</sub>O), 99.9% metals basis erbium (III) nitrate pentahydrate (Er(NO<sub>3</sub>)<sub>3</sub> • 5H<sub>2</sub>O), and ≥98.0% ACS reagent ammonium fluoride (NH<sub>4</sub>F) were purchased from Sigma Aldrich (Saint Louis, Missouri, USA) and used without additional purification. Rare earth salts and NH<sub>4</sub>F were mixed to make an aqueous solution with the final concentrations of 0.32 M La(NO<sub>3</sub>)<sub>3</sub>, 0.026 M Yb(NO<sub>3</sub>)<sub>3</sub>, 0.0018 M Er(NO<sub>3</sub>)<sub>3</sub>, and 1.04 M NH<sub>4</sub>F. Solution pH was then adjusted to ~1.5 using ACS reagent grade nitric acid (70 wt%, Fisher Scientific, Pittsburgh, Pennsylvania, USA) to ensure complete dissolution of all precursors. pH was measured using a HI 2221 Calibration Check pH/ORP Meter (Hanna Instruments Ltd, Bedfordshire, England, UK).

70 mL of the solution was placed into a Teflon® liner of a 125 ml Parr® Acid Digestion Bomb (Parr Instrument Company, Moline, Illinois, USA), which was then fully sealed. The sealed vessel(s) was placed in a VWR Sheldon Lab 1430m Vacuum Oven (VWR International, Radnor, Pennsylvania, USA) at 240 °C for 16 h with no applied vacuum. The vessel(s) was removed and allowed to ambiently cool to room temperature. Upon opening, a solid white precipitate was observed at the bottom. The precipitate cake was broken up using a Teflon™ spatula and was then transferred to 50 mL Nalgene®, Oak Ridge Style 3119, centrifuge tubes (Sigma Aldrich, Saint Louis, Missouri, USA). The precipitate and reaction solution were then washed and centrifuged with 30 mL of absolute ethanol (Fisher Scientific, Pittsburgh, Pennsylvania, USA) three times at 10,000 g using a Beckman Coulter Avanti J-26 XP Centrifuge (Brea, California, USA). The precipitate was washed and centrifuged with 30 mL of 18.2 MΩ deionized water once at 10,000g. The precipitate was placed back into the VWR Sheldon Lab 1430m Vacuum Oven at ~70 °C overnight with no applied vacuum. The dried precipitate was then ground into a fine powder using an agate mortar and pestle (Sigma Aldrich, Saint Louis, Missouri, USA). No further modification(s) to the LYEF were conducted.



#### 4.2.2. Composite Synthesis

CN551 (amine modified polyether acrylate oligomer,  $\rho = 1.15 \text{ g/cm}^3$ ) was donated by Sartomer (Exton, Pennsylvania, USA). CN551 is a highly reactive amine modified polyetheracrylate oligomer, which experiences less shrinkage than other common monomers upon polymerization. The photoinitiator, IRGACURE 819, purchased from BASF (Ludwigshafen, Germany), allows for the *in-situ* polymerization of the CN551 oligomers under UV-light. *In-situ* polymerization has been widely used to synthesize highly transparent bulk nanocomposites<sup>10,24,25</sup>. Propylene glycol monomethyl ether acetate (PGMEA) was purchased from Sigma-Aldrich. Zirconium dioxide ( $\text{ZrO}_2$ ,  $\rho = 5.68 \text{ g/cm}^3$ ) nanoparticles dispersed in PGMEA, 4 – 6 nm in diameter (PixClear™-PA), were purchased from Pixelligent (Baltimore, Maryland, USA) and were reported to be the tetragonal polymorph with no mention of added stabilizers such as magnesium or yttrium. The  $\text{ZrO}_2$  nanoparticle surfaces were modified with a Pixelligent proprietary ligand that increases their dispersion in an acrylic-based polymer matrix.  $\text{ZrO}_2$  is a high RI oxide that has no absorption in the visible and IR region. The RI of bulk, tetragonal  $\text{ZrO}_2$  is  $\sim 2.10$  at  $\lambda = 980 \text{ nm}$ . The exact compositions of the nanocomposite materials are reported in both weight percent and volume percent of the individual fractions (Table 4.1 – 4.3).

CN551,  $\text{ZrO}_2$ , IRGACURE 819, and LYEF were blended into the PGMEA solvent. IRGACURE 819 was fixed at 2 weight% relative to CN551 resins in each sample. The mixtures were then sonicated for 2 min using a QSonica probe sonicator (Newtown, Connecticut, USA). The suspensions were uniform but turbid due to LYEF agglomeration. The solutions were then immediately drop-cast onto glass slides to avoid precipitation. These samples were dried on a  $40^\circ\text{C}$  hot plate for 12 h to evaporate excess solvent. The samples were placed in a vacuum oven for 10 min to remove any excess solvent so as to prevent void formation. Samples were then cross-linked using a pulsed UV xenon lamp (XENON RC-500, Wilmington, Massachusetts, USA) with a dose of  $8 \text{ J/cm}^2$ . To measure

refractive indices of each component used in the nanocomposites, suspensions and solutions of  $\text{ZrO}_2$ , IRGACURE 819, and CN551 were spin-coated onto silicon wafers using PGMEA as a solvent. All spin-coated films were approximately 20 microns thick.

#### *4.2.3. Characterization*

Structure and phase of the LYEF powders were characterized using powder X-ray diffraction on a Bruker D8 Discover (Bruker AXS, Inc, Madison, Wisconsin, USA) with a step size of  $0.018^\circ$  ( $2\theta$ ) with a 0.5 s dwell time. The instrument was equipped with a Vantec 1 Detector, copper K-alpha source operating at 40 kV and 40 mA (1600 Watts), and a horizontal goniometer. Pattern-fitting and Rietveld-analysis were conducted using MDI Jade 9 (Materials Data, Inc., Livermore, California, USA) equipped with Fachinformationszentrum Karlsruhe/National Institute of Standards and Technology Inorganic Crystal Structure Database (FIZ/NIST ICSD, National Institute of Standards and Technology, Gaithersburg, Maryland, USA).

Scanning electron micrographs of the as-synthesized LYEF powders were collected using a Zeiss Sigma Field Emission Scanning Electron Microscope (FESEM, Zeiss United States, Thornwood, New York, USA) operating at a 20 kV accelerating voltage and a working distance of 8.5 mm. Samples were prepared by first grinding them with mortar and pestle to break-up large agglomerates. The powdered samples were gently dusted onto 8 mm carbon tape coated SEM studs (Electron Microscopy Sciences, Hatfield, Pennsylvania, USA). Excess powder was removed with gentle blasts of pressurized air from a house compressed air line. The powders were then coated with 10 nm of gold using an EMS150T ES Turbo-Pumped Sputter Coater (Electron Microscopy Sciences, Hatfield, Pennsylvania, USA) to improve sample conductivity. Multiple micrographs of LYEF samples containing at least 50 well dispersed particles in different locations were collected to

ensure a representative description of the samples were obtained. Composite cross sections were analyzed with an FEI Magellan FESEM (Hillsboro, Oregon, USA).

Steady state spectra of LYEF powders and LYEF/polymer nanocomposites were collected using an FSP920 Spectrometer (Edinburgh Instruments, Livingston, UK) equipped with a Hamamatsu G5852-23 InGaAs detector and a Hamamatsu R928P Photomultiplier Tube for infrared and visible ranges, respectively. Detector limitations hindered the reliable measurement of lifetime values for the  $^4I_{13/2} \rightarrow ^4I_{15/2}$  (1530 nm) transition in composite samples with low LYEF vol% and/or large  $ZrO_2$  vol%. Both powder and nanocomposite samples were irradiated with an external 2.5 watt, 976 nm diode laser (B&W Tek, Newark, Delaware, USA) focused into a 3 mm diameter spot. 1530 nm decay (lifetime) measurements were also collected with the FSP920 Spectrometer, but with an external TDS 200 Digital Oscilloscope (Tektronix, Beaverton, Oregon, USA) connected to a Hamamatsu G5852-23 analog InGaAs detector. Powder samples were pressed into 10 mm pellets for spectral measurements. Composite samples were measured as synthesized. Scan parameters such as emission slit width ( $\Delta\lambda = 0.5$  nm) and integration time ( $t = 0.10$  sec) were kept constant between all samples.

The refractive indices of the  $ZrO_2/CN551$  nanocomposites were measured using the RC2 Spectroscopic Ellipsometer with an NIR extension (J.A.Woollam Inc., Co., Lincoln, Nebraska, USA) and analyzed using the CompleteEASE software (J.A.Woollam Inc., Co., Lincoln, Nebraska, USA). Data was collected in the wavelength range of 193 - 1690 nm, using incident angles from 55 to 70° in 5° increments. The data was fitted using the Cauchy model, over the Sellmeier fit, using select wavelengths from 400 to 1690 nm to obtain film thickness and RI. Differences between the Cauchy model and Sellmeier fit were found to be minimal within the range of properties studied<sup>48</sup>. Data fitting with the Cauchy model was reasonable for our materials as the films were transparent and have minimum absorption over the selected wavelength range. Transmittance spectra of

coatings on glass slides were obtained using a PerkinElmer Lambda 1050 UV-Vis-NIR spectrometer (Waltham, Massachusetts, USA). Direct transmittance spectra data was collected from 380 to 1200 nm with a resolution of 5 nm. Transmittance measurements also include losses due to Fresnel reflections, which are expected to be 10% or less for each interface with a difference in refractive index. Approximate losses due to Fresnel reflectance can be calculated using the reflectance equation. Haze was measured using a PerkinElmer Lambda 1050 UV-Vis-NIR spectrometer equipped with an integrating sphere. Haze measurements were conducted as per the procedure outlined by ASTM D1003-92<sup>49</sup>. In brief, four transmission scans of the sample ranging from 380 to 780 nm utilizing four different measurement configurations (Figure 4.2) were required. The integral of the transmission curve(s) with respect to wavelength were then incorporated into the Haze equation as defined by ASTM D1003-92.

#### 4.3. Results and Discussion

The LYEF synthesized via the hydrothermal method is phase pure fluocerite (PDF#: 97-001-6964, Figure 4.3) with approximate primary particle sizes of 70 nm (Figure 4.4a). Shifts in peak locations are attributed to doping by  $\text{Yb}^{3+}$  and  $\text{Er}^{3+}$  ions. Cross-sections of [LYEF]-[CN551] composites at different LYEF vol% (Figure 4.4b – d) show increasing degrees of agglomeration with increased LYEF loading, with effective particle sizes of hundreds of nanometers at high LYEF vol%. These agglomerates cause large amounts of scattering and decrease light transmittance of the composite films.

To improve the optical transmittance of these composites,  $\text{ZrO}_2$  nanoparticles were incorporated at volume fractions ranging from 0 to 54.1 vol%. The RIs of the [ $\text{ZrO}_2$ -CN551] nanocomposites with respect to  $\text{ZrO}_2$  vol% show increasing RI with increasing  $\text{ZrO}_2$  vol% (Figure 4.5). Nanocomposite RI at  $\lambda = 1530$  nm increased from 1.485 to 1.655 as  $\text{ZrO}_2$  volume fraction increased from 0 to 54.1

vol%. Since the RI of LYEF is 1.574 at  $\lambda = 1530$  nm, a 20.3 vol% ZrO<sub>2</sub> loading in CN551 will create a RI match.

The transmittance of 20  $\mu$ m thick [LYEF]-[CN551-ZrO<sub>2</sub>] nanocomposites containing 5 vol% LYEF as a function of ZrO<sub>2</sub> solids loading (Table 4.1) shows that nanocomposite transmission is maximized when the expected RI of the matrix matches that of LYEF (Figure 4.6a). From 0 to 20.3 vol% ZrO<sub>2</sub>, transmittance increased to greater than 89%, but then dropped below 80% once the ZrO<sub>2</sub> loading exceeded 20.3 vol%. Increased light scattering occurred proportionately with RI mismatch when the RI of the matrix is either smaller or greater than of the phosphor. The observed maximum transmittance at 20.3 vol% ZrO<sub>2</sub> (Figure 4.6b) corresponds to the experimentally determined ZrO<sub>2</sub> vol% associated with a minimal RI mismatch between the matrix and the phosphor ( $RI_{\text{matrix}} \approx RI_{\text{phosphor}}$ ). This maximum transmittance ZrO<sub>2</sub> vol% corresponds with the theoretically determined ZrO<sub>2</sub> vol% per the Maxwell-Garnett (MG) and Lorentz-Lorenz (LL) effective medium approaches (Figure 4.5c). Loading beyond 20.3 vol% ZrO<sub>2</sub> decreased transmittance due to scattering at the phosphor/matrix interface(s). Increasing RI mismatch between the matrix and the phosphor accounted for the proportionally increasing scattering (Figure 4.5b). Transmittance data for 15 vol% [LYEF]-[CN551-ZrO<sub>2</sub>] and 30 vol% [LYEF]-[CN551-ZrO<sub>2</sub>] composites demonstrate the same behavior as demonstrated by the 5 vol% [LYEF]-[CN551-ZrO<sub>2</sub>] composites (Figure 4.7a and 4.7b, respectively). At both 15 vol% and 30 vol% LYEF, optical transmission is maximized when the  $RI_{\text{matrix}}$  experimentally matches that of LYEF. Differences between the experimentally determined RI for the composites and theoretically determined RIs via MG and LL approximations at higher ZrO<sub>2</sub> solids loading (> 20 vol%) can be attributed to the difficulties in experimental processing associated with evenly dispersing the large volume fractions of ZrO<sub>2</sub>. However, it should be noted

that both MG and LL approaches accurately approximate composite RIs at low ZrO<sub>2</sub> solids loading and up to the RI match point (Figure 4.5c).

Transmittance haze measurements (Figure 4.2), which are used to determine the degree of wide angle scattering (> 2.5 degrees from transmission axis), of 5 vol% [LYEF]-[CN551-ZrO<sub>2</sub>] composites (Figure 4.6b) showed that at the expected RI match point ( $RI_{\text{matrix}} = RI_{\text{LYEF}}$ ) of 20.3 vol% of ZrO<sub>2</sub>, wide angle scattering disappears. Nanocomposites loaded with either too little or too much ZrO<sub>2</sub> exhibited increased haze. Combined with transmittance data, wide angle scattering accounts for much of the optical losses in samples where the effective matrix RI does not match that of the LYEF. In all samples, optical absorption contributes to decreased transmittance. This is apparent in the RI matched sample (20.3 vol% ZrO<sub>2</sub>) where maximum transmittance is achieved.

However, a composite material must have a stable microstructure in order for its properties, and therefore function, to remain unchanged. Qualitative observations and photospectrometry measurements made many months after synthesis (Figure 4.8) were suggestive of an evolving microstructure. Qualitatively, all samples increased in optical opacity with composites without ZrO<sub>2</sub> loading being nearly opaque. Photospectrometry measurements (Figure 4.8) show a general correlation between emission intensity and ZrO<sub>2</sub> loading: decreasing emission intensity with increasing ZrO<sub>2</sub> loading. Theoretical interparticle spacing (IPS)<sup>50</sup> calculations (Figure 4.9 & 4.10) help demonstrate the reason for the evolving microstructures and this general trend in emission intensity.

For a constant ZrO<sub>2</sub> vol% (Figure 4.9 & 4.10), increasing the amount of LYEF will decrease the average interparticle spacing (IPS)<sup>50</sup> between ZrO<sub>2</sub> nanoparticles, eventually crossing the 20 nm threshold (Figure 4.10) at which van der Waals forces will overcome repulsive forces between the ZrO<sub>2</sub> nanoparticles. This is also observed in high ZrO<sub>2</sub> vol% systems with no LYEF solids loading.

For an established  $\text{ZrO}_2$  particle size ( $r = 4 \text{ nm}$ ) (Figure 4.10a), increasing  $\text{ZrO}_2$  vol% rapidly decreases  $\text{ZrO}_2$  IPS, which further decreases when loading LYEF. At a given  $\text{ZrO}_2$  vol% (Figure 4.10b), increasing  $\text{ZrO}_2$  particle size increases the amount of LYEF vol% that the system is able to incorporate before the 20-nm aggregation threshold is reached, as larger particles begin at a greater IPS. The same logic used to demonstrate the agglomeration of  $\text{ZrO}_2$  can also be applied to LYEF. In general, emission intensity for a RE-doped phosphor increases with particle/agglomerate size and this is reflected in the composite microstructures. Decreasing emission intensity with increasing  $\text{ZrO}_2$  loading points to the fact that the degree of LYEF agglomeration decreases with increasing  $\text{ZrO}_2$  loading. Composite opacity at low  $\text{ZrO}_2$  solids loadings can be linked to the high degree of LYEF agglomeration due to the lack of  $\text{ZrO}_2$  particles to physical lock the LYEF particles in place. The low  $\text{ZrO}_2$  solids loading also results in a RI mismatch between the matrix and the LYEF, further exacerbating this light scattering condition. Increasing  $\text{ZrO}_2$  solids loading may decrease the degree of LYEF agglomeration, but the resulting  $\text{ZrO}_2$  agglomeration due to LYEF induced crowding creates an optically heterogeneous medium. Emission intensity can be increased with greater LYEF solids loading, but this eventually results in decreased light transmission due to light scattering by  $\text{ZrO}_2$  agglomerates (Figure 4.9) because of the crowding by LYEF (Figure 4.10). This decreased transmission is further compounded by the fact the matrix is now optically heterogeneous and the matrix RI no longer matches that of the LYEF, resulting in light scattering by the LYEF as well.

The exact composition of the ligands coating the surfaces of the particles,  $\text{ZrO}_2$  and LYEF, also affect their stability in the matrix. In this study, the  $\text{ZrO}_2$  particles were coated with a Pixelligent proprietary ligand meant to help improve their dispersion in the matrix. The LYEF particles were uncoated. These ligands ultimately place an upper limit  $\text{ZrO}_2$  loading and affects the crowding of the LYEF particles by the  $\text{ZrO}_2$  particles and the  $\text{ZrO}_2$  particles by themselves. As aforementioned,

this helps determine how much of the particles we can load into a system before agglomeration destabilizes the system, resulting in an optically heterogeneous matrix and a composite with large amounts of optical opacity due to agglomerate/particle induced light scattering. Arbitrary combinations of particles, surface ligands, and matrix in further efforts will result in difficulties achieving stable, optically active, and highly transmissive composites. Exact ligand chemistry, and its interaction with the matrix, affects the optimum concentrations of LYEF particles and  $\text{ZrO}_2$  particles required to achieve maximum emission intensity, high transmittance, refractive index match between the LYEF and the blended matrix, and nanocomposite stability.

Characterization of the nanocomposites immediately following their synthesis has demonstrated that the RI matching methodology improves light transmission, but subsequent characterization and observation(s) at later dates has shown the need to further optimize this methodology in order to ensure nanocomposite stability with regards to optical properties by accounting for the initial conditions that result in particle agglomeration. This may be accomplished by improving the stability of the polymer and/or better tailoring the solids loading amounts and schemes required to create and maintain an optically active nanocomposite and optically homogeneous medium.

#### **4.4. Conclusions**

Nanocomposites containing LYEF particles were fabricated using *in-situ* polymerization. Nanocomposites containing only LYEF and the CN551 polymer exhibited large amounts of scattering due to LYEF agglomeration, the degree of which increased with LYEF vol%. By homogeneously dispersing small  $\text{ZrO}_2$  particles into the polymers, the [CN551- $\text{ZrO}_2$ ] nanocomposites form an optically homogeneous medium, and the effective RI of the  $\text{ZrO}_2$ /polymer composites can be precisely tuned. High transmittance composites can be



synthesized by well mixing the three components together in a solvent and casting on to substrates. These composites are mechanically robust enough to undergo a moderate amount of bending by hand without tearing. However, we have also demonstrated further optimization is required in order to ensure that polymer relaxation over time due to either the inherent properties of the polymer or solvent evaporation does not help change particle distribution in the composite. Careful consideration thus need be given to particle loading fractions that take into account changes in the polymer phase over time. This will slightly limit the potential range of tunability of this system, but these findings provide significant insights into composite design choices, such as starting RI of the matrix. It should also be noted that the exact chemistry of the ligands used to coat particle surfaces will place an upper limit on the solids loading of the particles in a given matrix. This will affect the exact solids loading requirements necessary to achieve composite stability, high emission intensity, and optical transparency. Further efforts to utilize this methodology should take this into consideration when selecting for different combinations of a low refractive index polymer-matrix, a high refractive index particle-tuning-phase (with associated surface ligand), and a medium refractive index optically active particle-phase (with associated surface ligand). This is the first demonstration of hybrid composites being used as the RI matching matrix to fabricate transparent composites. A potential application of this method is the fabrication of optical amplifiers; printing optical amplifiers with grating structures via soft imprint lithography is an important future work with efforts already underway.

## 4.5. Figures

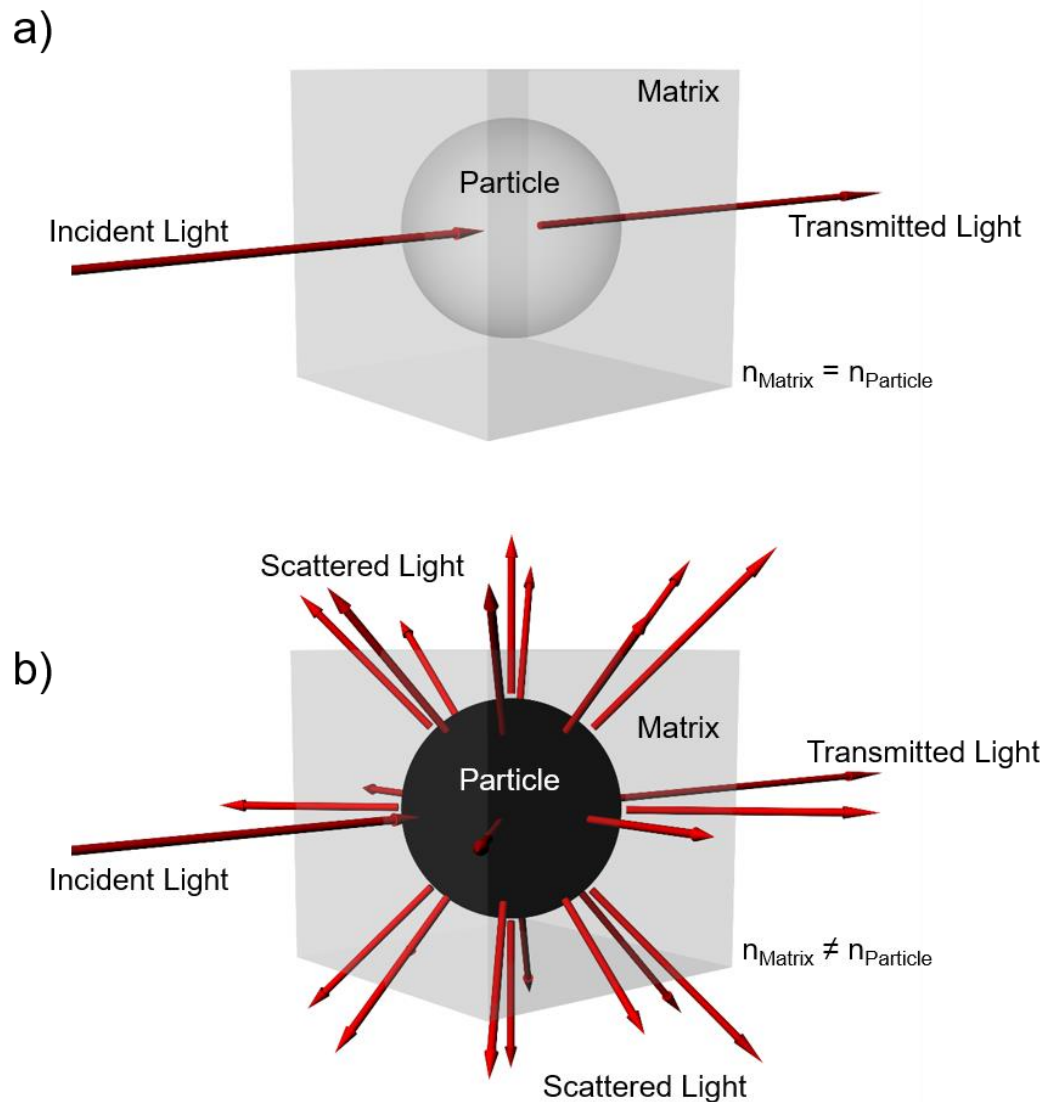


**Figure 4.11.** Illustration of achieving high transmittance through RI matching. a) Incident light is transmitted through the optically homogeneous medium with no scattering ( $n_{\text{matrix}} = n_{\text{particle}}$ ). b) Incident light is scattered by the particle as the medium is not optically homogeneous ( $n_{\text{matrix}} \neq n_{\text{particle}}$ ).

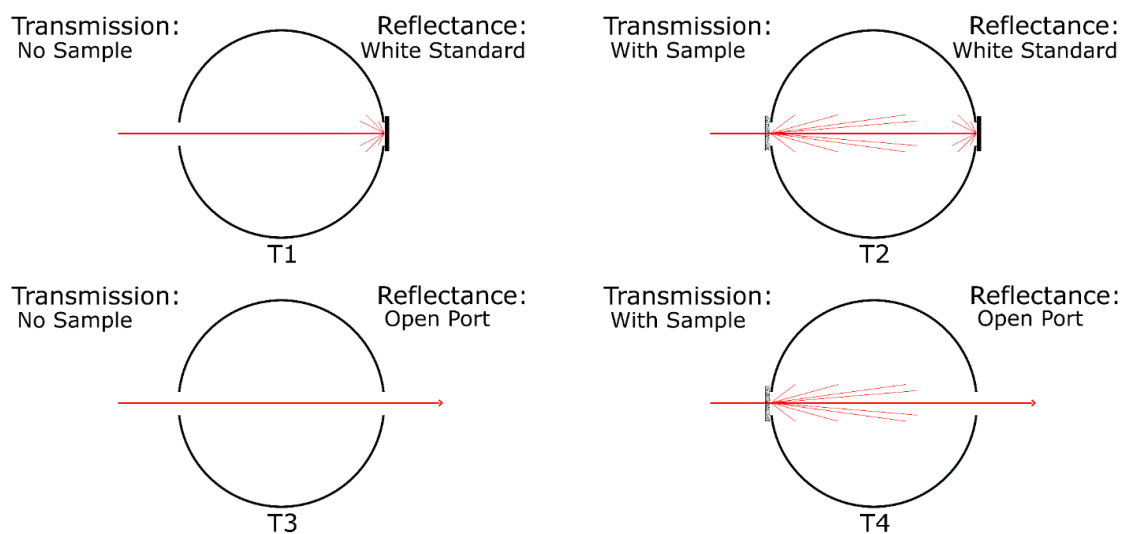


**Figure 4.2.** Schematic for the ASTM 1003-92 standard for the measurement of polymer material haze. Composite samples are placed in the locations dictated by T2 and T4.

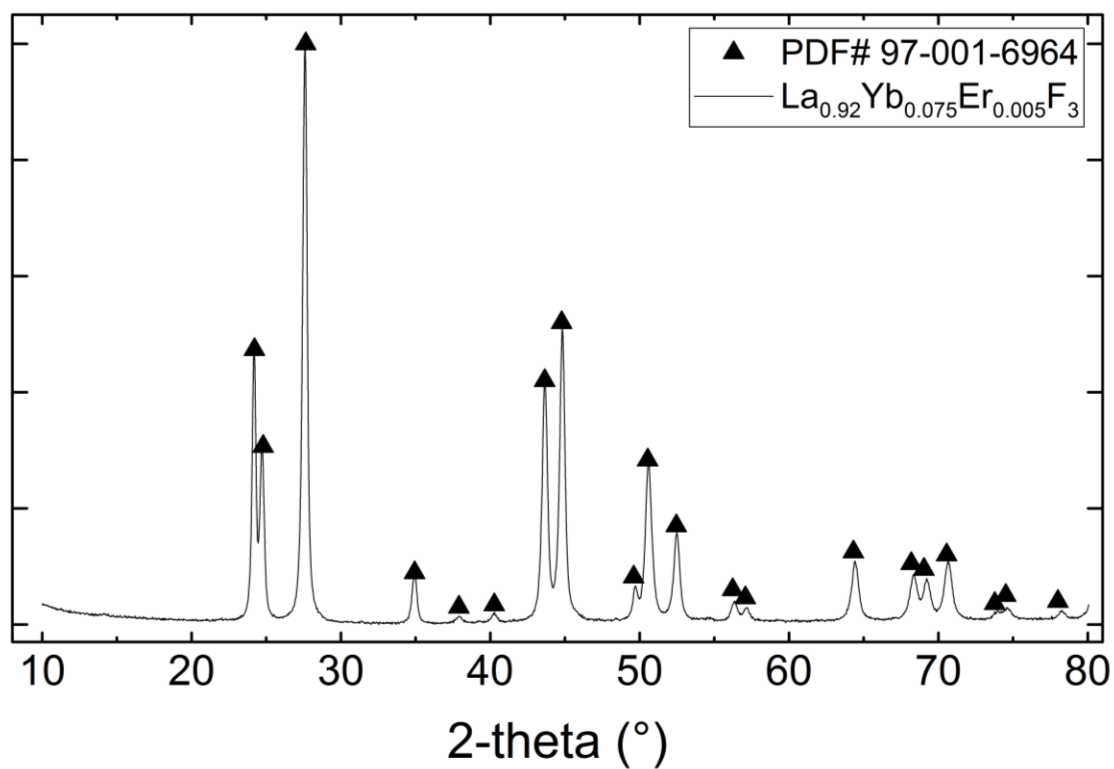


**Figure 4.3.** X-ray diffraction spectrum of  $\text{La}_{0.92}\text{Yb}_{0.075}\text{Er}_{0.005}\text{F}_3$  powders exhibiting characteristic peaks for fluocerite (PDF# 97-001-6964).

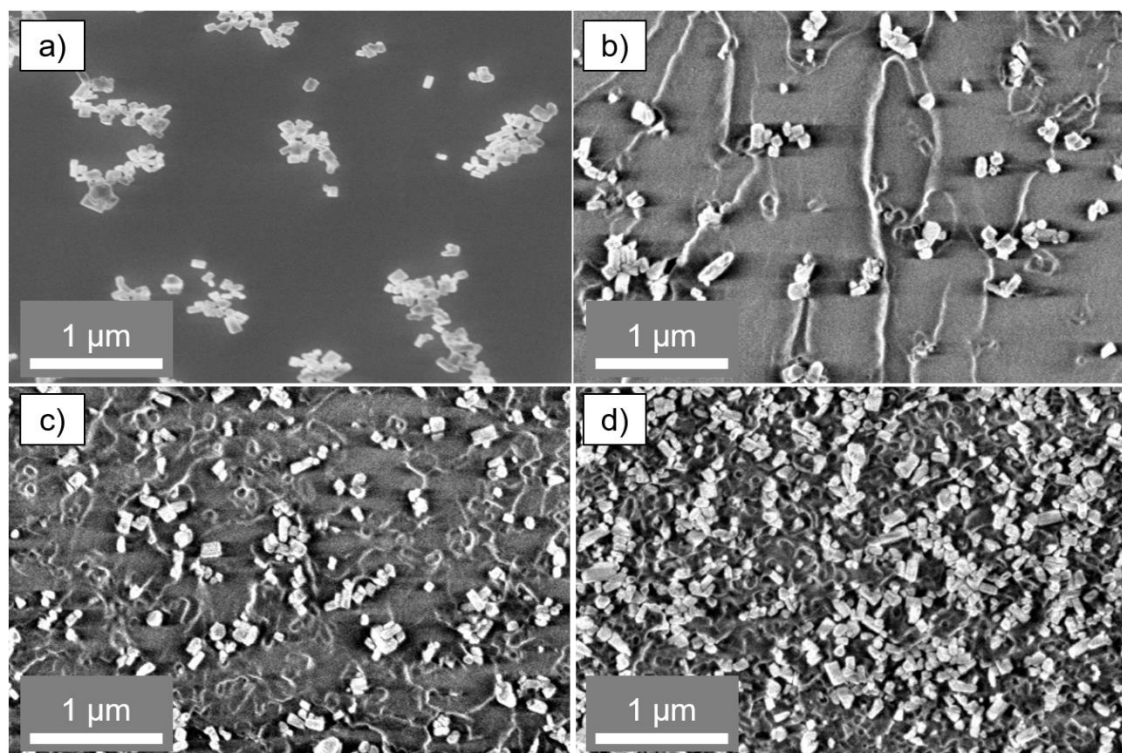


**Figure 4.4.** Scanning electron micrographs of a)  $\text{La}_{0.92}\text{Yb}_{0.075}\text{Er}_{0.005}\text{F}_3$  particles (LYEF), and cross sections of [LYEF]-[CN551] composites at b) 5 vol% LYEF, c) 15 vol% LYEF, and d) 30 vol% LYEF.

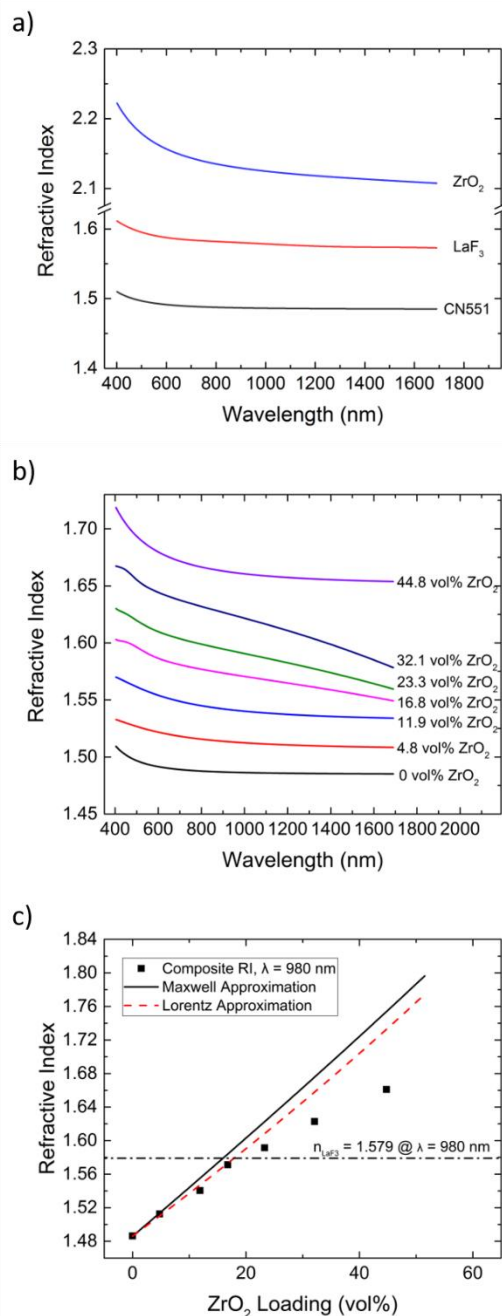


**Figure 4.5.** Changes in refractive index of the CN551 polymer matrix with respect to  $\text{ZrO}_2$  solids loading. a) Refractive index of the individual components. b) Refractive index of CN551 polymers at different  $\text{ZrO}_2$  solids loadings (vol%). c) Extracted refractive index values at  $\lambda = 980$  nm using Maxwell-Garnett and Lorentz-Lorenz Approximations.

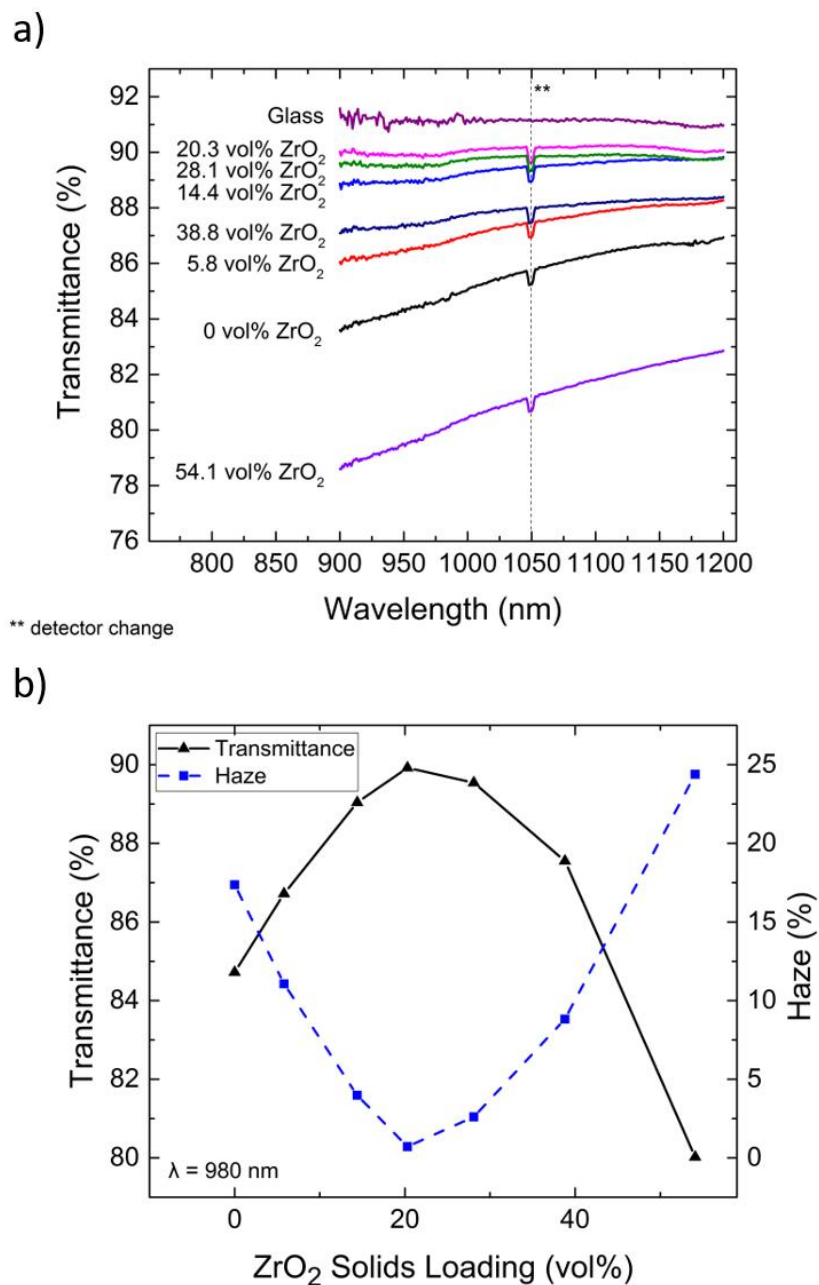


**Figure 4.6.** a) Transmittance of 5 vol% [LYEF]-[CN551-ZrO<sub>2</sub>] composites with respect to ZrO<sub>2</sub> solids loading. b) Extracted transmittance values and haze values at  $\lambda = 980 \text{ nm}$ . Losses due to scattering are minimized when the refractive index of the matrix matches that of [LYEF].

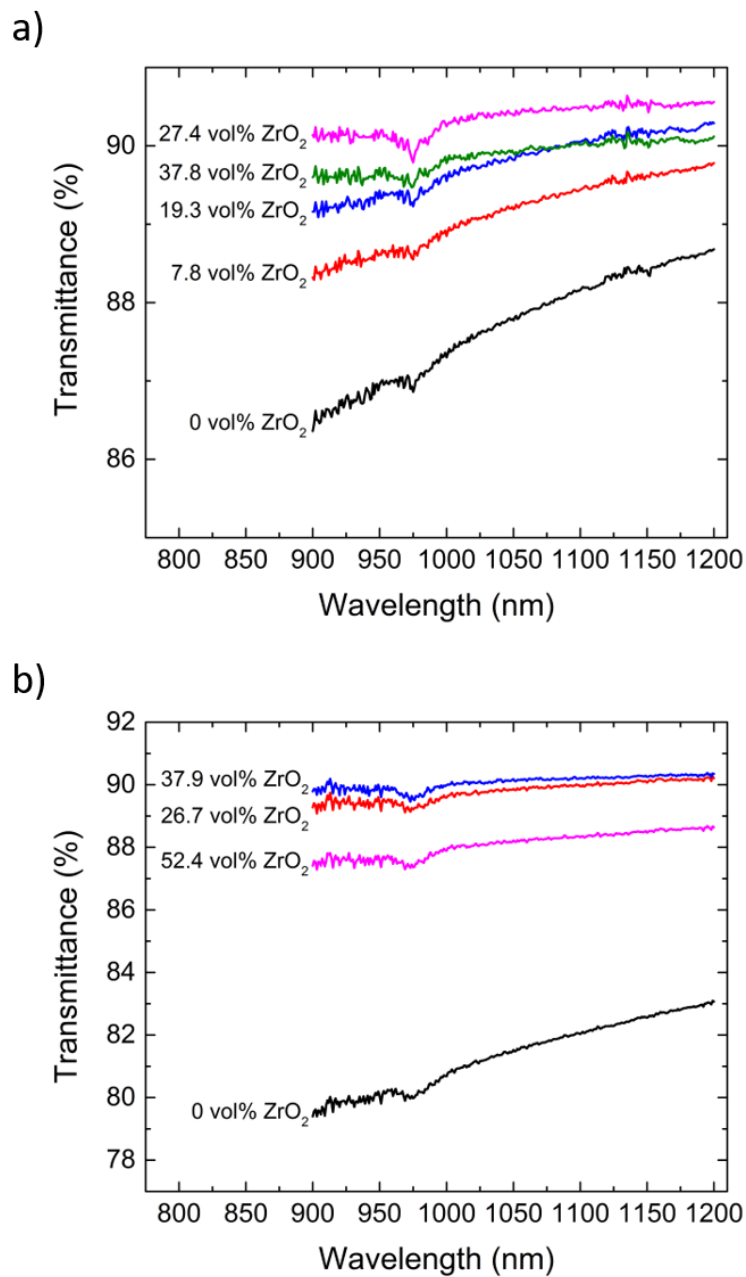
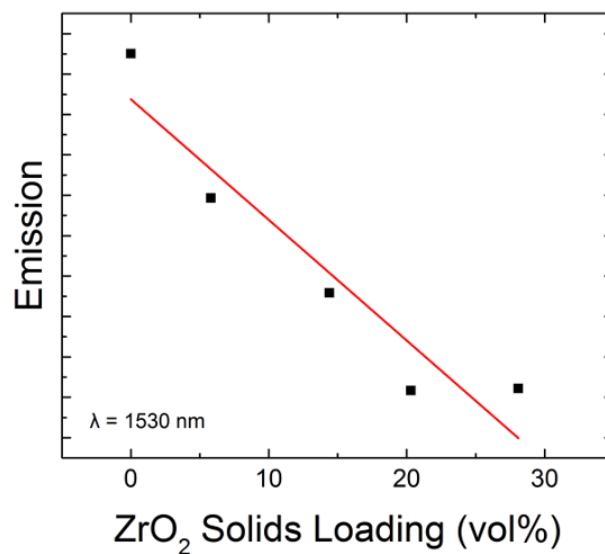


**Figure 4.7.** Transmittance of a) 15 vol% LYEF and b) 30 vol% LYEF nanocomposites. Maximum transmittance of the nanocomposites corresponds to the theoretically determined refractive index match point (27.4 vol% and 37.9 vol%  $\text{ZrO}_2$ , respectively).



a)



b)

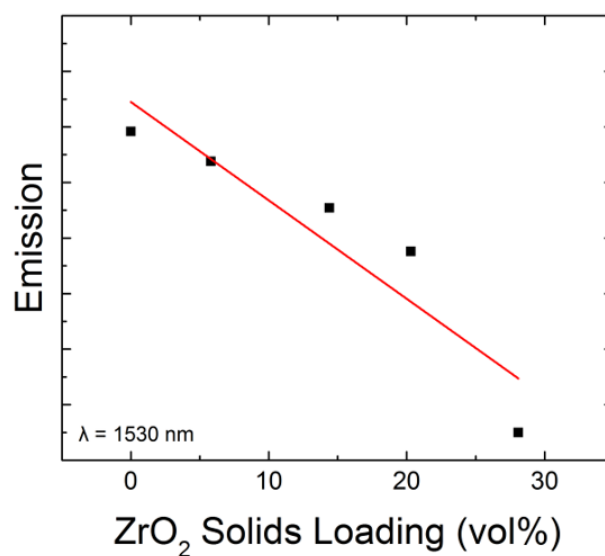


**Figure 4.8.** Relative intensity values of 15 vol% LYEF composites at  $\lambda = 1530$  nm as determined by photospectrometry. Curves indicate changes in relative intensities over time of 1530 nm emission. a) Measured 2 months after initial synthesis. b) Measured 18 months after synthesis.

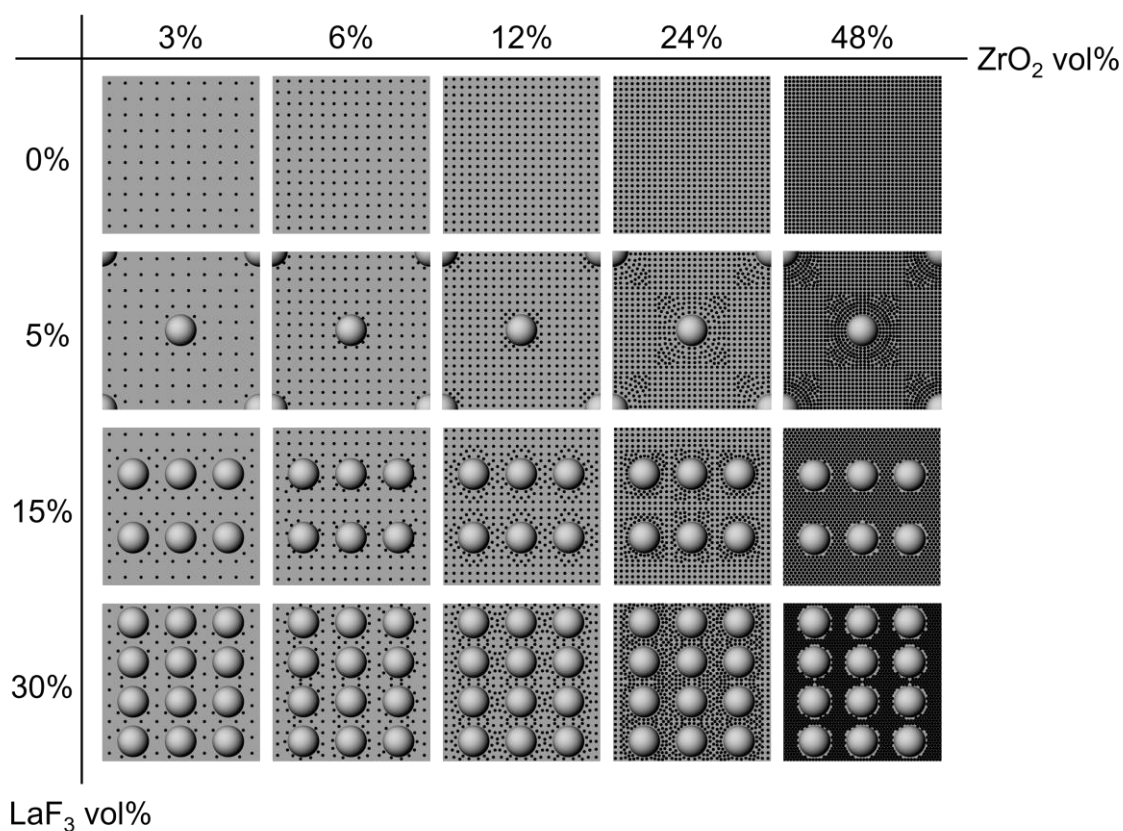


**Figure 4.9.** Microstructure schematic for initial conditions that result in proposed changes in microstructure that accounts for change in relative optical emission intensity with respect to  $\text{ZrO}_2$  ( $r = 4 \text{ nm}$ ) and  $\text{LaF}_3$  ( $r = 40 \text{ nm}$ ) solids loading over time. Initial solids loading conditions determine initial interparticle spacing (IPS) conditions.

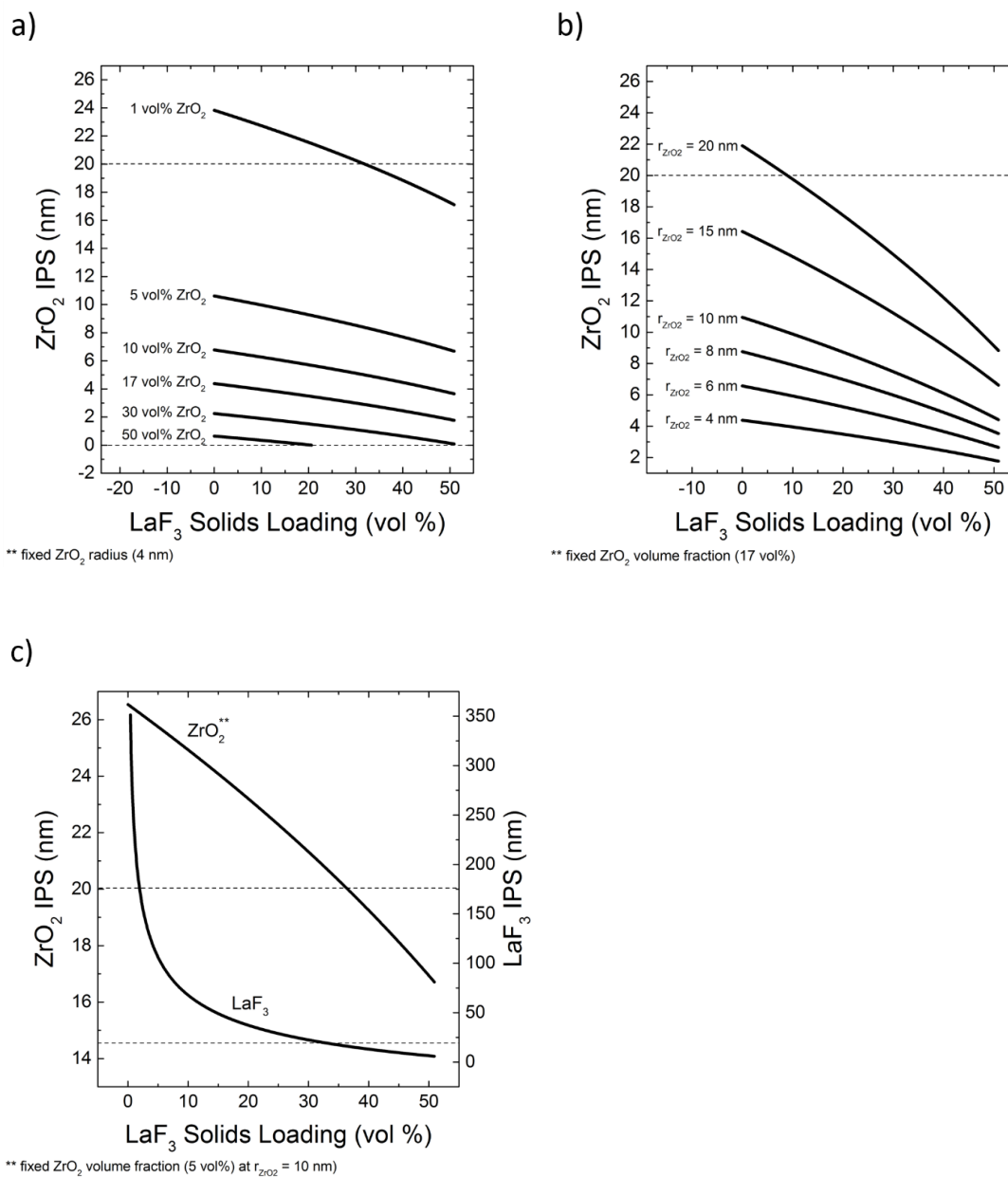


**Figure 4.10.** ZrO<sub>2</sub> nanoparticle IPS with respect to LaF<sub>3</sub> solids loading. IPS < 20 nm are distances at which attractive forces overcome repulsive forces. a) Fixed ZrO<sub>2</sub> particle size ( $r = 4$  nm) with variable ZrO<sub>2</sub> volume fraction. b) Fixed ZrO<sub>2</sub> volume fraction (17 vol%) with variable ZrO<sub>2</sub> particle size. c) LaF<sub>3</sub> and ZrO<sub>2</sub> IPS with fixed ZrO<sub>2</sub> volume fraction (5 vol%) and particle size ( $r = 10$  nm).

#### 4.6. Tables

**Table 4.1. Nanocomposite compositions for 5 vol% LYEF – CN551 – ZrO<sub>2</sub>.**

5 vol% LYEF – CN551 – ZrO <sub>2</sub> Composites							
Component (vol%)	A	B	C	D	E	F	G
La <sub>0.92</sub> Yb <sub>0.075</sub> Er <sub>0.005</sub> F <sub>3</sub>	5	5	5	5	5	5	5
CN551	95	89.2	80.6	74.7	66.9	56.2	40.9
ZrO <sub>2</sub>	0 (0 wt%)	5.8 (20 wt%)	14.4 (40 wt%)	20.3 (50 wt%)	28.1 (60 wt%)	38.8 (70 wt%)	54.1 (80 wt%)

**Table 4.2. Nanocomposite compositions for 15 vol% LYEF – CN551 – ZrO<sub>2</sub>.**

15 vol% LYEF – CN551 – ZrO <sub>2</sub> Composites					
Component (vol%)	A	B	C	D	E
La <sub>0.92</sub> Yb <sub>0.075</sub> Er <sub>0.005</sub> F <sub>3</sub>	15	15	15	15	15
CN551	85	77.2	65.7	57.6	47.2
ZrO <sub>2</sub>	0 (0 wt%)	7.8 (20 wt%)	19.3 (40 wt%)	27.4 (50 wt%)	37.8 (60 wt%)

**Table 4.3. Nanocomposite compositions for 30 vol% LYEF – CN551 – ZrO<sub>2</sub>.**

30 vol% LYEF – CN551 – ZrO <sub>2</sub> Composites				
Component (vol%)	A	B	C	D
La <sub>0.92</sub> Yb <sub>0.075</sub> Er <sub>0.005</sub> F <sub>3</sub>	30	30	30	30
CN551	70	43.3	32.1	17.6
ZrO <sub>2</sub>	0 (0 wt%)	26.7 (40 wt%)	37.9 (50 wt%)	52.4 (60 wt%)

#### 4.7. References

- (1) Werts, M. H. V. Making Sense of Lanthanide Luminescence. *Sci. Prog.* **2005**, *88* (2), 101–131.
- (2) Kido, J.; Okamoto, Y. Organo Lanthanide Metal Complexes for Electroluminescent Materials. *Chem. Rev.* **2002**, *102*, 2357–2368.
- (3) Sun, L. N.; Zhang, H. J.; Meng, Q. G.; Liu, F. Y.; Fu, L. S.; Peng, C. Y.; Yu, J. B.; Zheng, G. L.; Wang, S. Bin. Near-Infrared Luminescent Hybrid Materials Doped with Lanthanide (Ln) Complexes (Ln = Nd, Yb) and Their Possible Laser Application. *J. Phys. Chem. B* **2005**, *109* (13), 6174–6182.
- (4) Bünzli, J. C. G.; Eliseeva, S. V. Lanthanide NIR Luminescence for Telecommunications, Bioanalyses and Solar Energy Conversion. *J. Rare Earths* **2010**, *28* (6), 824–842.
- (5) Faulkner, S.; Pope, S. J. A.; Burton-Pye, B. P. Lanthanide Complexes for Luminescence Imaging Applications. *Appl. Spectrosc. Rev.* **2005**, *40*, 1–31.
- (6) Carlos, L. D.; Ferreira, R. A. S.; de Zea Bermudez, V.; Ribeiro, S. J. L. Lanthanide-Containing Light-Emitting Organic-Inorganic Hybrids: A Bet on the Future. *Adv. Mater.* **2009**, *21* (5), 509–534.
- (7) Slooff, L. H.; Van Blaaderen, A.; Polman, A.; Hebbink, G. A.; Klink, S. I.; Van Veggel, F. C. J. M.; Reinhoudt, D. N.; Hofstraat, J. W. Rare-Earth Doped Polymers for Planar Optical Amplifiers. *J. Appl. Phys.* **2002**, *91* (7), 3955–3980.
- (8) Riman, R. E.; Kumar, G. A.; Banerjee, S.; Brennan, J. G. Molecular Minerals™: Lyophillic Colloids for Ceramists. *J. Am. Ceram. Soc.* **2006**, *89* (6), 1809–1815.
- (9) Caseri, W. R. Nanocomposites of Polymers and Inorganic Particles: Preparation, Structure and Properties. *Mater. Sci. Technol.* **2006**, *22* (7), 807–817.
- (10) Althues, H.; Henle, J.; Kaskel, S. Functional Inorganic Nanofillers for Transparent Polymers. *Chem. Soc. Rev.* **2007**, *36*, 1454–1465.
- (11) Boyer, J. C.; Johnson, N. J.; van Veggel, F. C. J. Upconverting Lanthanide-Doped NaYF<sub>4</sub>-PMMA Polymer Composites Prepared by in Situ Polymerization. *Chem. Mater.* **2009**, *21*, 2010–2012.
- (12) Chai, R.; Lian, H.; Cheng, Z.; Zhang, C.; Hou, Z.; Xu, Z.; Lin, J. Preparation and Characterization of Upconversion Luminescent NaYF<sub>4</sub>:Yb, Er (Tm)/PS Bulk Transparent Nanocomposites through in Situ Polymerization. *J. Colloid Interface Sci.* **2010**, *345* (2), 262–268.
- (13) Lu, C.; Yang, B. High Refractive Index Organic-Inorganic Nanocomposites: Design, Synthesis and Application. *J. Mater. Chem.* **2009**, *19*, 2884–2901.
- (14) Xue, X.; Uechi, S.; Tiwari, R. N.; Duan, Z.; Liao, M.; Yoshimura, M.; Suzuki, T.; Ohishi, Y. Size-Dependent Upconversion Luminescence and Quenching Mechanism of LiYF<sub>4</sub>:Er<sup>3+</sup>/Yb<sup>3+</sup> Nanocrystals with Oleate Ligand Adsorbed. *Opt. Mater. Express* **2013**, *3* (7), 989–999.
- (15) Tian, Y.; Tian, B.; Cui, C.; Huang, P.; Wang, L.; Chen, B. Size-Dependent Upconversion Luminescence and Temperature Sensing Behavior of Spherical Gd<sub>2</sub>O<sub>3</sub>:Yb<sup>3+</sup>/Er<sup>3+</sup> Phosphor. *RSC Adv.* **2015**, *5* (19), 14123–14128.

- (16) Yuan, D.; Tan, M. C.; Riman, R. E.; Chow, G. M. Comprehensive Study on the Size Effects of the Optical Properties of NaYF<sub>4</sub>:Yb,Er Nanocrystals. *J. Phys. Chem. C* **2013**, *117* (25), 13297–13304.
- (17) Yang, L.; Li, G.; Zhao, M.; Yang, E.; Li, L. Lattice Defect Quenching Effects on Luminescence Properties of Eu<sup>3+</sup>-Doped YVO<sub>4</sub> Nanoparticles. *J. Nanoparticle Res.* **2013**, *15* (10).
- (18) Kumar, G. A.; Riman, R.; Snitzer, E.; Ballato, J. Solution Synthesis and Spectroscopic Characterization of High Er<sup>3+</sup> Content LaF<sub>3</sub> for Broadband 1.5 Mm Amplification. *J. Appl. Phys.* **2004**, *95* (1), 40–47.
- (19) Ballato, J.; Riman, R. E.; Snitzer, E. Sol-Gel Synthesis of Rare-Earth-Doped Lanthanum Halides for Highly Efficient 1.3-Mm Optical Amplification. *Opt. Lett.* **1997**, *22* (10), 691–693.
- (20) Heer, S.; Kömpe, K.; Güdel, H. U.; Haase, M. Highly Efficient Multicolour Upconversion Emission in Transparent Colloids of Lanthanide-Doped NaYF<sub>4</sub> Nanocrystals. *Adv. Mater.* **2004**, *16* (23–24), 2102–2105.
- (21) Wang, F.; Liu, X. Recent Advances in the Chemistry of Lanthanide-Doped Upconversion Nanocrystals. *Chem. Soc. Rev.* **2009**, *38* (4), 976–989.
- (22) Kumar, G. A.; Chen, C. W.; Ballato, J.; Riman, R. E. Optical Characterization of Infrared Emitting Rare-Earth-Doped Fluoride Nanocrystals and Their Transparent Nanocomposites. *Chem. Mater.* **2007**, *19* (6), 1523–1528.
- (23) Tan, M. C.; Patil, S. D.; Riman, R. E. Transparent Infrared Emitting CeF<sub>3</sub>:Yb-Er Polymer Nanocomposites for Optical Applications. *ACS Appl. Mater. Interfaces* **2010**, *2* (7), 1884–1891.
- (24) Chai, R.; Lian, H.; Yang, P.; Fan, Y.; Hou, Z.; Kang, X.; Lin, J. In Situ Preparation and Luminescent Properties of LaPO<sub>4</sub>:Ce<sup>3+</sup>, Tb<sup>3+</sup> Nanoparticles and Transparent LaPO<sub>4</sub>:Ce<sup>3+</sup>, Tb<sup>3+</sup>/PMMA Nanocomposite. *J. Colloid Interface Sci.* **2009**, *336* (1), 46–50.
- (25) Althues, H.; Simon, P.; Kaskel, S. Transparent and Luminescent YVO<sub>4</sub>:Eu/polymer Nanocomposites Prepared by *in Situ* Polymerization. *J. Mater. Chem.* **2007**, *17* (8), 758–765.
- (26) Tan, M. C.; Al-Baroudi, L.; Riman, R. E. Surfactant Effects on Efficiency Enhancement of Infrared-to-Visible Upconversion Emissions of NaYF<sub>4</sub>:Yb-Er. *ACS Appl. Mater. Interfaces* **2011**, *3* (10), 3910–3915.
- (27) Kumar, G. A.; Chen, C. W.; Riman, R.; Chen, S.; Smith, D.; Ballato, J. Optical Properties of a Transparent CaF<sub>2</sub>:Er<sup>3+</sup> Fluoropolymer Nanocomposite. *Appl. Phys. Lett.* **2005**, *86* (24), 241105.
- (28) Eldada, L.; Shacklette, L. W. Advances in Polymer Integrated Optics. *IEEE J. Sel. Top. Quantum Electron.* **2000**, *6* (1), 54–68.
- (29) Higashihara, T.; Ueda, M. Recent Progress in High Refractive Index Polymers. *Macromolecules* **2015**, *48* (7), 1915–1929.
- (30) Hass, G.; Ramsey, J. B.; Thun, R. Optical Properties of Various Evaporated Rare Earth Oxides and Fluorides. *J. Opt. Soc. Am.* **1959**, *49* (2), 116.
- (31) Nigara, Y. Measurement of the Optical Constants of Yttrium Oxide. *Jpn J. Appl. Phys.* **1968**, *7* (4), 404–408.

- (32) Thoma, R. E. *Rare-Earth Halides*; Oark Ridge, Tennessee, 1965.
- (33) Daimon, M.; Masumura, A. High-Accuracy Measurements of the Refractive Index and Its Temperature Coefficient of Calcium Fluoride in a Wide Wavelength Range from 138 to 2326 Nm. *Appl. Opt.* **2002**, *41* (25), 5275–5281.
- (34) Beaulieu, M. R.; Hendricks, N. R.; Watkins, J. J. Large-Area Printing of Optical Gratings and 3D Photonic Crystals Using Solution-Processable Nanoparticle/Polymer Composites. *ACS Photonics* **2014**, *1* (9), 799–805.
- (35) Tao, P.; Li, Y.; Siegel, R. W.; Schadler, L. S. Transparent Dispensible High-Refractive Index ZrO<sub>2</sub>/Epoxy Nanocomposites for LED Encapsulation. *J. Appl. Polym. Sci.* **2013**, *130* (5), 3785–3793.
- (36) Tao, P.; Li, Y.; Rungta, A.; Viswanath, A.; Gao, J.; Benicewicz, B. C.; Siegel, R. W.; Schadler, L. S. TiO<sub>2</sub> Nanocomposites with High Refractive Index and Transparency. *J. Mater. Chem.* **2011**, *21*, 18623–18629.
- (37) Zhang, G.; Zhang, H.; Wei, H.; Zhu, S.; Wu, Z.; Wang, Z.; Jia, F.; Zhang, J.; Yang, B. Creation of Transparent Nanocomposite Films with a Refractive Index of 2.3 Using Polymerizable Silicon Nanoparticles. *Part. Part. Syst. Charact.* **2013**, *30* (8), 653–657.
- (38) Li, C.; Colella, N. S.; Watkins, J. J. Low-Temperature Fabrication of Mesoporous Titanium Dioxide Thin Films with Tunable Refractive Indices for One-Dimensional Photonic Crystals and Sensors on Rigid and Flexible Substrates. *ACS Appl. Mater. Interfaces* **2015**, *7* (24), 13180–13188.
- (39) Howell, I. R.; Li, C.; Colella, N. S.; Ito, K.; Watkins, J. J. Strain-Tunable One Dimensional Photonic Crystals Based on Zirconium Dioxide/Slide-Ring Elastomer Nanocomposites for Mechanochromic Sensing. *ACS Appl. Mater. Interfaces* **2015**, *7* (6), 3641–3646.
- (40) Nakayama, N.; Hayashi, T. Preparation and Characterization of TiO<sub>2</sub> and Polymer Nanocomposite Films with High Refractive Index. *J. Appl. Polym. Sci.* **2007**, No. 105, 3662–3672.
- (41) Imai, Y.; Terahara, A.; Hakuta, Y.; Matsui, K.; Hayashi, H.; Ueno, N. Transparent Poly(bisphenol A Carbonate)-Based Nanocomposites with High Refractive Index Nanoparticles. *Eur. Polym. J.* **2009**, *45* (3), 630–638.
- (42) Wang, F.; Luo, Z.; Qing, S.; Qiu, Q.; Li, R. Sol-Gel Derived Titania Hybrid Thin Films with High Refractive Index. *J. Alloys Compd.* **2009**, *486* (1–2), 521–526.
- (43) Wang, B.; Wilkes, G. L.; Hedrick, J. C.; Liptak, S. C.; McGrath, J. E. New High Refractive Index Organic/Inorganic Hybrid Materials from Sol-Gel Processing. *Macromolecules* **1991**, *24*, 3449–3450.
- (44) Kyprianidou-Leodidou, T.; Caseri, W.; Suter, U. W. Size Variation of PbS Particles in High-Refractive-Index Nanocomposites. *J. Phys. Chem.* **1994**, *98*, 8992–8997.
- (45) Kyprianidou-Leodidou, T.; Althaus, H.-J.; Wyser, Y.; Vetter, D.; Büchler, M.; Caseri, W.; Suter, U. W. High Refractive Index Materials of Iron Sulfides and Poly(ethylene Oxide). *J. Mater. Res.* **1997**, *12* (8), 2198–2206.
- (46) Lee, S.; Shin, H.-J.; Yoon, S.-M.; Yi, D. K.; Choi, J.-Y.; Paik, U. Refractive Index Engineering of Transparent ZrO<sub>2</sub>-polydimethylsiloxane Nanocomposites. *J. Mater. Chem.* **2008**, *18*, 1751–1755.

- (47) Tsai, C.-M.; Hsu, S.-H.; Ho, C.-C.; Tu, Y.-C.; Tsai, H.-C.; Wang, C.-A.; Su, W.-F. High Refractive Index Transparent Nanocomposites Prepared by in Situ Polymerization. *J. Mater. Chem. C* **2014**, 2 (12), 2251–2258.
- (48) Ballato, J.; Foulger, S.; Smith, Jr., D. W. Optical Properties of Perfluorocyclobutyl Polymers. *J. Opt. Soc. Am. B* **2003**, 20 (9), 1838.
- (49) International, A. D1003. Standard Test Method for Haze and Luminous Transmittance of Transparent Plastics. **2013**, 7.
- (50) Hao, T.; Riman, R. E. Calculation of Interparticle Spacing in Colloidal Systems. *J. Colloid Interface Sci.* **2006**, 297 (1), 374–377.



## Chapter 5. FINAL REMARKS

In summary, a steady and sustainable rare earth supply chain that enables rare earth based technologies begins with a codified understanding of the fundamental properties of the rare earth carbonates that then can be used in thermodynamic process simulations to discover new means of separating rare earths from different phases. A review of the fundamental properties of the normal rare earth carbonates and rare earth hydroxycarbonates has found trends in the crystallography, thermochemistry, aqueous behavior, and thermal decomposition. The shrinking lattice parameters, decreasing magnitude in thermochemical parameter(s), downward trending decomposition temperatures, and increasing solubility with increasing atomic number have basis within the concept of the lanthanide contraction along with the chemical implication thereof. What we have found is that most of these values can benefit from further refinement and exploration. Despite the limitations on the thermochemical and aqueous solubility values, they have proven sufficient to be utilized in thermodynamic process simulations to predict the precipitation of the rare earth normal carbonates ( $\text{RE}_2(\text{CO}_3)_3 \cdot x\text{H}_2\text{O}$ ) from aqueous solutions at industrially relevant concentrations. Concentrated solutions of MEA loaded with  $\text{CO}_2$  have been used to successfully deplete concentrated solutions, up to 100 g/L or  $10^{-0.4}$  molality, of rare earth chlorides with  $\geq 99\%$  efficiency and precipitate the rare earths as  $\text{La}_2(\text{CO}_3)_3 \cdot 8\text{H}_2\text{O}$ ,  $\text{Nd}_2(\text{CO}_3)_3 \cdot 8\text{H}_2\text{O}$ , and  $\text{Y}_2(\text{CO}_3)_3 \cdot 2\text{H}_2\text{O}$ . The filtrate, which contains MEA-HCl, can be recovered and used as a secondary chemical product, eliminating a large waste concern associated with other precipitation methods. Though there were inconsistencies between the predicted precipitate and the one observed, the value of prediction has been established. It should be noted that continuing development of the database and thermodynamic model used to predict phase equilibria would benefit from accounting for the nuanced equilibrium between the normal carbonates and hydroxycarbonates in water with respect to  $\text{pCO}_2$ . The demonstrated work on optically active,

transparent composite materials has contextualized the importance of a stable rare earth supply chain in the development, deployment, and improvement of high technologies based on the rare earths. The composites have achieved high levels of transmittance (optical transparency) with phosphor loadings of  $\geq 5$  vol% while demonstrating the optical absorption/emission pair characteristic of  $\text{Er}^{3+}$ , mechanical robustness due to the polymer matrix, and a facile synthesis method afforded by the spin-coating technique. However, the composites require further tuning as long term degradation of the optical properties due to particle agglomeration necessitates additional study. These studies would focus on improving the stability of the matrix by utilizing different combinations of solvents, polymer matrix, high refractive index tuning phase, and/or phosphor host to achieve stability.

## **Appendix 1. ANNEALING SODIUM YTTRIUM FLUORIDE NANOPOWDERS TO IMPROVE OPTICAL PROPERTIES AND SURFACE CHEMISTRY**

We demonstrate the efficacy of a low temperature annealing process that improves the optical efficiency of nanocrystalline phosphors while leaving surface chemistry intact.  $\text{NaY}_{0.78}\text{Yb}_{0.20}\text{Er}_{0.02}\text{F}_4$  phosphors, prior to and post annealing at a range of temperatures between 200 °C to 400 °C, were characterized to show changes in surface chemistry, optical properties, and physical properties.

Solvothermal synthesis of the core-shell  $\text{NaY}_{0.78}\text{Yb}_{0.20}\text{Er}_{0.02}\text{F}_4@\text{NaYF}_4$  nanoparticles is a two-step process in which two distinct solutions, ‘Core’ and ‘Shell’, were added in succession to achieve the core-shell structure. This process is a modified variant of previous literature that has synthesized doped  $\text{NaYF}_4$  nanoparticles utilizing oleylamine as the high temperature solvent. 98% primary amine Oleylamine (*cis*- $\text{CH}_3(\text{CH}_2)_7\text{CH}=\text{CH}(\text{CH}_2)_7\text{CH}_2\text{NH}_2$ ) and 98% Sodium Trifluoroacetate ( $\text{Na}(\text{CF}_3\text{COO})$ , NaTFA) were purchased from Sigma Aldrich (Saint Louis, Missouri, USA). 99.9% metals basis Yttrium trifluoroacetate ( $\text{Y}(\text{CF}_3\text{COO})_3$ ,  $\text{Y}(\text{TFA})_3$ ), 99.9% metals basis Ytterbium trifluoroacetate ( $\text{Yb}(\text{CF}_3\text{COO})_3$ ,  $\text{Yb}(\text{TFA})_3$ ), and 99.9% metals basis Erbium trifluoroacetate ( $\text{Er}(\text{CF}_3\text{COO})_3$ ,  $\text{Er}(\text{TFA})_3$ ) were purchased from GFS Chemicals (Powell, Ohio, USA). ‘Core’: Individual solutions of NaTFA,  $\text{Y}(\text{TFA})_3$ ,  $\text{Yb}(\text{TFA})_3$ , and  $\text{Er}(\text{TFA})_3$  in Oleylamine were mixed and diluted with additional Oleylamine to achieve the desired concentrations in the single, final ‘Core’ solution: 0.1 M NaTFA, 0.039 M  $\text{Y}(\text{TFA})_3$ , 0.01 M  $\text{Yb}(\text{TFA})_3$ , and 0.001 M  $\text{Er}(\text{TFA})_3$ . These concentrations represent a 2:1 ratio of sodium to total rare earth(s) and a 39:10:1 ratio of  $\text{Y}^{3+}$ : $\text{Yb}^{3+}$ : $\text{Er}^{3+}$ , or 2 mol%  $\text{Er}^{3+}$ , 20 mol%  $\text{Yb}^{3+}$ , and 78 mol%  $\text{Y}^{3+}$ . ‘Shell’: This solution was prepared by mixing the molar amounts of NaTFA (0.5 M) and YTFA (0.25 M) in Oleylamine to achieve the desired concentrations. The 2:1 ratio between sodium and rare earth(s) is maintained.

50 ml of 'Core' solution was heated and stirred with Argon bubbling at  $\sim 120$  °C for 1 hour. At the end of the hour, Argon bubbling was removed and replaced with Argon overpressure. Solution temperature was then increased to and held at 340 °C for 1 hour. 10 ml of 'Shell' solution was then injected via syringe pump over a 10-minute period. The reaction was held at temperature for an additional 45 minutes to allow for shell growth. The solution was then cooled to room temperature in the ambient while stirring and under Argon flow; the solution/glassware was removed from the heating mantle. The nanoparticles were harvested by precipitating and centrifuging three times at 8000 xG for 10 minutes with Absolute Ethanol to remove excess Oleylamine. Once fully cleaned, the particles were resuspended in water, frozen in liquid N<sub>2</sub>, and lyophilized until fully dry. Powders were annealed under positive N<sub>2</sub> flow in a Micromeritics SmartPrep Degasser (Norcross, Georgia, USA). The annealing chamber was first purged with N<sub>2</sub> for 30 minutes. The samples were then annealed at the desired temperature for 60 minutes under N<sub>2</sub> flow. Samples are then cooled to room temperature under N<sub>2</sub> flow.

Fourier transform infrared spectroscopy of NaY<sub>0.78</sub>Yb<sub>0.20</sub>Er<sub>0.02</sub>F<sub>4</sub> annealed at 200 °C shows that surface chemistry is relatively unchanged, with the bands characteristic of Oleylamine, such as the CH<sub>2</sub> stretching, CH<sub>3</sub> symmetric and asymmetric stretching, and blue shifted N-H bending vibrations, present. Optical efficiency improvements of 10%, as measured by a modified Hamamatsu Quantum Yield Measurement System, due to heat treatment can be attributed to the improved crystallinity of the phosphors due to the loss of bulk hydroxyls that occupy fluoride sites, loss of surface hydroxyls that vibronically quench emissions from surface dopant atoms, and redistribution of lanthanide ions within the phosphor particles. Phosphors treated at 300 °C also demonstrate improved optical efficiency, similar to those of phosphors treated at 200 °C, over untreated phosphors, but have changed crystalline phase distribution and larger crystallites as shown via XRD and TEM, respectively. Phosphors treated at 400 °C show degraded optical

efficiency with significantly larger crystallites (via XRD peak fitting and TEM). Degraded optical efficiency is attributed to the significant contamination from Oleylamine decomposition as evidenced by decreased FTIR absorption and qualitative observations of carbon contamination.

Improving optical efficiency, which improves imaging depth, while maintaining surface chemistry and particle size allows for their post-treatment use in short wave infrared region (SWIR) biomedical imaging platforms that require specific surface chemistry and particle size for biocompatibility, cellular targeting, and long term residence within the animal. We have demonstrated that a low temperature annealing process in inert atmospheres may be used to improve the optical performance of phosphors while leaving the crucial surface chemistry and particle sizes relatively intact.